Computer Modelling Studies of New Electrode Materials for Rechargeable Batteries

Wood, Stephen

Award date:
2015

Awarding institution:
University of Bath

Computer Modelling Studies of New Electrode Materials for Rechargeable Batteries

submitted by

Stephen Michael Wood

for the degree of Doctor of Philosophy

of the

University of Bath

Department of Chemistry

September 2015

Contents

List of Figures

List of Tables

List of Publications and Presentations

Publications

1. Tripathi R., Wood S. M., Islam M. S. and Nazar L. F., "Na-ion mobility in layered Na_2FePO_4F and olivine $Na[Fe,Mn]PO_4$", *Energy Environ. Sci.*, **6**, 2257-2264 (2013) [citations=56]

2. Wood S. M., Eames C., Kendrick E. and Islam M. S., "Sodium Ion Diffusion and Voltage Trends in Phosphates $Na_4M_3(PO_4)_2P_2O_7$ (M = Fe, Mn, Co, Ni) for Possible High-Rate Cathodes", *J. Phys. Chem. C*, **199 (28)**, 15935-15941 (2015)

3. Roos J., Eames C., Wood S. M., Whiteside A. and Islam M. S., "Unusual Mn coordination and redox chemistry in the high capacity borate cathode $Li_7Mn(BO_3)_3$", *Phys. Chem. Chem. Phys.*, **17**, 22259-22265 (2015)

4. Yuan Y., Wood S. M., Yao W., Tompsett D. A., He K., Lu J., Nie A., Islam M. S. and Shahbazian-Yassar R.,"Atomistic Visualization of Self-Assembly Growth of Tunnel-based Oxide Nanostructures", *ACS Nano*, **In Press** (2015)

5. Wood S. M., Fisher C. A. J. and Islam M. S., "Surface structures and crystal morphologies of Na-ion cathode material Na_2FePO_4F", *Chem. Mater.*, **To be submitted**, (2015)

Oral Presentations - International

1. Oct 2013; **1st Symposium on Na Batteries, Victorria-Gastiez, Spain**; *"Na-ion Mobility in Layered Na_2FePO_4F and Olivine $NaFePO_4$"*

2. June 2015; **Japan Fine Ceramics Centre Internal Seminar, Nagoya, Japan**; *"Surface Features and Energetics of the Na-ion Cathode Material Na_2FePO_4F"*

3. June 2015; **Lithium Battery Discussions, Arcachon, France**; *"Sodium-Ion Diffusion and Voltage Trends in Phosphates $Na_4M_3(PO_4)_2P_2O_7$ (M = Fe, Mn, Ni, Co) for Possible High Rate Cathodes"*

Oral Presentations - UK

1. March 2013; **Computational Group Seminar, University of Bath**; *"Novel Polyanionic Materials for Li-ion and Na-ion Batteries"*

2. June 2013; **CSCT Postgraduate Symposium Series, University of Bath**; *"Computer Modelling of New Cathode Materials for Lithium-Ion Batteries"*

3. July 2013; **Research Seminar, SHARP Laboratories of Europe, Oxford**; *"Modelling Studies of Novel Polyanionic Materials for Li-ion and Na-ion Batteries"*

4. Sep 2013; **CSCT Summer Showcase, University of Bath**; *"Modelling Studies of Novel Polyanionic Materials for Na-ion Batteries"* **(Prize Winner)**

5. Mar 2014; **Chemistry Postgraduate Symposium Series, University of Bath**; *"Na-ion Mobility in Layered Na_2FePO_4F and Olivine $NaFePO_4$"*

6. Apr 2014; **RSC Solid State Group Easter Meeting, Chicheley**; *"Na-ion Mobility in Layered Na_2FePO_4F and Olivine $NaFePO_4$"*

7. Oct 2014; **RSC 6th Form Chemistry Afternoon, BRLSI, Bath**; *"Solar Energy and Green Batteries"*

8. Dec 2014; **RSC Solid State Group Christmas Meeting, Glasgow**; *"Beyond Lithium-Ion: Insights into Novel Phosphate Materials for Na-ion Batteries"*

9. Feb 2015; **RSC 6th Form Chemistry Afternoon, BRLSI, Bath**; *"Solar Energy and Green Batteries"*

10. Mar 2015; **CSCT Postgraduate Symposium Series, University of Bath**; *"Evolutionary Structure Prediction of Na-ion Battery Materials"*

11. July 2015; **CSCT Summer Showcase, University of Bath**; *"Computational Insights into Novel Na-ion Battery Cathode Materials"*

Poster Presentations - International

1. June 2014; **International Meeting on Lithium Batteries 2014, Como, Italy**; *"Na-ion Mobility in Layered Na_2FePO_4F and Olivine $Na[Fe_Mn]PO_4$"*
2. Oct 2014; **1st Yonsei-Bath International Workshop on Energy, Environment and Sustainability**; *"Novel Phosphate Materials for Na-ion Batteries: Defect, Voltage and Ion Diffusion Properties"*
3. June 2015; **Lithium Battery Discussions, Arcachon, France**; *"Sodium-Ion Diffusion and Voltage Trends in Phosphates $Na_4M_3(PO_4)_2P_2O_7$ (M = Fe, Mn, Ni, Co) for Possible High Rate Cathodes"*

Poster Presentations - UK

1. May 2013; **Chemistry Postgraduate Symposium, University of Bath**; *"Na-ion Batteries: Atomistic Simulations of Novel Cathode Materials"*
2. June 2013; **Science Graduate Research Afternoon, University of Bath**; *"Na-ion Batteries: Atomistic Simulations of Novel Cathode Materials"*
3. Dec 2013; **RSC Solid State Group Christmas Meeting, University of Bath**; *"Na-ion Mobility in Layered Na_2FePO_4F and Olivine $NaFePO_4$ for Sodium-Ion Batteries"*
4. Sept 2014; **Energy Materials: Computational Solutions, University of Bath**; *"Materials for Sodium-Ion Batteries"*
5. Mar 2015; **STFC Early Career Reserachers Conference, Abingdon**; *"Beyond Li-ion: Atomistic Properties of Novel Cathode"*
6. Apr 2015; **Advances in Li-Battery Research, Loughborough**; *"Beyond Li-ion: Atomistic Properties of Novel Cathode"*
7. Sept 2015; **Energy Materials: Computational Solutions, University of Bath**; *"Sodium-Ion Diffusion and Voltage Trends in Phosphates $Na_4M_3(PO_4)_2P_2O_7$ (M = Fe, Mn, Ni, Co) for Possible High Rate Cathodes"*

Abstract

Developing a sustainable energy infrastructure for the 21st century requires the large scale development of renewable energy resources. Fully exploiting these inherently intermittent supplies will require advanced energy storage technologies, with rechargeable Li-ion and Na-ion batteries considered highly promising for both vehicle electrification and grid storage applications. However, the performance required of battery materials has not been achieved, and significant improvements are needed. Modern computational techniques allow the elucidation of structure-property relationships at the atomic level and are valuable tools in providing fundamental insights into novel materials. Therefore, in this thesis a combination of atomistic simulation and *ab initio* density functional theory (DFT) techniques have been used to study a number of potential battery cathode materials. Firstly, Na_2FePO_4F and $NaFePO_4$ are interesting materials that have been reported recently as attractive positive electrodes for Na-ion batteries. Here, we report their Na-ion conduction behaviour and intrinsic defect properties using atomistic simulation methods. Na^+ ion conduction in Na_2FePO_4F is predicted to be two-dimensional (2D) in the interlayer plane. Na ion migration in $NaFePO_4$ is restricted to the [010] direction along a curved trajectory, leading to quasi-1D Na^+ diffusion. Furthermore, Na/Fe antisite defects are predicted to have a lower formation energy in $NaFePO_4$ than Na_2FePO_4F. The higher probability of tunnel occupation with a relatively immobile Fe^{2+} cation - along with a greater volume change on redox cycling - contributes to the poor electrochemical performance of $NaFePO_4$. Secondly, work on the Na_2FePO_4F system is extended to include investigation of the surface structures and energetics. The equilibrium morphology is found to be essentially octagonal, compressed slightly along the [010] direction, and is dominated by the (010), $(02\bar{1})$, $(1\bar{2}\bar{2})$ and $(1\bar{1}0)$ surfaces. The calculated growth morphology is a more "rod-like" nanoparticle, with the $(02\bar{1})$, $(02\bar{3})$, $(1\bar{1}0)$ and $(1\bar{1}\bar{2})$ planes predominant. The (010) surface lies parallel to the Na layers in the *ac* plane and is unlikely to facilitate Na^+ intercalation. As such, its prominence in the equilibrium morphology, and absence from the growth morphology, suggests nanoparticles synthesised in a kinetically limited regime should provide higher rate performance than those synthesised in close to equilibrium conditions. Surface redox potentials for Na_2FePO_4F derived using DFT vary between 2.76 - 3.37 V, in comparison to a calculated bulk cell voltage of 2.91 V. Most significantly, the lowest energy potentials are found for the $(1\bar{3}0)$ and (001) planes suggesting that upon charging Na^+ will first be extracted from these surfaces, and inserted lastly upon discharging. Thirdly, the mixed phosphates $Na_4M_3(PO_4)_2P_2O_7$ (M=Fe, Mn, Co, Ni) are explored as a fascinating new class of materials reported to be attractive Na-ion cathodes, displaying low volume changes upon cycling indicative of long lifetime operation. Key issues surrounding intrinsic defects, Na-ion migration mechanisms and voltage trends have

been investigated through a combination of atomistic energy minimisation, molecular dynamics and DFT simulations. The MD results suggest Na^+ diffusion extends across a 3D network of migration pathways with an activation barrier of 0.20-0.24 eV, and diffusion coefficients (D_{Na}) of $10^{-10} - 10^{-11} cm^2 s^{-1}$ at 325 K, suggesting high rate capability. The cell voltage trends, explored using DFT methods, indicate that doping the Fe-based cathode with Ni can significantly increase the voltage, and hence energy density. Finally, DFT simulations of K^+-stabilised α-MnO_2 have been combined with aberration corrected-STEM techniques to study the surface energetics, particle morphologies and growth mechanism. α-$K_{0.25}MnO_2$ grown through a hydrothermal synthesis method is found to produce primary nanowires with preferential growth along the [001] direction. Primary nanowires attach through a shared (110) interface to form larger secondary nanowires. This is in agreement with DFT simulations with the {100}, {110} and {211} surfaces displaying the lowest surface energies. The ranking of surface energies is driven by Mn coordination environments and surface relaxation. The calculated equilibrium morphology of α-$K_{0.25}MnO_2$ is consistent with the observed primary nanowires from high resolution electron microscopy images.

Acknowledgements

Firstly, I must extend my warmest thanks to my supervisor Prof. Saiful Islam for giving me the opportunity to conduct this research. Much of what I have gained over the course of my PhD can be directly attributed to his expertise, support and guidance. For that I will be eternally grateful. I am also indebted to all the members of the Islam group, past and present, whom it has been an absolute privilege to work with (including in no particular order: John Clark, Graheme Gardiner, Jesse Dufton, David Tompsett, Chris Eames, Alex Whiteside, Jenny Heath, Yue Deng, Julian Roos and Hungru Chen). I must give special thanks to John Clark for all his assistance when I first began this journey, David Tompsett for all his advice in the application of DFT, and particularly Chris Eames, without whose vast knowledge and patience I likely could not have completed this work.

Over the course of my PhD I have been extremely fortunate to have been able to perform work outside of Bath and must extend my sincerest appreciation to all those who made it possible. Dr Emma Kendrick and her team at SHARP Laboratories Europe were gracious (or naive) enough to let me try my hand at experimental work and have supported much of my work. In addition, I must thank Dr Craig Fisher and the nanosimulation team at JFCC in Nagoya for sharing their expertise of simulation techniques, and allowing me the brilliant experience of a placement in Japan.

My family deserve a special recognition. The further I move through life the more I come to realise that all the things I do are only possible because of all that they have done for and taught me. I also wish to show my appreciation to everyone involved with the Centre for Sustainable Technologies, for every opportunity I have been provided with has been a direct result of all their hard work and understanding. I genuinely cannot express the depth of my gratitude to all involved. Finally, there are so many others whom I need to thank and I can only apologise if you have been omitted, I assure you it was not intentional. However, it would be remiss not to mention the other students at the CSCT, and in particular cohort 2011. You all have my deepest admiration and respect, without you the last four years just would not have been the same.

1 Introduction

"Equipped with his five senses man explores the
universe around him and calls the adventure Science."
Edwin Powell Hubble

1.1 Energy Generation and Storage in the 21st Century

It is now widely accepted that anthropogenic carbon dioxide emissions are leading to significant, and potentially irreversible, alterations to the global climate. The vast majority of these emissions are a direct result of the burning of fossil fuels to provide power for modern society. Additional concerns over energy security and resource scarcity provide further impetus to move beyond fossil fuels to a low carbon economy. Addressing these problems requires the exploitation of renewable energy resources, coupled with a transition in energy vectors. As such, the development of a sustainable energy infrastructure is one of the greatest technological challenges of the 21st century.

Suitable energy storage technologies will be critical to any future energy framework. Renewable energy resources are inherently intermittent and diffuse in time and location. Therefore, as they begin to form a greater fraction of electricity generation, primary supplies may become more unstable. As such, energy storage technologies will

be required to match supply with demand, whilst also maintaining supply quality. In addition, road transportation currently accounts for approximately 25% of CO_2 emissions in developed countries [1]; as such, the decoupling of transportation from the fossil fuel economy is essential to reducing CO_2 emissions. Whilst various fossil fuel alternatives exist, for many applications rechargeable batteries are the most promising. Unfortunately, energy storage technologies currently demonstrate inadequate overall performance for either task, largely driven by the properties and characteristics of their constituent materials. Therefore, innovative materials science is central to current energy storage research and future development.

Lithium ion batteries have become synonymous with high energy density secondary (rechargeable) batteries in recent years, coming to dominate the portable electronics market (e.g. mobile phones, laptops, mp3 players (see Figure 1-1)). This is primarily due to their exceptional energy storage capacity, in both gravimetric and volumetric terms, as illustrated in Figure 1-2. This makes them excellent candidates for hybrid and electric vehicles, with several car models already on the market [2–4]. However, current Li-ion battery materials display certain properties inhibiting their performance in electric vehicles, including concerns over safety, toxicity, cost and sustainability. Hence, the development of improved Li-ion battery and alternative chemistries is a highly active area of research.

In principle, Li-ion technology is also well placed to meet the requirements of grid storage as it can provide batteries with both large energy density and high round trip efficiency, alongside excellent power delivery properties. In addition, the modular nature of Li-ion batteries allows rapid scale up/down, from single home to citywide storage. Therefore, batteries could be used for bulk energy storage (akin to pumped hydroelectric and compressed air storage). Alternatively, if built for high kinetics and power capability batteries could fulfill an intermediate role between the renewable farm and the main grid, ensuring a stable, high quality electricity supply. However, the use of Li-ion batteries in these applications is currently prohibited by high battery costs. With the predicted increase in Li-ion battery sales, as application moves from portable electronics to electric vehicles, cost pressures are likely to intensify. Furthermore, lithium is widely used in the production of glasses, ceramics and pharmaceuticals; and is pre-

[Figure removed for copyright reasons]

Figure 1-1: *Examples of Li-ion battery applications: smartphones and tablets (top); power tools and other portable electronics (middle); electric vehicles (bottom).*

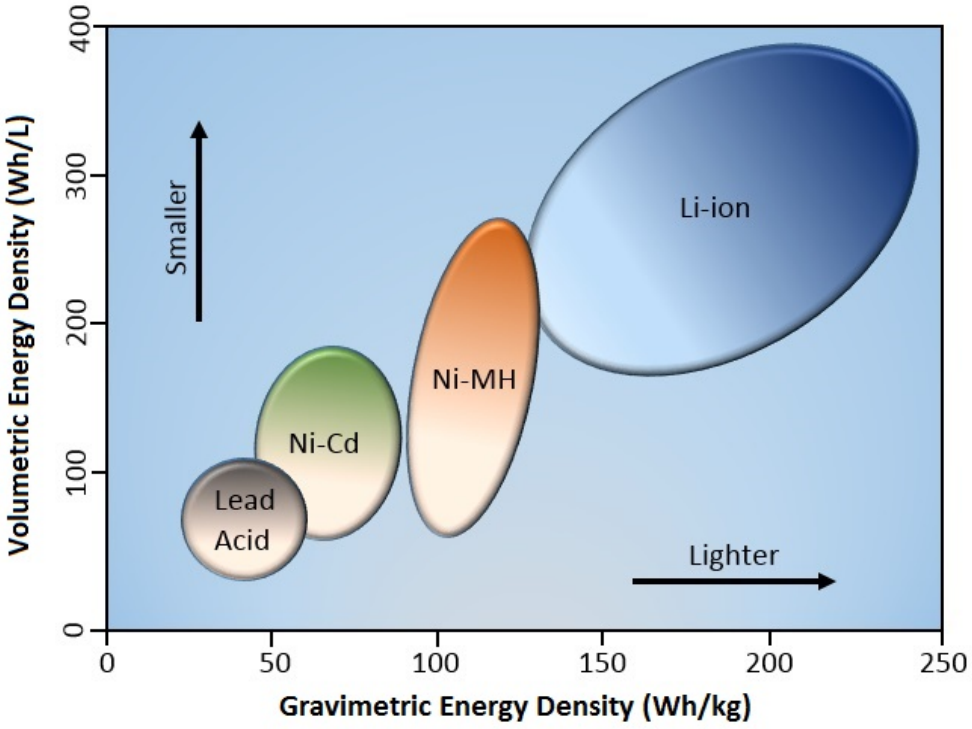

Figure 1-2: *Volumetric and gravimetric capacities of secondary batteries by battery type. Adapted from Tarascon et al. [5]*

dicted to feature heavily in the next generation of nuclear power plants - all industries expected to expand rapidly in the coming years [6]. As such, recent research has focused on finding an alternative to lithium so as to reduce battery costs using widely available elements.

Na-ion batteries work on the exact same principles as Li-ion technology, but with Na^+ substituted for Li^+. Accordingly, they share many characteristics with their lithium ion counterparts, displaying similar intercalation and transport properties [7]. Crucially, unlike lithium, sodium has an essentially unlimited natural abundance and resources are widely dispersed around the globe [8]. However, research into Na-ion batteries is still in its infancy as compared to the established Li-ion battery sector and many materials hurdles exist. Consequently, the provision and characterization of new materials and concepts, with a deeper understanding of the materials science involved, is essential to producing suitable Na-ion battery technologies. Computer modelling techniques can be of use in providing an atomic-scale understanding of materials, illuminating experimental results and assisting in directing future work and the developmental process.

This thesis details computer modelling studies of novel Li-ion and Na-ion battery materials, with a focus on the latter. A variety of techniques are employed in furthering the fundamental understanding of these materials, and to assist in the development of advanced batteries for next-generation applications. This chapter outlines the fundamentals of rechargeable batteries and then describes a range of materials for Na-ion batteries, highlighting the systems investigated in this PhD project.

1.2 Fundamentals of Rechargeable Batteries

All batteries are electrochemical devices composed of two electrodes, an anode and a cathode, separated by an electrolyte medium. These act as transducers, converting chemical energy into electrical energy and vice versa. The electrodes have differing chemical potentials as a result of their contrasting stoichiometry, crystal structures and chemistry, causing electrons to flow from the more negative to more positive material upon completion of an external circuit. Ion transport through the electrolyte accompanies this electron discharge thereby maintaining charge balance at the electrodes. The driving potential voltage for such flow is directly determined by the difference in electrode chemical potentials. By applying a larger opposing voltage certain cell configurations, known as secondary batteries (as opposed to non-rechargeable primary batteries), can induce ions to flow up the energy gradient from the cathode to anode, into which they intercalate, thereby recharging the battery. The general concept is shown in Figure 1-3 for a typical Na-ion battery [9, 10].

The energy stored per unit mass in a battery is dependent upon the number of ions that can be removed from the electrodes and the difference in chemical potentials. The deliverable power is primarily dependent upon the rate at which ions can be removed from the electrode and transported through the electrolyte. To work effectively whilst avoiding short circuits the electrolyte must be a good ionic conductor but a poor electronic conductor. Interfacial phases (known as the *solid electrolyte interface layer* or *SEI layer*) often develop between electrodes and electrolyte and can have a significant impact on battery properties, as can the degree of side reactions between ions and the electrolyte [11, 12].

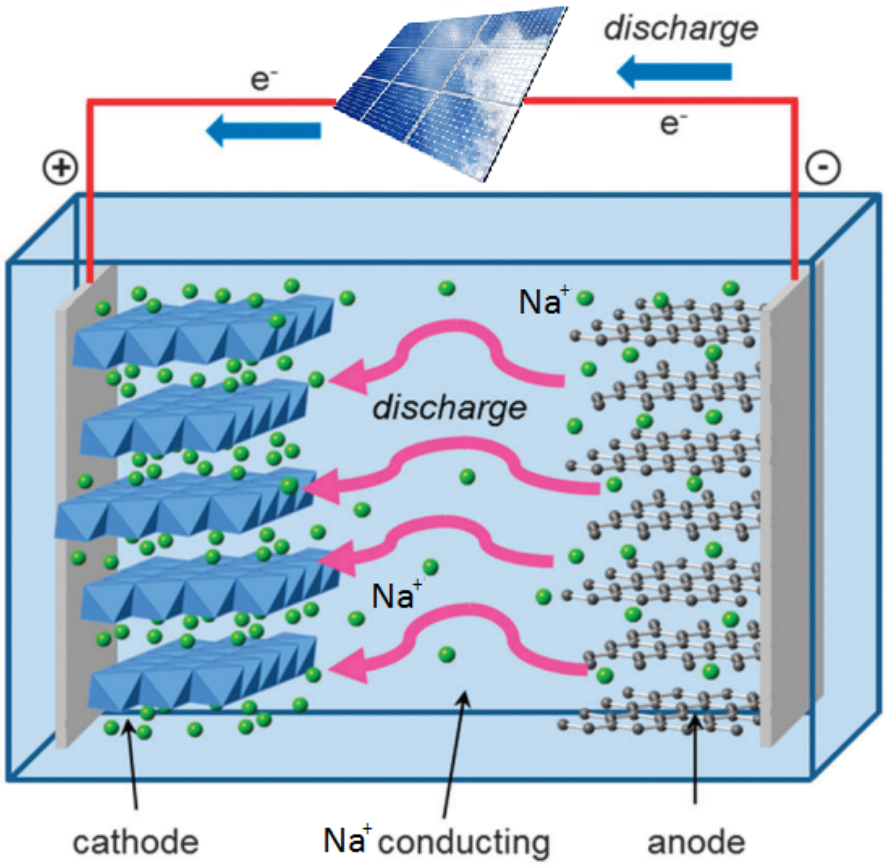

Figure 1-3: *Schematic diagram of a typical Na-ion battery structure, with a layered oxide cathode and carbon based anode. Na^+ ions are depicted as green spheres. Electron and Na^+ flows are reversed upon charging. Adapted from Islam et al. [11]*

Despite being conceptually simple, progress in battery technology has been slow in comparison to other sections of the electronics industry. This is fundamentally a materials science limitation, governed by the paucity of suitable intercalation and electrolyte materials. Myriad electrochemical cell compositions have been proposed, with the most commercially successful primary (non-rechargeable) configuration being Zn-MnO_2 [13]. Secondary batteries have been dominated by lead-acid, Ni-Cd, Ni-MH (MH = metal hydride) and Li-ion configurations [5].

1.3 From Li to Na: Background on Alkali Ion Batteries

Being both the most electropositive and lightest metal (redox potential of -3.04 V vs SHE and molecular weight of $M_r = 6.94$ gmol^{-1}) [14], lithium was first considered as a

charge carrier for high energy density batteries in the 1970's. Moreover, alongside the high theoretical energy density primary lithium cells were soon found to display a host of other advantages. Stable over a wide range of operating temperatures, they coupled a low rate of self discharge to a high and variable discharge rate. As such primary lithium batteries were rapidly incorporated into many small electronic devices, such as calculators and watches [15]. Many of the properties which made lithium attractive for primary batteries were also applicable to secondary batteries, and in tandem research commenced into lithium secondary configurations. This led to the discovery of intercalation compounds, materials into which lithium ions can be reversibly inserted and extracted over repeat cycles. The development of these, typically inorganic, compounds marked a significant turning point in the development of high energy density secondary batteries, the early examples of which are the precursors on which all current Li-ion and Na-ion batteries are based. Ultimately, this led to the first commercial Li-ion rechargeable battery, released in 1990 by SONY, based upon an $LiCoO_2$ insertion cathode and a graphite insertion anode [5, 10]. To date this configuration, and variants thereof, remains the dominant Li-ion battery chemistry for the majority of applications.

Na-ion intercalation materials were originally explored in the 1970's, alongside their Li-ion counterparts. As the second lightest (22.99 $gmol^{-1}$) monovalent metal ion and possessing a high electropositivity (- 2.7 V vs SHE) sodium displays many of the same properties which make lithium appealing as a charge carrier [16]. Some of the first reports of reversible Na^+ intercalation involved transition metal chalcoginides, with TiS_2 and $TiSe_2$ (developed by Exxon) two of the most promising materials [17, 18]. However, subsequent research focused on lithium intercalation cells due to their high energy density and light weight.

Recently, there has been renewed interest in Na-ion batteries. The primary driver of this resurgence has been the recognition that the future electricity infrastructure will require energy storage which is cheaper and more sustainable than current Li-ion systems can provide. Sodium is vastly more abundant than lithium (Na: 5^{th}, Li: 31^{st} most abundant elements in Earth's crust [8] (as shown in Figure 1-4)) and its sources are much more easily accessed. Hence, the raw material cost is typically much lower for sodium compounds, and is unlikely to rise with increasing demand. In addition,

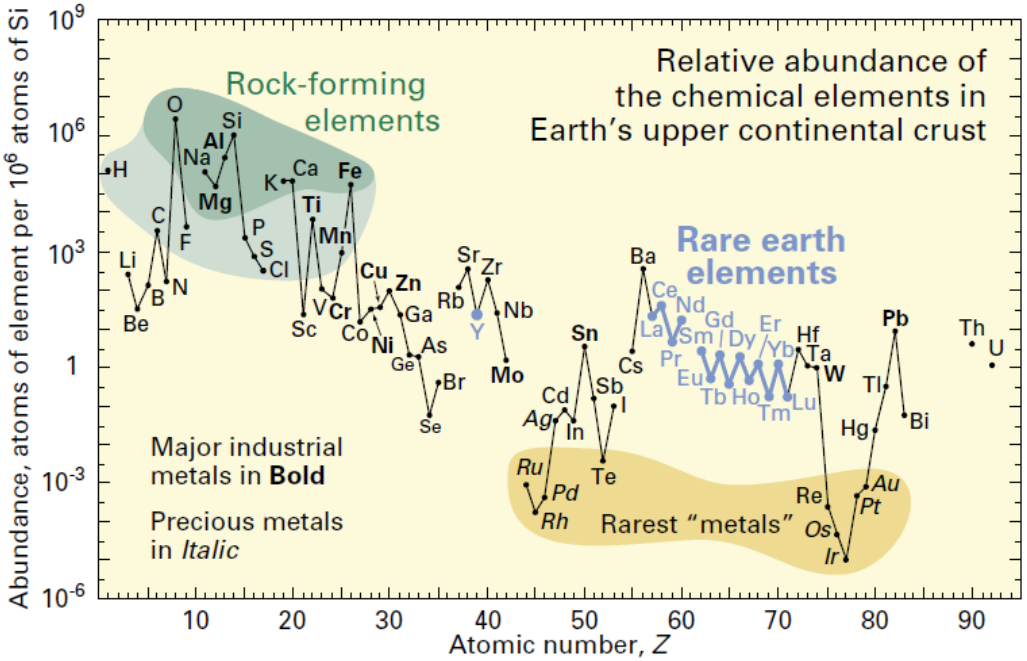

Figure 1-4: *The relative abundance of elements in the Earth's crust, demonstrating the abundance of Na as several orders of magnitude greater than that of Li [19].*

unlike lithium, sodium does not alloy with aluminium and as a result aluminium can be used for the current collectors in the battery architecture, further reducing costs [20]. Alongside these differences sodium demonstrates many of the same advantageous properties as lithium for secondary batteries. Its redox potential, - 2.7 V vs SHE, is only 0.3 V higher than Li and although the ionic radius of Na^+ (1.02 Å) is greater than that of Li^+ (0.76 Å) it displays similar intercalation chemistry [16]. Indeed recent work has suggested that the larger size and lower polarization of the Na^+ ion may lead to better rate performance than that seen in Li-ion compounds [11]. Furthermore, operating at ambient temperature means Na-ion batteries can be made modular, allowing rapid scale up/down of facilities and providing improved safety compared to high temperature batteries (e.g. V-flow, Na-S, ZEBRA [21]).

Despite this, research into materials for Na-ion batteries is still in its infancy and significant work is required before they satisfy all of the properties required for commercial success. Accordingly, at this juncture it is worth reviewing the current state of the art in Na-ion battery materials. The rest of this chapter is intended to provide an overview of the electrolyte, anode and cathode materials most heavily studied for Na-ion batter-

ies. In addition, a more detailed description of selected cathode materials is provided, corresponding to materials explored in this work.

1.4 Na-ion Anode Materials

Analogous to lithium, sodium metal is theoretically the most attractive of all anode materials, with the highest capacity ($\sim$1166 mAhg^{-1}), an order of magnitude higher than current alternatives [22], and the potential to produce cells with the highest voltage. Regrettably upon repeated cycling metallic anodes are known to develop dendritic growths, which eventually extend through the electrolyte to the cathode leading to dangerous internal short circuits [10]. To solve this two approaches are employed, either alternative anode materials can be developed which do not demonstrate dendritic growth, or techniques can be developed to suppress such growth in metallic anodes. The former is the approach most commonly employed in battery research, although research into the latter continues apace [23].

Alternative anode materials are required to have a low potential vs. Na/Na$^+$, with a high capacity to intercalate Na$^+$ ions, along with suitable cycle stability and reversibility. For lithium the current anode of choice is graphite, acting as an intercalation electrode with Li$^+$ inserted between carbon layers. Advantages of graphite include high natural abundance, low cost, good electronic conductivity and relative stability upon cycling. Unfortunately the larger ionic radius of the Na$^+$ ion (1.02 Å vs 0.76 Å) [16] precludes insertion into graphite with adequate kinetics, instead leading to Na plating on the anode surface [21]. This leads to the same problems with dendritic growths experienced by metallic Na anodes. Therefore alternatives to graphite are required. The majority of these alternatives can be classified as either hard carbons, inorganic Ti compounds, or alloying materials.

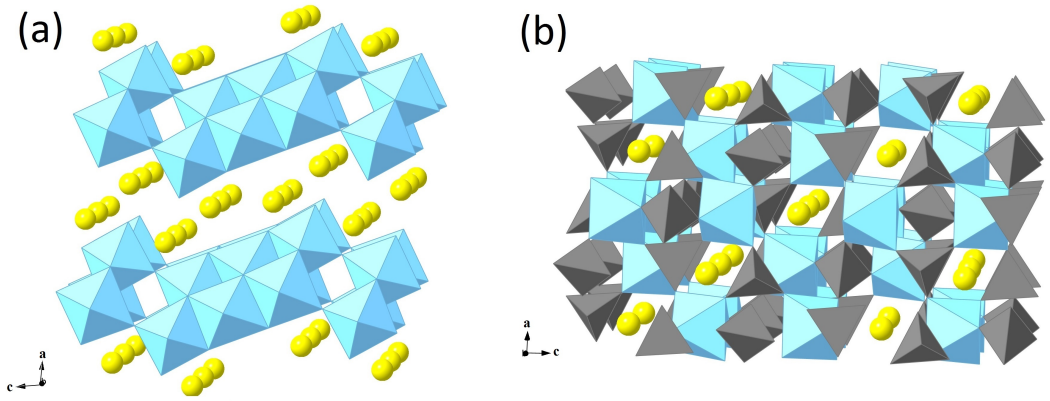

Figure 1-5: *Crystal structures of examples of titanium containing Na-ion anodes, (a)$Na_2Ti_3O_7$ and (b) $NaTi_2(PO_4)_3$. Sodium is shown in yellow, TiO_6 octahedra in blue and PO_4 tetrahedra in grey [27, 28].*

Hard Carbons

In recent years much work has focused upon hard carbon anodes. These are highly porous carbon structures, often derived from the pyrolysis of carbon containing precursors. The choice of carbon precursor and pyrolysis conditions leads to significant variations in the carbon nanostructures produced. Typically these contain both graphene-like and micropore insertion sites, formed between disordered carbon layers [14, 24]. In general these materials can provide around 200-300 $mAhg^{-1}$ at a potential of ~0.3 V vs Na/Na^+ making them highly promising as anode materials [7, 24, 25]. However, it has recently been noted that the potential at which Na^+ intercalate into hard carbons tends to be very close to the potential for metallic sodium. The very low potential afforded by many hard carbons mean they cannot currently be operated at high current densities without the risk of metallic sodium plating [7]. It must also be noted that the insertion characteristics into hard carbon anodes are heavily dependent on the choice of electrolyte and additives. For example, in a recent study a hard carbon anode cycled with an electrolyte composed of $NaClO_4$ dissolved in an ethylene carbonate/diethyl carbonate solution demonstrated high capacity with excellent capacity retention. Conversely, changing the electrolyte solvent to an ethylene carbonate/ethyl methyl carbonate solution lead to poor cycle performance [22]. As such, it is clear that hard carbon research must run in tandem with electrolyte research if it is to lead to a commercially viable anode [7, 26].

Ti oxides and phosphates

A number of titanium based inorganic compounds have received significant attention as Na-ion anodes. Titanium dioxides are of interest due to their exceptional stability, abundance and nontoxicity. Nanosized anatase-TiO_2 has demonstrated a reasonable reversible capacity of <150 $mAhg^{-1}$ at an average potential of 0.8 V vs Na/Na^+. Unfortunately, as with certain oxide cathode materials, larger particles are electrochemically inactive. The importance of size has also been demonstrated for the intercalation of Na^+ ions into amorphous TiO_2 nanotubes [29–34].

The crystal structures of some alternative titanium anodes are given in Figure 1-5. The sodium titanate $Na_2Ti_3O_7$ has been shown to be able to intercalate two Na ions at $\sim$ 0.3 V vs Na/Na^+, corresponding to a capacity of 200 $mAhg^{-1}$ [24, 27, 35, 36]. $Na_2Ti_6O_{13}$ forms a similar structure to the $Na_2Ti_3O_7$ material. However, it affords a considerably lower energy density [37, 38].

Finally NASICON type $NaTi_2(PO_4)_3$ can also be used as an Na-ion anode. Theoretically 2 Na^+ can be inserted/extracted at 2.1 V vs Na/Na^+, leading to a potential capacity of 133 $mAhg^{-1}$. A further voltage plateau exists at 0.4 V vs Na/Na^+ corresponding to insertion of a further Na^+ ion, leading to the fully sodiated $Na_4Ti_2(PO_4)_3$ phase. This has been demonstrated in a symmetrical cell configuration, with $NaTi_2(PO_4)_3$ as both anode and cathode, delivering an operating cell voltage of 1.7 V [39–41]. The relatively low cost, abundance and non-toxicity of Ti compounds mean much work is likely to continue into their use as Na-ion anodes. However, the inclusion of the heavy Ti ion means capacities are unlikely to exceed those of many other potential anodes.

Alloying compounds

In order to improve upon the relatively low capacities offered by hard carbon and Ti containing materials a number of metals and metalloids have been explored as alloying anodes in Na-ion batteries. In particular Sn and Sb have been studied due to their exceptionally high theoretical capacity, although a very large volume change upon cycling typically leads to poor cycle life [21, 42]. Nanostructuring these metals to

produce morphologies which can accommodate the large stresses induced by this volume change is currently being explored. Alternative mitigation techniques involve dispersing nanoparticles in a support network or careful binder selection [43]. Recent work by Liu et al. [44] has demonstrated exceptional capacity retention in Sn nanoparticles embedded in a carbon network. This design lead to a stable capacity of 415 $mAhg^{-1}$ even after 500 cycles at ∼2C rate. Other materials are also being explored as Na-ion alloying anodes with initial work including Ge, In and P, with the latter particularly promising possessing a theoretical capacity > 2000 $mAhg^{-1}$ [45]. Much of this work is continuing in tandem with alloying compounds for Li-ion batteries, which suffer the same disadvantages as in Na-ion systems. To date no alloying anode has been reported with adequate cycle life for typical battery applications [7].

1.5 Na-ion Electrolyte Materials

The electrolyte in a battery must allow the transport of Na^+ ions through the cell, preferably with sufficient conductivity to be a non-rate limiting step, whilst also being electronically insulating so as to minimise self-discharge. In addition, the maximum voltage of the cell is determined by the maximum voltage window at which the electrolyte is thermodynamically stable against decomposition and side reactions, although in practice this window can be extended by kinetic limitations. If a meta-stable configuration is selected then any side reactions must be as slow and predictable as possible. In organic electrolytes this electrochemical stability window is essentially determined by the energy gap between the highest occupied molecular orbital (HOMO) and the lowest unoccupied molecular orbital (LUMO) of the organic solvent. In addition to meet commercial requirements an electrolyte should be thermally, chemically and electrochemically stable, demonstrate low toxicity and be as low cost as possible. Furthermore, it would be preferable to avoid the use of volatile solvents due to safety concerns [6, 7, 10].

The most common electrolyte currently employed in Li-ion batteries is $LiPF_6$ salt dissolved in an organic solvent. Thermodynamic stability extends to 3.5 V vs. Li/Li^+ whilst kinetic limitations raise this stability window to 5.5 V [5]. However, slow elec-

trolyte decomposition still proceeds, diminishing battery performance over the product lifetime. Electrolytes for Na-ion batteries are broadly based upon the same principles as those of Li-ion, with sodium salts dissolved in organic solvents forming the most common group. However, the choice of electrolyte is limited somewhat as sodium salts are typically less soluble than their lithium analogs. As such, considerable effort is being employed in developing suitable organic electrolyte compositions. The choice of sodium salt depends on several crucial properties. Firstly, the solubility of the salt in the solvent or solvent mixture used is essential to generate sufficient charge carriers and conductivity. Secondly, the stability of the salt with respect to both reduction (and oxidation) and the chemical stability with respect to the other materials employed. Finally, the toxicity, cost and safety related aspects are important from commercial considerations. These concerns tend to limit potential salts to those based on anions such as BF_4^-, ClO_4^-, PF_6^-, $CF_3SO_3^-$(Tf) and $[N(CF_3SO_2)_2]^-$(TFSI) [6, 46, 47], although all demonstrate some undesirable properties for Na-ion cells. In academic work the most common salt is $NaClO_4$, however, this is a strong oxidant and as such is not suitable for commercial applications. The TFSI/Tf based salts are very appealing due to a high thermal stability, Na^+ conductivity and non-toxicity. However, they have a tendency to corrode the aluminium current collector. As such there is much work to do in sodium salt development, either through mixtures of currently known compounds or the discovery of new suitable anions [6, 46, 47].

The number of potential solvents is far greater than those of sodium salts. Although solvents must adhere to many of the same requirements as sodium salts they must also contain enough polar groups to adequately dissolve the salts. Furthermore, they require a low melting and high boiling point, with low viscosity and must remain inert with respect to the other materials employed in the full cell. In addition, the choice of solvent can have a significant impact on cell performance and is often electrode specific. For example Vidal-Arbarca et al. [48] demonstrated that in Na_2FePO_4F half cells capacity retention could be greatly increased by moving from a propylene carbonate solvent to an ethylene carbonate:diethyl carbonate mixture. The full variety of solvents is too vast to state here although common solvents include various carbonates (e.g. ethylene carbonate, propylene carbonate), dimethoxyethane or diethyleneglycol dimethylether

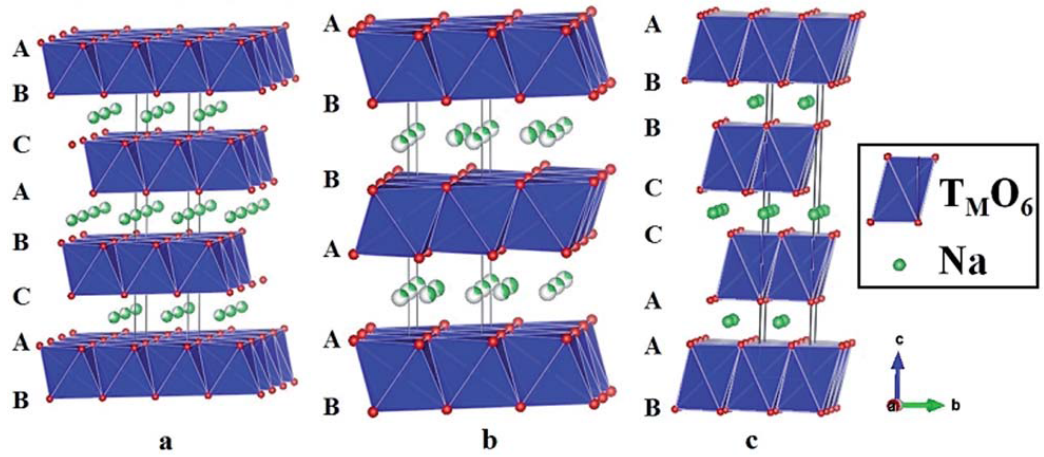

Figure 1-6: *Example of different stacking sequences in sodium layered oxides with (a) O3-, (b) P2-, and (c) P3- type order. Adapted from Rojo et al [50].*

and mixtures thereof. For a more in depth profile of electrolyte research see elsewhere for details [6, 7] .

In tandem, concerns over the safety and cost of organic electrolytes, and their ultimate viability in a commercial cell, mean that alternatives are being sought. These include gel polymer and solid-state electrolytes (see [20, 49] for details), although for the foreseeable future organic based electrolytes are likely to dominate. It is generally recognised that much future work is required in Na-ion electrolyte research, both to optimise current systems and to develop novel chemistries.

1.6 Na-ion Cathode Materials

Given the similarities in Na^+ and Li^+ intercalation chemistry it is perhaps unsurprising that Na-ion cathode research has tended to mimic that of Li-ion. As with lithium, initial work focused on chalcogenides such as TiS_2, TaS_2, $MoSe_2$, and $SnSe_yS_{2-y}$, in which Na^+ can occupy vacant inter-slab sites [18, 24]. However, the poor electrochemical performance of these materials has meant that current cathodes can generally be broken down into *oxides* (both layered and non-layered), and *polyanion* based materials.

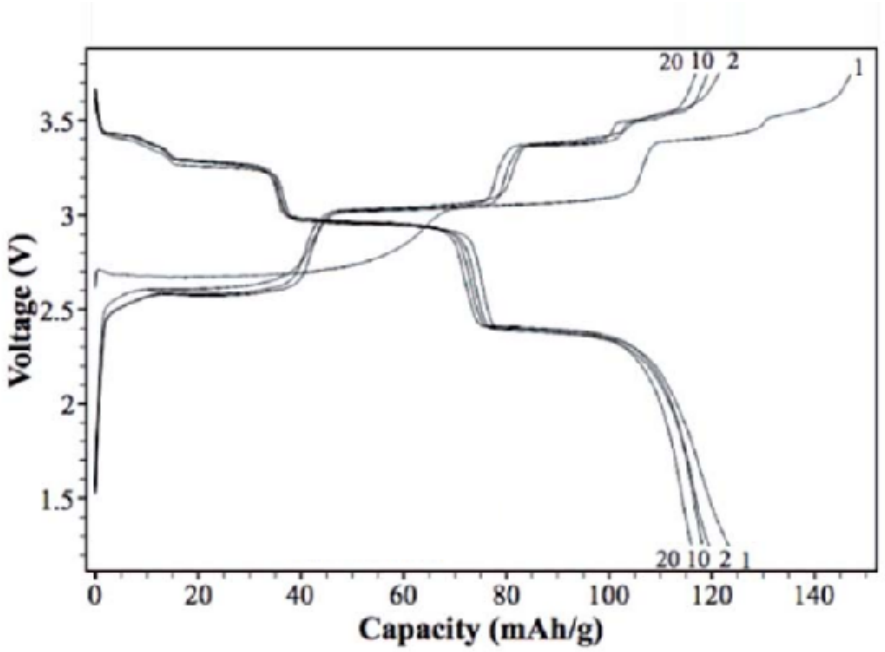

Figure 1-7: *Voltage profile of $NaNiO_2$ over multiple galvanostatical cycles between 1.25-3.75 V at C/10 as an example of the multi-plateau behaviour commonly seen in sodium layered oxides. Reprinted from Vassilaras et al [52].*

1.6.1 Layered and Other Oxide Cathodes

Layered oxides of the formula Na_xMO_2 (where M is a transition metal) have become one of the most prominent areas of Na-ion cathode research. This is largely due to the success of related Li-ion compounds, along with their virtually unassailable theoretical capacity for an intercalation compound. Typically, these materials are formed from sheets of edge sharing MO_6 octahedra, between which Na^+ ions are found. These display a rich degree of polymorphism as the MO_2 sheets glide over one another, leading to variations in both the Na^+ site coordination (octahedral vs prismatic) and the repeat period of transition metal stacking. Such behaviour is not seen in Li-ion analogs, as Li^+ ions do not as a rule occupy trigonal prismatic sites. To classify this polymorphism these materials can be categorised into two groups, with various subsets, as described by the nomenclature devised by Delmas et al.[51] The nature of the Na^+ site is described by O (octahedral) or P (prismatic), followed by a number, describing the number of oxygen layers in the repeat unit [50]. Examples of this are shown in Figure 1-6.

An important feature of these layered oxides is their ability to transition between stacking types upon de/sodiation. For instance, materials synthesised in the O3 phase typically become unstable upon partial sodium extraction. Gliding of the MO_2 slabs, without M-O bond breaking, leads to a transition to a P3 phase. These gliding phenomena are poorly understood, as is their effect on de/sodiation kinetics. Furthermore, transitions can lead to complex voltage profiles making it difficult to find a suitable plateau region for battery operation, perhaps predicating the use of many layered oxides in commercial cells [53]. An example of a layered oxide voltage profile is displayed in Figure 1-7. On the other hand, Na-ion compounds show less of an affinity than Li-ion for reverting to spinel structures and as a result may well be stable over a greater alkali ion concentration, allowing more of the theoretical capacity to be accessed. It is also important to note that transitions that involve M-O bond breaking are not seen at typical battery operating temperatures, as such some transitions (e.g. P3/O3 to P2) are not observed [50]. The full range of oxides under investigation is substantial and beyond the scope of this work, although many excellent reviews exist containing a more complete description of these cathodes [14, 20–22, 24, 50]. Table 1.1 contains a selection of oxide materials that have been reported, along with key material properties. A particularly interesting class of layered oxides are the $Na_xFe_yMn_{1-y}O_2$ group, as these are composed entirely of high natural abundance elements. The Li-ion analogs of these are not thermodynamically stable, as the similar ionic radii of Li^+ and Fe^{3+} mean the more stable structure is rocksalt type [16, 22]. Examples of note include the P2-$Na_{0.6}MnO_2$ material, with hexagonal crystal structure, which has been shown to deliver 140 $mAhg^{-1}$ within the voltage range 3.8-2.0 V. However, extreme volume changes on cycling meant the structure collapsed after a few cycles [54]. Alternatively, the O3-$NaFeO_2$ phase has also been shown to be electrochemically active. A capacity of $\sim$ 100 $mAhg^{-1}$ was accessed at the high average voltage of 3.3 V. Furthermore, the reversible capacity was still 80 $mAhg^{-1}$ after 30 cycles [55]. Another important composition is P2-$Na_{2/3}[Fe_{1/2}Mn_{1/2}]O_2$ as it is the basic Na_xMO_2 oxide currently reported with the highest accessible energy capacity. It has been shown to deliver 190 $mAhg^{-1}$ at 2.75 V vs Na/Na^+ making it highly competitive, even against Li-ion cathodes [56]. These examples demonstrate the exciting layered structures only available to Na-ion materials. As such much future work will likely focus on these compounds.

Table 1.1: *A selection of oxide cathodes reported in the literature.*

Material	Structure	Voltage (V)	Capacity ($mAhg^{-1}$)	Cyclability/Comments
Na_xCoO_2	Layered	∼2.8	120-200	0.5 Na accessed, P2 form displayed best electrochemical performance [57–60]
$NaCrO_2$	Layered	∼3	135	No capacity loss over 50 cycles, 0.5 Na accessed, minimal cation mixing, Na form greater performance than Li analogue [61–63]
$NaMn_{0.5}Ni_{0.5}O_2$	Layered	∼3-3.4	105-130	95% retention after 10 cycles, minimal cation mixing, higher capacity irreversible, variety of structural changes upon cycling [61]
$NaNi_{1/3}Fe_{1/3}Mn_{1/3}O_2$	Layered	2.75	100-120	Good capacity retention for 150 cycles, 0.5 Na reversibly cycled, main expansion in *c* axis [64]
NaV_6O_{15}	Layered	∼2.5	142	Capacity fade to 75% after 30 cycles, kinetic limitations [65]
$Na_{2/3}Co_{2/3}Mn_{1/3}O_2$	Layered	∼3	-	P2 ordering, Co^{3+} and Mn^{4+} oxidation states [66]
Na_xVO_2	Layered	∼1.7	120	No capacity loss over 14 cycles, 0.5Na accessed, Na site coordination preserved during entire cycle [67–70]
$Na_{2/3}Fe_{1/2}Mn_{1/2}O_2$	Layered	2.75	190	99.6% capacity retention over 50 cycles, no carbon coating [61, 71]
$Na_2V_2O_5$	Bi-layered	3	235	80% after 320 cycles, synthesis technique imperative as orthombric form is poor electrochemically [72]
Na_xFeO_2	Layered	3.3	100	80% retention after 30 cycles, small polarization observed [55]
$Na_{0.44}MnO_2$	Framework	2.7	130-140	77% capacity remains after 1000 cycles, kinetic limitations, DFT calculations performed, compatible with aqueous electrolyte, only some Na sites considered accessible [73]
Na_xNiO_2	Layered	∼3	147	Rapid capacity loss, low coulombic efficiency [52]

Oxides crystallizing in non-layered type structures have also been explored as potential electrode materials, with several extensive review articles detailing a variety of oxide compounds [7, 22]. Iron oxides are of great interest due to their very low cost constituents, however, they often require nanosizing to become electrochemically active. One of the most interesting is nanocrystalline Fe_3O_4 which has been shown to reversibly intercalate Na^+ ions with a capacity of 170 $mAhg^{-1}$ and acceptable capacity retention over 30 cycles. However most of its capacity is activated at low potentials, meaning it may be more suitable as an anode material [74]. Other reported iron oxides include β-$NaFeO_2$ and α-Fe_2O_3 [22]. Another transition metal oxide which has received widespread interest is α-V_2O_5, which forms a distinct bi-layered structure. As with Fe_3O_4 nanostructuring is key to realising the large theoretical capacity ($\sim$ 250 $mAhg^{-1}$), with a nanoribbon morphology particularly effective. This delivered close to the theoretical capacity with good cyclability [75]. Conversely, nanoplatelets synthesised through a self-combustion methods dispayed a somewhat reduced initial capacity of 150 $mAhg^{-1}$, with significant capacity fade [76]. In addition, amorphous V_2O_5 has also demonstrated interesting electrochemical performance, with a high capacity [77].

Manganese oxides have been explored as sodium insertion materials since the 1980's. $Na_{0.44}MnO_2$ forms a complex framework structure with two distinct tunnels running parallel to the c-axis. Crystalline nanowires of $Na_{0.44}MnO_2$ have demonstrated a reversible capacity of $\sim$100 $mAhg^{-1}$ with good rate performance and capacity retention. Furthermore, the kinetics and surface stability of $Na_{0.44}MnO_2$ have been shown to be improved upon incorporation into an Al_2O_3/multi-walled carbon nanotube network [73, 78, 79]. Beyond this MnO_2 exists in a wide variety of polymorphs, many of which have been studied as Na-ion intercalation hosts [11, 80–83]. One well known polymorph is λ-MnO_2, which forms in a cubic spinel structure with an open tunnel framework. However, when electrochemically cycled the structure becomes amorphous upon sodium insertion. Despite this 0.6 Na per formula unit could be cycled between 2 - 4 V [84]. Although amorphisation is generally detrimental to cycle life this material continues to be studied for low voltage cells as it is water stable, meaning cheap aqueous electrolytes can be used. Indeed, this configuration is currently being commercialised in aqueous Na-ion cells by Aquion Energy [85]. Another polymorph which has been explored is

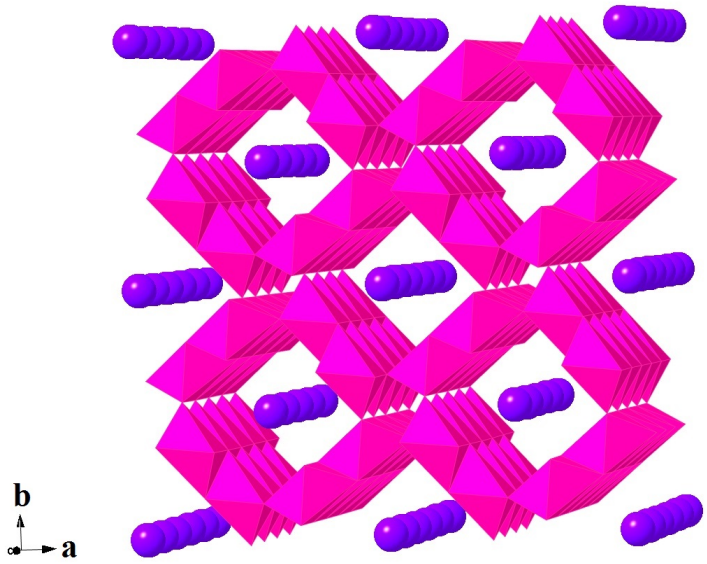

Figure 1-8: *Crystal structure of K^+-stabilised α-MnO_2 with MnO_6 octahedra in pink and K in purple.*

β-MnO_2. This is built of a series of edge and corner sharing MnO_6 octahedra, crystallizing in a rutile structure, forming 1x1 tunnels running parrallel to the c axis. However, these tunnels are too small for Na^+, or even Li^+, insertion and as such bulk β-MnO_2 has been shown to be electrochemically inactive. Conversely, nanosized β-MnO_2 has been shown to be electrochemically active. Nanorods, with preferential growth along the $[\bar{1}\bar{1}2]$ direction and a square cross sectional area of 400 nm^2, have demonstrated a reversible capacity >200 $mAhg^{-1}$ with good capacity retention after 100 cycles [86, 87].

One of the most interesting polymorphs is hollandite α-MnO_2. As with β-MnO_2 the structure is formed of edge and corner sharing octahedra, but in α-MnO_2 larger 2x2 tunnels along the [001] direction are produced, as shown in Figure 1-8. These tunnels can intercalate Na^+ ions along with even larger species including K^+, Li_2O and ammonia. Indeed, it is known that the α-MnO_2 structure is often stabilised by the inclusion of large cations [88]. However, in Li-ion cells α-MnO_2 has struggled with poor capacity retention over many cycles, although both cation inclusion and nanosizing have been shown to alleviate capacity fade, leading to a reversible capacity of 160 $mAhg^{-1}$ [89]. In Li-ion cells, stabilization of the tunnel structure with Li_2O or ammonia leads to good cycling at a capacity of 240 $mAhg^{-1}$ [90, 91]. Previous DFT studies have explored this

stabilization effect and ion migration for Li-ion cells, and even suggested Na^+ migration barriers are comparable to Li^+ barriers [88]. Experimentally nanorods of α-MnO_2 have demonstrated a large reversible capacity (> 200 mAhg^{-1}) in an Na-ion cell, albeit with a large polarization between charge and discharge [86].

In **Chapter 6** stabilization of the tunnels with K^+ is explored in a combined experimental and computational study through a recent collaboration with the microscopy group of Prof. R. Shahbazian-Yassar at Michigan Technological University, USA. The α-$K_{0.25}MnO_2$ stoichiometry is detailed, with its effect on the growth mechanism and morphology of the as synthesised nanorods studied on a fundamental level.

1.6.2 Polyanion-type Cathodes

Na-based polyanionic materials are interesting candidates for grid storage applications. In part this is because, with the oxygen being tightly bound into polyanionic groups, the compounds are intrinsically more stable against oxygen evolution. As such, the risk of self ignition upon cycling is greatly reduced. Furthermore, they generally contain abundant constituent elements, and display great variations in composition and material properties. In addition, their lower theoretical capacity is less of an issue for grid storage technologies. To date research into polyanionic compounds has generally focused on NASICON-type materials, $NaMPO_4$ (related to $LiFePO_4$), and various phosphate based compounds. A summary of these materials can be found in Table 1.2 and extensive reviews can be found elsewhere [7, 11, 20–22, 24].

Na super-ionic conductors, NASICONs (general formula $Na_3M_2(XO_4)_3Y$ where M is a transition metal, X=P,S,Si and Y=F,OH), were originally studied as solid electrolytes for Na-S batteries as their open framework, with wide Na^+ diffusion channels, allows facile Na^+ migration. The framework structure is composed of corner sharing MO_6 and XO_4 polyhedra. In 1987 certain NASICON stoichiometry were shown to be electrochemically active, with reversible de/sodiation [40]. Since then a number of transition metals (M=Ti,V,Fe...) have been studied for use in Li-ion and Na-ion batteries. The most widely studied, $Na_3V_2(PO_4)_3$ has demonstrated a capacity of 93 mAhg^{-1} at a

Table 1.2: *A selection of polyanionic Na-ion cathodes reported in the literature.*

Material	Structure	Voltage (V)	Capacity ($mAhg^{-1}$)	Cyclability/Comments
$NaFePO_4$	Olivine	2.7	125	More than 90% retention after 50 cycles, 80% theoretical capacity accessed [92, 93]
$NaVPO_4F$	3D framework	3.7	82	Less than 50% retention after 30 cycles, full cell constructed [94]
$Na_3V_2(PO_4)_3$	NASICON-type	1.63/3.4	95/235	Steady capacity over 20 cycles, removed 2Na and inserted 4Na to get high capacity (117 $mAhg^{-1}$ if 2Na inserted), poor electronic conductivity [95–99]
$Na_3V_2(PO_4)_2F_3$	VO_4F_2/PO_4 framework	4.1	120	90% capacity retention after 220 cycles, 2Na reversibly cycled, low volume change [100–102]
$NaFeSO_4F$	Tavorite	3.55	$\sim$10	Limited performance, Na poorly accessible [103]
$Na_2FeP_2O_7$	Isostructural to $Na_2CoP_2O_7$	$\sim$3	82	82% theoretical capacity accessed, high rate capability [104, 105]
$Na_{1.5}VOPO_4F_{0.5}$	Layered	3.7/4.1	87	84% capacity retention after 500 cycles, high voltage plateau loss due to cell polarization, 0.56Na accessed [106, 107]
Na_2FePO_4F	Layered	3.3	135	80% capacity retention after 750 cycles, high rate performance through nanostructuring, low volume change [108–111]
$Na_2Fe_2(SO_4)_3$	Framework	3.8	102	Single phase reaction with small volume change [112]
$Na_4Fe_3(PO_4)_2P_2O_7$	Frameowrk	3.0	135	86% capacity retention after 100 cycles, low volume change [113]

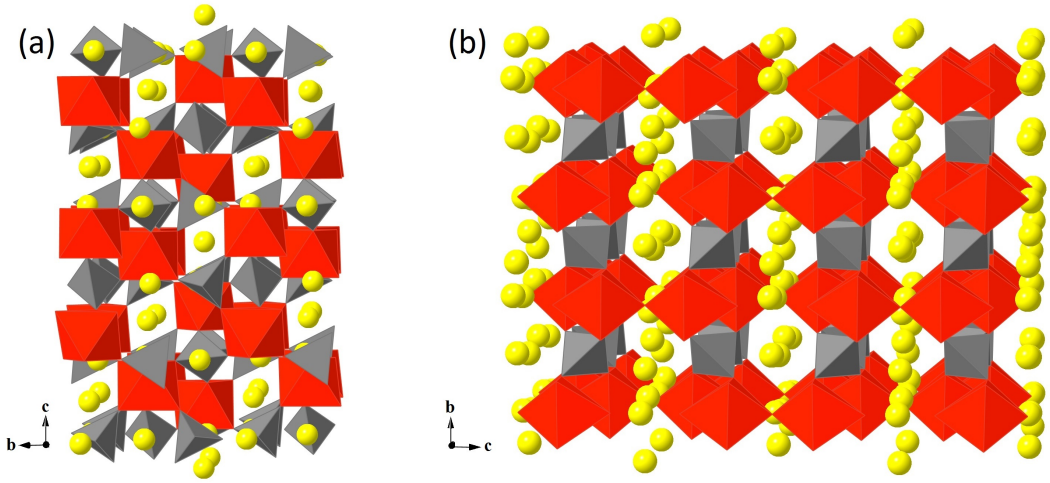

Figure 1-9: *The crystal structures of selected vanadium based Na-ion cathodes, with (a)$Na_3V_2(PO_4)_3$ and (b) $Na_3V_2(PO_4)_2F_3$. Sodium is shown in yellow, VO_6 octahedra in red and PO_4 tetrahedra in grey [114, 115].*

voltage plateau of 3.40 V vs Na/Na^+ ($V^{3+/4+}$) and a further 59 $mAhg^{-1}$ at 1.63 V ($V^{2+/3+}$) with good cyclability, particularly when nanosized. In addition, there have been studies into using this material as both anode and cathode in a symmetrical cell, due to the large voltage difference between plateaus. Such cells have been shown to reversibly deliver 64 $mAhg^{-1}$ [20, 95, 96, 116]. However, delivering capacity over such a broad voltage range is detrimental to stored energy density. Indeed, the exceptionally low energy densities afforded by NASICON compounds is a significant hindrance to their use in commercial Na-ion cells. Despite this the huge range of stoichiometries available to NASICON-type materials mean a great deal of future work is likely to be undertaken, exploring the broad composition space.

Further research on polyanion-type compounds has tended to focus on phosphate derivatives, employing V, Fe or Mn as the framework transition metal. Vanadium containing compounds are attractive due to their high energy density. The sodium vanadium fluorophosphate $Na_3V_2(PO_4)_2F_3$ has shown excellent rate capability, delivering 95 $mAhg^{-1}$ with two voltage plateaus at 3.65 and 4.1 V vs Na/Na^+. In addition, a volume change upon cycling of just 1.8% is indicative of good cyclability of the material [100, 117]. A recent combined experimental and computational study attributed the good cyclability to how the Na^+ site occupancies vary upon cycling so as to accommodate the stress [118]. The compound $Na_3(VO_2)(PO_4)_2F$ is based on the same

framework and has also shown high performance with 100 $mAhg^{-1}$ accessed at a 1C rate on voltage plateaus of 3.6 and 4.0 V vs Na/Na^+ [106]. The crystal structure of two vanadium based cathodes are shown in Figure 1-9. This family also includes the $NaVPO_4F$ material, which has recently been shown to provide excellent cyclability with an initial capacity of 121 $mAhg^{-1}$ when synthesised as a $NaVPO_4F$/graphene composite [119].

However, disadvantages with vanadium compounds include the difficulty of working with vanadium, some oxides of which are toxic, and the low elemental abundance as opposed to alternative transition metals [120]. Cathodes based on Fe or Mn, which are more benign and abundant, have also been explored. Pyrophosphates offer a robust and stable $(P_2O_7)^{4-}$ framework, with multiple sodium sites and potential migration pathways. The iron pyrophosphate $NaFe(P_2O_7)$, shown in Figure 1-10(a), has been shown to provide a capacity of 82 $mAhg^{-1}$, delivered predominantly at 3 V (with a small 2.5 V region) vs Na/Na^+ and a small volume change of just 2.1% [104].

The mixed phosphate-pyrophosphates $Na_4M_3(PO_4)_2(P_2O_7)$ have also received some attention, particularly M=Fe, for similar reasons to the pure pyrophosphate. In addition, they demonstrate particularly high thermal stability. Operating at 3.2 V vs Na/Na^+ $Na_4Fe_3(PO_4)_2P_2O_7$ can deliver ~100 $mAhg^{-1}$ at C/20 rates corresponding to the exchange of 3 Na^+ ions [121, 122]. The $Na_4M_3(PO_4)_2P_2O_7$ (M = Fe, Mn, Ni, Co) class of materials are discussed in more detail in **Section 1.9**. Finally, two of the most heavily studied phosphate based compounds are $NaFePO_4$ and Na_2FePO_4F, due to the success of similar lithium cathodes, and are discussed in considerable detail in **Sections 1.7** and **1.8** respectively.

Beyond the phsophates, sulfate based cathodes have recently been explored, including $Na_2M(SO_4)_2 \cdot nH_2O$ and alluaudite-type $Na_2Fe_2(SO_4)_3$. Both bloedite and krohnkite-type polymorphs of $Na_2Fe(SO_4)_2 \cdot nH_2O$ have been shown to be electrochemically active, with average voltages of 3.3 V and 3.25 V vs Na/Na^+ respectively. However, upon cycling water is lost from the structure resulting in amorphisation, limiting cycle life. The $Na_2Fe_2(SO_4)_3$ material has one of the highest voltages, at 3.8 V vs Na/Na^+, of any polyanionic cathode. This is a result of its unique structure of edge sharing FeO_6

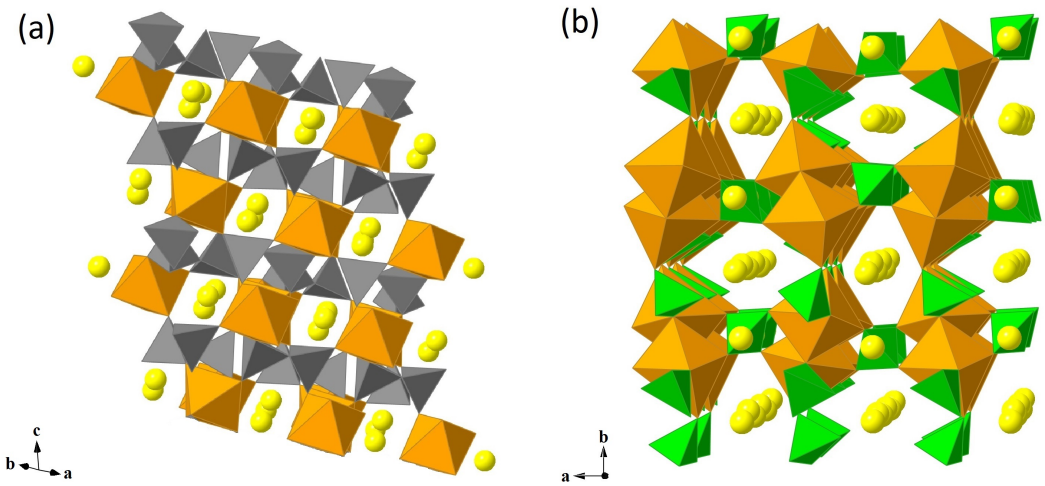

Figure 1-10: *The crystal structures of selected polyanionic Na-ion cathodes, with (a)$NaFe(P_2O_7)$ and (b) $Na_2Fe_2(SO_4)_3$. Sodium is shown in yellow, FeO_6 octahedra in brown, PO_4 tetrahedra in grey and SO_4 tetrahedra in green [112, 123].*

octahedra (see Figure 1-10(b)). A reversible capacity of 102 $mAhg^{-1}$ has been accessed, corresponding to 85% of the theoretical capacity. Furthermore, a volume change of just 1.6% upon de/sodiation is promising for high reversibility and rate performance [112, 124–126]. As with NASICON materials the considerable size of configuration space available to polyanionic materials suggests much future work will be conducted in this area. To conclude this introduction chapter, detailed descriptions of the three main types of polyanionic material explored in this PhD project are presented.

1.7 Novel Polyanion Cathode: $NaFePO_4$

The most successful polyanionic Li-ion cathode is $LiFePO_4$. Hence, initial work has focused on the sodium analog, $NaFePO_4$, and related compounds (e.g. $NaFe_{0.5}Mn_{0.5}PO_4$, $NaMnPO_4$) [92, 127–129]. However, the olivine structure of $LiFePO_4$, which provides open channels for Li^+ migration, is not the most thermodynamically stable polymorph of $NaFePO_4$. Instead it crystallises in the maracite structure, which can be envisaged as the olivine material but with the Na^+ and Fe^{2+} switching lattice sites. The resultant framework does not provide channels for facile Na ion migration, and is generally found to be electrochemically inactive [130]. However, through delithiation of $LiFePO_4$

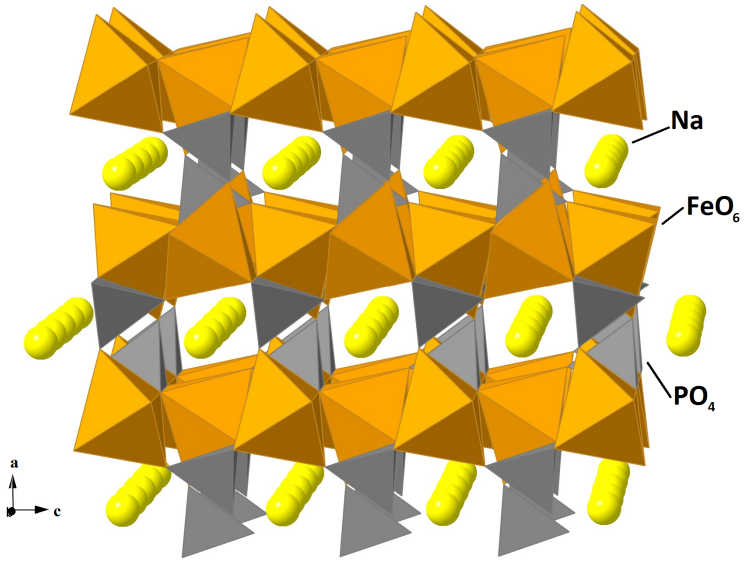

Figure 1-11: *Crystal structure of olivine $NaFePO_4$ with Na in yellow, FeO_6 octahedra in brown and PO_4 in grey [132].*

and subsequent sodiation olivine $NaFePO_4$ has been produced, the structure of which is given in Figure 1-11 [92]. In the olivine $NaMPO_4$ structure (space group: Pnma, M = Fe,Mn), MO_6 octahedra link to each other via corner sharing in the *ab* plane. Sandwiched between these planes are PO_4 tetrahedra which share corners and edges with the MO_6 octahedra. This well-known framework provides open channels along the *b*-axis in which Na^+ ions are located. A unique ordered composition, $Na_{0.7}FePO_4$ is also reported to form on electrochemical oxidation of $NaFePO_4$, with an associated step in voltage plateau, although its precise structure has not yet been elucidated [131].

Conflicting reports have emerged regarding the electrochemical properties of olivine $NaFePO_4$. While an initial study by Moreau et al. [131] indicated that carbon coating of the parent material, $LiFePO_4$, did not impact the electrochemical performance of olivine $NaFePO_4$, recent investigations by Zhu et al. [129] has demonstrated superior electrochemical properties upon carbon coating. A reversible capacity of ~100 $mAhg^{-1}$ at 0.1 C rate is considerably higher than that obtained without carbon coating, although the performance is still inferior to that of the carbon coated lithium analogue. In addition, a volume change of 17.58% upon de/sodiation may prove to be problematic for cycle life and rate performance [92, 128]. The mixed Fe-Mn system $NaFe_{0.5}Mn_{0.5}PO_4$ was also synthesised recently by direct methods [133], and it gives a characteristically

sloping electrochemical profile when cycled in an Na-ion battery. This material has demonstrated a reversible capacity of 125 $mAhg^{-1}$ (80% of theoretical capacity) at 2.7 V vs Na/Na^+ and excellent capacity retention after 50 cycles. Due to the success of $LiFePO_4$ a considerable body of work is continuing on the sodium analog.

1.8 Novel Polyanion Cathode: Na_2FePO_4F

The Na-ion cathode Na_2FePO_4F displays many attractive properties: composed of earth abundant elements and possessing an open layered structure (shown in Figure 1-12), it has been shown to be electrochemically active towards reversible Na^+ intercalation [103]. The material is based upon a *Pbcn* spacegroup, isostructural to Na_2FePO_4OH rather than Na_2MnPO_4F. The Fe is situated in a 6-coordinate environment involving 4 oxygen and 2 fluorine, with two adjacent octahedra face sharing to form dimer like $Fe_2O_6F_3$ bioctahedra. Bioctahedra are connected through a corner shared F along the *a* direction, and PO_4 tetrahedra along *c*. This leads to alternating layers of Na_2 and $FePO_4F$. Within the sodium layers exist two distinct Na sites, both possessing [6+1] fold coordination involving 4 oxygen and 2 fluorine with an additional oxygen somewhat removed from the direct environment. The two sites differ in overall size, with the Na2 site being more compact than the Na1 site.

Early reports on the electrochemical performance of Na_2FePO_4F as a cathode for Na-ion cells have been promising. The theoretical capacity, assuming Na extraction to $NaFePO_4F$, is 135 $mAhg^{-1}$, with current reports suggesting 85% of theoretical capacity can be reversibly accessed at low rates (0.1C) and at an average voltage of 3.3 V [130]. Furthermore, upon cycling a volume contraction of just 3.7 % has been observed. At higher rates (5C) a capacity of 80 $mAhg^{-1}$ was accessed, whilst the material retains 80% of initial capacity after 750 cycles at a 1C rate [108]. However, such performance has only been achieved through the inclusion of $\sim$5 wt% carbon. This is to compensate for the low intrinsic electronic conductivity, which has been ascribed to electron localization due to the high ionicity of fluorine. Sodium migration is assumed to be predominantly 2-D in nature, with limited motion between sodium layers. Sodium extraction demonstrates solid solution like behaviour with a slight structural distor-

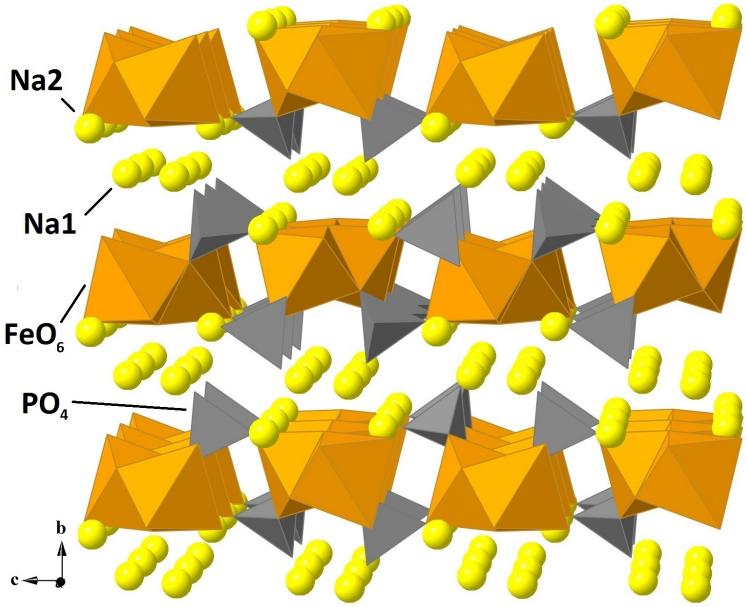

Figure 1-12: *Crystal structure of layered Na_2FePO_4F with Na in yellow, FeO_6 octahedra in brown and PO_4 tetrahedra in grey [103].*

tion (β = 91.22 °) at a composition of $Na_{1.5}FePO_4F$, driven by electron localization of Fe^{2+}/Fe^{3+}. The Na2 sites are considered less stable than the Na1 sites, and complete extraction (to $NaFePO_4F$) results in almost all remaining Na^+ residing on the Na1 sites. Many approaches to improving the electrochemical performance of electrode materials revolve around the reduction of particle size to the nanometre scale. As such, much work has focused on using synthesis conditions and techniques to influence electrochemical performance and nanoparticle properties [102, 134–136]. A number of synthesis methods have been employed in the fabrication of Na_2FePO_4F cathodes including solid-state [103, 111, 137], hydrothermal [109], spray pyrolysis [108, 136], and solgel [138] techniques, leading to a wide range of particle sizes and morphologies. Commonly, the various approaches lead to nanosize granular particles [103, 135, 137] but other morphologies have been found, such as hollow nanospheres [108] and nanorods [103].

Given the promise of Na_2FePO_4F there is still little in the published literature in the way of computational modelling studies. As such, the atomistic insights into defects and ion diffusion that can be gleaned from such work are yet to be realised and are explored in **Chapter 3**. This work was performed in tandem with simulations of

$NaFePO_4$ to identify how different structural features lead to contrasting electrochemical properties. This study is extended in **Chapter 4** to include an examination of the surface structures, energetics and morphology of Na_2FePO_4F.

1.9 Novel Polyanion Cathode: $Na_4M_3(PO_4)_2P_2O_7$ (M=Fe, Co, Ni, Mn)

A family of compounds, based upon a mixed phosphate-pyrophosphate framework, have recently gained interest as novel Na-ion cathodes. These materials, given by the formula $Na_4M_3(PO_4)_2P_2O_7$ (where M=Fe, Co, Mn and Ni), adopt isostructural metal-phosphate framework structures (shown in Figure 1-13). The materials can essentially be envisioned as composed of MO_6 octahedra and PO_4 tetrahedra, which combine to form $[M_3P_2O_{13}]_\infty$ layers running parallel to the *bc* plane. These layers are then connected by P_2O_7 groups which run parallel to the *a* axis. This framework can be indexed with a $Pn_{21}a$ space group, providing a three dimensional tunnel structure, with intersecting tunnels running along the [100], [010] and [001] directions. Na^+ ions are located in four distinct sites within this complex tunnel system. Although this network is essentially three dimensional in nature it should be noted that tunnels running parallel to the *b* axis are particularly spacious and promising for Na ion diffusion [113, 121, 139]. Since these materials exhibit an isostructural framework structure a potential route to turning the material properties may be through varying transition metal combinations. The theoretical capacities of these mixed phosphates are in the region of 170 $mAhg^{-1}$; making them highly competitive with other Na-ion cathodes.

The compounds were first studied for their electrochemical properties in 2001 by Sanz et al. [121] whereupon the analogs corresponding to M=Co, Ni and Mn were studied, and Na^+ diffusion measurements taken. The ionic conductivity of Na^+ was shown to increase from 2.1×10^{-7} Scm^{-1} to 2.7×10^{-5} Scm^{-1} at 575K as the transition metal was changed from Ni to Co to Mn. This increase was attributed to a lengthening in selected Na-O bonds upon moving from Ni to Mn. This was predicted to have the effect of increasing the dimensionality of diffusion, by improving conductivity along the *a* axis,

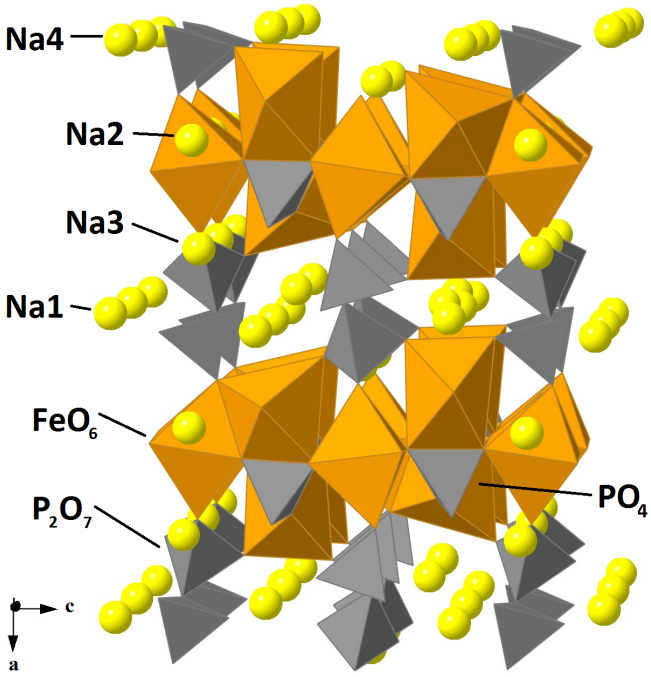

Figure 1-13: *Crystal structure of $Na_4Fe_3(PO_4)_2P_2O_7$, isostructural with the Co, Ni and Mn analogs. The sodium is given in yellow, FeO_6 octahedra in brown and PO_4 tetrahedra in grey [113].*

thereby linking better to the tunnel situated in the *bc* plane. The two most studied analogs in recent literature are those involving the Fe and Co transition metals. The $Na_4Fe_3(PO_4)_2P_2O_7$ mixed phosphate has been studied by Kang et al. [113] (along with its Li equivalent), and demonstrated a capacity of 129 $mAhg^{-1}$ delivered at ~3.2 V vs Na/Na^+. Furthermore, the lithium compound displayed a reasonable capacity retention of 86% initial capacity after 100 cycles and good rate performance, maintaining 75% capacity upon moving from a C/20 to 1C rate. Perhaps most importantly for large scale battery operation a small volume change upon cycling (<4%) and high thermal stability, were singled out in $Na_4Fe_3(PO_4)_2P_2O_7$ cathodes [113, 139]. Nose et al. [122] have investigated the electrochemical properties of the $Na_4Co_3(PO_4)_2P_2O_7$ material, and achieved a reversible capacity of 95 $mAhg^{-1}$ delivered at two plateaus of 4.1 V and 4.7 V vs Na/Na^+, with negligible capacity fade after 100 cycles. Of significant interest is the demonstrated rate performance with a capacity of 80 $mAhg^{-1}$ still maintained even at extreme 25C discharge rates.

An understanding of these materials would also provide insight into the effect of dif-

ferent transition metal cations on an otherwise essentially unchanged material framework. Furthermore, it is instructive to explore how the electrochemical properties of this isostructural class of materials vary across the transition metal series. Therefore, a computational study of these materials is detailed in **Chapter 5** concerning the defect, structural and ion diffusion properties on an atomic scale. In addition, the voltage trends of selected mixed transition metal systems have been studied, as a method for tailoring the electrochemical properties of the materials.

Having introduced the materials explored in this PhD project, the next chapter describes the computational methods used. After which the results of the studies are presented.

2 Computational Methods

"The universe... stands continually open to our gaze, but it cannot be understood unless one first learns to comprehend the language and interpret the characters in which it is written. It is written in the language of mathematics..."

Galileo

Computer modelling is now a well established set of techniques employed in the study of solid state materials, allowing the investigation of a wide variety of properties over diverse length and time scales. The majority of the techniques available are based on one of two approaches: one in which the focus is on describing the motion of atoms or ions at a simplified level of theory, and another based upon a description of the electronic structure of a material. Both methods have found many uses in computational materials science to describe a range of phenomena, and both have been employed in this work.

Within this thesis techniques detailing the atomic or ionic motion, based on atomistic models describing interactions with a series of interatomic potentials, have been used extensively in the study of structures, defects and ion transport. These have been performed with both static lattice methods, conducted within the General Utility Lattice Program (GULP) [140], and molecular dynamics methods, implemented in the

DL_POLY [141] and LAMMPS [142] codes. In addition, *ab initio* electronic structure techniques, under the framework of density functional theory (DFT) have been conducted in the Vienna Ab Initio Simulation Package (VASP)[143, 144]. DFT has been applied to understanding the electronic structure of battery materials along with related properties such as voltage, phase stability and surface energetics. An overview of both potentials-based and electronic techniques is given in this chapter. Many excellent texts are available for a more in depth discussion of these simulation methods [145–152].

2.1 Atomistic Simulations

Atomistic simulations encompass a range of well-established techniques that have been used to study a rich variety of solid state materials and properties. They involve several components. Initially a suitable potential model, often incorporating the polarizability of ions, is developed and fitted to known experimental data. Constraints are then applied to simulate a particular phenomena or process. The system is then minimised with respect to a suitable thermodynamic property, typically the total energy of the system (although usually it is the forces on such a system which are minimised as, under certain constraints, this is equivalent to a full energy minimisation). Various methods exist to do this and are discussed in **Section 2.1.3**. Simulations of defects and single ion migration are considered in **Section 2.2**, whilst molecular dynamics simulations are detailed in **Section 2.3**.

2.1.1 Energy Surface

The basis of atomistic simulations is the Born model of solids, which states that the energy of a system can be described by a function of the atomic coordinates, that is

$$U = f(\mathbf{x}) \tag{2.1}$$

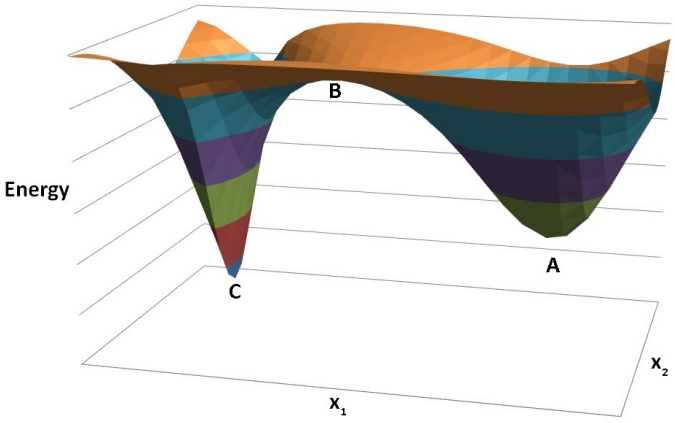

Figure 2-1: *Example of a two dimensional energy surface demonstrating important features such as local minima (A), global minima (C) and saddle points (B).*

where U is the potential energy of the system, and $\mathbf{x}$ is the Cartesian space vector of all atoms in the solid. For a system containing N atoms, $\mathbf{x}$ will take the form of a vector containing $3N$ elements. This function defines the energy surface in atomic coordinate space. For real systems this will be described by a multidimensional hypersurface, however, a simpler 2 dimensional surface is shown in Figure 2-1. Exploration of the energy surface is the basis of atomistic simulations, with two main surface features significant: minima and saddle points.

Minima refer to points on the energy surface for which $f(\mathbf{x})$ is at a minimum with respect to infinitesimal displacements in all atomic coordinates, represented in Figure 2-1 by points A and C. The global minima is the lowest point on the entire energy surface, demonstrated in Figure 2-1 by point C. Global minima of real systems describe the most thermodynamically stable configuration of the atomic coordinates. Alternatively minima can be local, as shown in Figure 2-1 point A. These are a minimum with respect to infinitesimal displacements in $f(\mathbf{x})$, but are not the lowest point on the energy surface. Since experimental ion positions are often known local minima are typically of the most interest, referring to the stable configuration of the polymorph under study. Finally, saddle points are locations on the energy surface which are a minima with respect to one or more atomic coordinates, but a maxima with respect to one or more alternate coordinates, as seen in Figure 2-1 point B. These relate to transition points in the system and are important for topics such as ion migration, defining the activation energy of the process.

Accurately defining the energy surface, through developing a suitable $f(\mathbf{x})$, is essential. To a significant degree the accuracy and reliability of results produced depends upon the extent to which the model developed represents the true energy surface of the system.

2.1.2 Potential Model

Interatomic potential simulations use the lattice energy, U_{LAT}, as the energy surface and describe it through a series of terms which represent interatomic interactions as a function of atomic coordinates ($\mathbf{x}$). The lattice energy is defined with respect to constituent ions placed at infinity, making it amenable to a Born-Haber cycle.

The most general form of interatomic potential is a series of the form

$$V(r) = \sum_{ij} V_{ij}(r_{ij}) + \sum_{ijk} V_{ijk}(r_{ijk}) + ... \tag{2.2}$$

describing interactions as a function of the interatomic separation $r_{ij..}$. However, this is often truncated at the pair potential, or limited three body level, as the pair potentials are the most significant terms. These are typically composed of an electrostatic contribution coupled to a short range potential

$$V_{ij}(r_{ij}) = \frac{q_i q_j}{4\pi\epsilon_0 r_{ij}} + \psi_{ij}(r_{ij}) \tag{2.3}$$

where q_i and q_j are the atomic charges, r_{ij} is as defined above and ψ_{ij} is the short range interatomic interaction. Many forms exist for $\psi_{ij}(r_{ij})$, parameterising the short range interactions in a variety of ways. One of the most popular forms is the Buckingham potential, given by

$$\psi_{ij}(r_{ij}) = Aexp(\frac{-r_{ij}}{\rho_{ij}}) - \frac{C}{r_{ij}^6} \tag{2.4}$$

where A, C and ρ_{ij} are variable parameters. This potential has reasonable theoretical underpinnings, including as it does an attractive r_{ij}^{-6} term describing Van der Waal interactions and a repulsive exponential term related to the interpenetration of electron shells. However, many other forms for the pair potentials have been developed, all with slightly different mathematical descriptions. A list of commonly used potentials is given in Table 2.1. Of particular note due to their popularity are the Morse and Lennard-Jones potentials. The exact form used is often somewhat arbitrary as all functions are attempting to describe the same interaction, and as such can often be fairly accurately mapped onto one another, with little loss of information.

Table 2.1: *Selected interatomic potentials commonly used in atomistic modelling.*

Potential	**Form**	**Parameters**
Buckingham	$Aexp(\frac{-r_{ij}}{\rho_{ij}}) - \frac{C}{r_{ij}^6}$	A, ρ, C
Morse	$D_e[(1 - exp(-a(r - r_0)))^2 - 1]$	D_e, a, r_0
Lennard-Jones	$\frac{A}{r^m} - \frac{B}{r^n}$	A, B, m, n
Harmonic	$\frac{1}{2}k_2(r - r_0)^2 + \frac{1}{6}k_3(r - r_0)^3 + \frac{1}{24}k_4(r - r_0)^4$	k_2, k_3, k_4, r_0
General/Del Re	$\frac{Aexp(-\frac{r}{\rho})}{r^m} - \frac{C}{r^n}$	A, ρ, m, n
Inverse Gaussian	$-A(-b(r - r_0)^2)$	A, b, r_0
Stillinger-Weber	$Aexp(\frac{\rho}{r - r_{cutoff}})(\frac{B}{r^4} - 1)$	A, B, ρ, r_{cutoff}

It is important at this point to state explicitly some additional constraints and assumptions relating to the potentials described thus far. Firstly, integral ionic charges are generally employed in calculations, to avoid problems arising when attempting to correctly model the cohesive properties of the crystal lattice. Secondly, taking the Buckingham form as an example, the parameters A,ρ_{ij}, and C are variable parameters within the potential model and are typically derived through *observables fitting* as discussed later. Finally, it must be stated that although the potentials described above theoretically extend to infinite distances such a situation cannot be simulated directly. As such, the potential is *cut-off* at some predefined value of r, which must be chosen such that it is large enough for the potential to converge to a suitable degree of accuracy whilst being small enough to limit the computational time expended.

Polarisability

To accurately model the crystal lattice it is often necessary to include the effect of polarization, distortion of the ions electron clouds, of the system. For example polarization resulting from the electric field introduced by a point defect will significantly affect lattice relaxation around the defect ion. The simplest model of polarization is the point polarizable ion (PPI) model, in which a polarizability α is assigned to each ion leading to a dipole moment μ, in electric field E.

$$\mu = \alpha E \tag{2.5}$$

However, this formulation fails to account for the coupling that arises in solids between polarization and short-range repulsion. The effect of short-range repulsion, resulting from the overlap of electron clouds, will be significantly affected by the degree of polarization induced in the system. In general this coupling acts to dampen polarization, and as such the PPI model tends to overestimate the polarization of a system. A simple and highly successful model which includes this coupling is the *shell model* developed by Dick and Overhauser [153]. The model includes polarization mechanically, whereby a massive ion core (containing the nucleus and inner electrons) is connected to a massless shell (representing the valence electrons) via a harmonic spring. A dipole moment is introduced through the displacement of the shell away from the core. This is shown schematically in Figure 2-2. The resulting polarizability of an ion is given by the relationship

$$\alpha = \frac{Y^2}{k} \tag{2.6}$$

where α is the polarizability of the ion. It should be noted that the constants k and Y are treated as variable parameters, and are used in empirical fitting of the model. The model has had great success in reproducing the properties of real systems, and as such is deployed in the majority of atomistic simulations in this work.

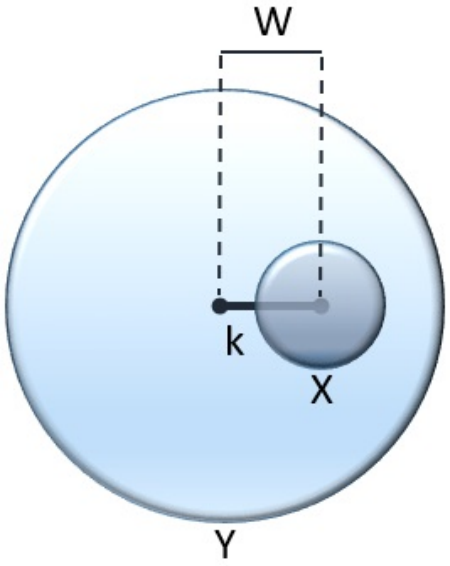

Figure 2-2: *Schematic of the shell model of polarizability. The ion core has charge X and the shell charge Y, with the two displaced by a distance W, whilst connected by a harmonic spring of constant k.*

Potential Fitting

It is essential to determine to what extent the energy surface generated by a model function correlates with the actual energy surface of the system. This is performed by determining the degree to which the model reproduces observed properties of the system, either from experimental data or *ab initio* calculations. Generally, the most widely available data is crystal structure information from x-ray diffraction or neutron scattering experiments, although fitting to other data such as elastic or dielectric constants is highly desirable. Whilst crystal structure data contains information about the location of minima on the energy surface many additional properties contain information about the curvature of the energy surface.

Typically the quality of reproduction is judged through a least sum of squares approach,

$$\sum_{i=1}^{N_{obs}} \omega_i (f_i^{obs} - f_i^{calc})^2 \tag{2.7}$$

in which f_i^{obs} and f_i^{calc} are the observed and calculated values of observables respec-

tively. These are weighted by a factor ω_i, depending on the relative importance and reliability of available data. This is summed over all observables N. A perfect reproduction will produce a zero sum of squares, with all properties perfectly matched. However, this is rarely achieved due to the complexity of simulations, approximations inherent to the model and the errors on experimental data.

It must be noted that interatomic potentials can be derived through *ab initio* calculations. Here, an energy surface is calculated from electronic structure methods and potential parameters are varied so as to reproduce the surface. However, a potential derived through this approach should still be tested against the extent to which it reproduces experimental data. Such an approach has not been applied in this work and hence is not discussed in detail.

2.1.3 Energy Minimisation

With an accurate description of the energy surface of the system in terms of atomic coordinates the process of energy minimisation is essential, to ensure the model is allowed to relax to a stable configuration. Conceptually this is quite simple: structural parameters, such as ion coordinate and cell dimensions, are adjusted until a minimum energy configuration is obtained. To ensure reduced computational expense for a large crystal structure, reasonably complex mathematical methods are typically employed in this operation. Energy minimisation techniques can in general be classified by the level of derivative information that is included. Zeroth order techniques are computationally cheap, and highly robust in that they rarely fail to locate a minima. However, except in trivial situations they tend to approach minima slowly, requiring many iterations, making the process unworkable for the systems explored in this work [154]. First order techniques introduce first derivative information, with a commensurate increase in the speed of convergence. Such techniques are also fairly robust, although the added expense of calculating and storing derivative information must be taken into account. Finally second order methods include second derivatives, introducing further information on the curvature of the energy surface. This can lead to step changes in the speed of convergence, although again the added computational expense of calculating

and storing second derivative information must be considered.

When considering multi-dimensional functions the gradient of a system of N constituents forms a vector $\mathbf{g}$ composed of $3N$ elements,

$$\mathbf{g} = U'(x) = \begin{bmatrix} \frac{\partial}{\partial x_1} U(x) \\ \vdots \\ \frac{\partial}{\partial x_{3N}} U(x) \end{bmatrix} \tag{2.8}$$

The direction and magnitude of the gradient contains information on the location of the minima, and the steepness of the function at the current point. Second derivative information is contained in the Hessian, or force constant matrix, a $3N \times 3N$ matrix of the form,

$$H = U''(x) = \begin{bmatrix} \frac{\partial^2 U}{\partial x_1^2} & \cdots & \frac{\partial^2 U}{\partial x_1 x_{3N}} \\ \vdots & \ddots & \vdots \\ \frac{\partial^2 U}{\partial x_{3N} x_1} & \cdots & \frac{\partial^2 U}{\partial x_{3N}^2} \end{bmatrix} \tag{2.9}$$

This holds information on the local curvature of the energy surface, which can be used in energy minimisation. At a stationary point the gradient vector, g, will be zero. Furthermore, at a minima the second derivative will be positive in all directions. Conversely, a saddle point is characterised by having one or more negative elements. For energy minimisation techniques which include derivative information, the energy function is generally expressed as a Taylor function about a position on the energy surface $\mathbf{x_i}$,

$$U(\mathbf{x}) = U(\mathbf{x_i}) + (\mathbf{x} - \mathbf{x_i})^T \mathbf{g}(\mathbf{x_i}) + \frac{(\mathbf{x} - \mathbf{x_i})^T H(\mathbf{x_i})(\mathbf{x} - \mathbf{x_i})}{2} + ... \tag{2.10}$$

where $\mathbf{g}$ and H are the gradient vector and Hessian matrix respectively. The series is truncated at the Hessian term and as such assumes the energy surface is quadratic. This approximation holds well close to a minima but is less valid for locations further

from the minima. As such, derivative methods are best applied close to a minimum.

First Derivative Methods

The simplest first derivative method is the **Steepest Descent** algorithm which quickly locates lower points on the energy surface by altering the atomic positions along the line of steepest descent. The direction of steepest descent can be represented by a vector, $\mathbf{r}$, which directly opposes the gradient vector such that,

$$\mathbf{r_i} = -\mathbf{g_i} \tag{2.11}$$

Given the steepest descent vector, $\mathbf{r_i}$, the atomic coordinates are updated, in an attempt to minimise the energy function, through the iteration

$$\mathbf{x_{i+1}} = \mathbf{x_i} + \alpha_i \mathbf{r_i} \tag{2.12}$$

whereby the scalar α_i governs how far along $\mathbf{r_i}$ to move to reach the minima. A line search or arbitrary step approach is taken, and after an initial value is taken α_i is updated during the search. If the direction of $\mathbf{r_i}$ remains constant over subsequent steps the minimia is assumed not to have been reached, and α_i is scaled by a factor (typically 1.2). If the direction of $\mathbf{r_i}$ is reversed then it is assumed the minima has been overshot and α_i is scaled by another factor (typically 0.5).

Once the minimum in the direction of the line search has been reached there can be no component of $\mathbf{g_{i+1}}$ along $\mathbf{r_i}$, by definition. Therefore, $\mathbf{r_{i+1}}$ must be orthogonal to $\mathbf{r_i}$ and the steepest descent algorithm must approach minima through a series of orthogonal vectors, as demonstrated in Figure 2-3(a). This process is very robust far from a minima, where the harmonic approximation is less valid, and the direction of movement $\mathbf{r_i}$ is determined by the largest inter-atomic forces, so will quickly relax high energy configurations. However, due to the alternating orthogonal direction vectors the minima is only approached indirectly and is highly dependent on the starting location and minima type. This is particularly troublesome for long narrow valleys, where

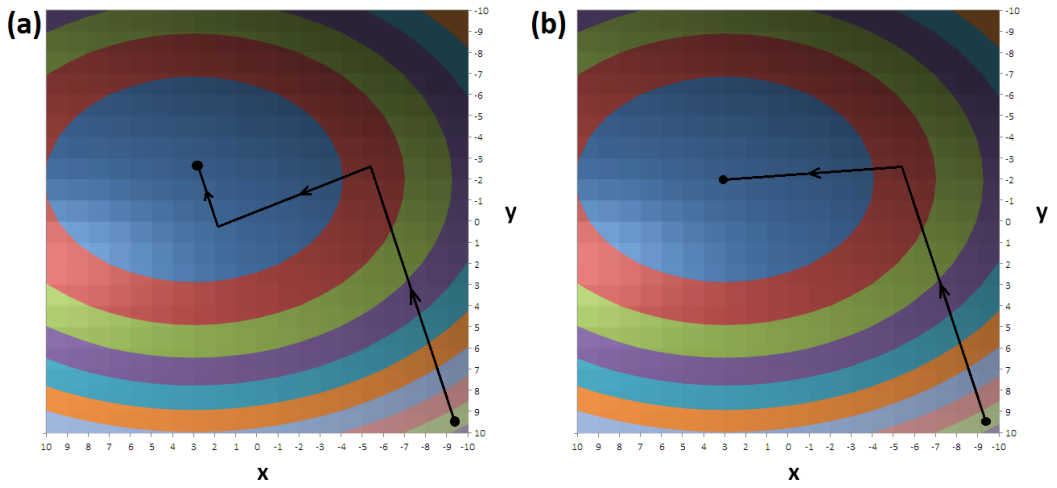

Figure 2-3: *Representation of first derivative minmisation algorithms, (a) the steepest gradient method in which the minima is approached through a series of orthogonal steps and (b) the conjugate gradient approach with the first step identical to steepest descent but subsequent steps are more efficient.*

many small steps will be required to reach a minimum if the starting configuration is unfavourable.

The **Conjugate Gradient** algorithm is more efficient, taking fewer steps to reach a minima. Fundamentally a set of orthogonal search vectors $\mathbf{d_0}$,$\mathbf{d_1}$, . . . , $\mathbf{d_{n-1}}$ (for a function of n variables) is chosen, and the energy is minimsed along each one only once. In this algorithm a new search vector, $\mathbf{d_i}$, is generated from the previous gradient, $\mathbf{g_{i-1}}$, previous search vector, $\mathbf{d_{i-1}}$, and current gradient, $\mathbf{g_i}$, according to the relation

$$\mathbf{d_i} = -\mathbf{g_i} + \beta_i \mathbf{d_{i-1}} \tag{2.13}$$

where β_i is defined as

$$\beta_i = \frac{\mathbf{g_i} \cdot \mathbf{g_i}}{\mathbf{g_{i-1}} \cdot \mathbf{g_{i-1}}} \tag{2.14}$$

As with the steepest descent algorithm a new position is then generated along a set direction, through equation 2.12 with $\mathbf{r_i}$ replaced by $\mathbf{d_i}$. Since previous iteration information is required for this technique, the initial search direction is taken along the steepest decent vector, $\mathbf{r_i}$, just as in the steepest descent algorithm. This method is

illustrated in Figure 2-3(b).

Second Derivative Methods

The **Newton-Raphson** method includes second order, along with first order derivatives. The technique is based upon approximating the energy surface with a Taylor series, expanded about the point $\mathbf{x_i}$ as given by,

$$U(\mathbf{x}) = U(\mathbf{x_i}) + (\mathbf{x} - \mathbf{x_i})^T \mathbf{g}(\mathbf{x_i}) + \frac{(\mathbf{x} - \mathbf{x_i})^T H(\mathbf{x_i})(\mathbf{x} - \mathbf{x_i})}{2} \tag{2.15}$$

From which the first derivative of $U(\mathbf{x})$ is given by

$$U'(\mathbf{x}) = \mathbf{g_i} + (\mathbf{x} - \mathbf{x_i})H_i \tag{2.16}$$

By definition at the minimum ($\mathbf{x}$=$\mathbf{x_m}$) the gradient will be zero, leading to the relation

$$\mathbf{x_m} = \mathbf{x_i} - H_i^{-1}\mathbf{g_i} \tag{2.17}$$

Hence for a truly quadratic surface the minimum will be reached in a single step. In real systems, which are rarely quadratic, a point closer to the minimum is generated and an iterative process is employed, updated through the relation

$$\mathbf{x_{i+1}} = \mathbf{x_i} + H_i^{-1}\mathbf{g_i} \tag{2.18}$$

Near a minima, where the harmonic approximation is most valid, the Newton-Raphson process provides rapid convergence. This becomes less true further from the minimum, where optimisation can become unstable. Therefore it is important to begin optimisations from a good starting structure. Typically this is achieved through the use of experimental data. Where this is not possible a different minimsation technique can be used initially, with Newton-Raphson procedures adopted as a minima is approached.

The advantages in convergence speed can be dwarfed by the computational expense required in calculation and inversion of the Hessian matrix. In response, it is possible to exploit the fact that the Hessian will not change much with each iteration, meaning the Hessian can be updated at each step rather than completely recalculated. Accordingly the BFGS updating formula is used on most iterations, with full recalculation of the Hessian matrix only after the energy has changed significantly or a set number of iterations. The BFGS formula updates the Hessian by

$$H_{i+1} \sim H_i + \frac{(\mathbf{x_{i+1}} - \mathbf{x_i}) \times (\mathbf{x_{i+1}} - \mathbf{x_i})}{(\mathbf{x_{i+1}} - \mathbf{x_i}).(\mathbf{g_{i+1}} - \mathbf{g_i})} - \frac{[H_i.(\mathbf{g_{i+1}} - \mathbf{g_i})] \times [H_i.(\mathbf{g_{i+1}} - \mathbf{g_i})]}{(\mathbf{g_{i+1}} - \mathbf{g_i}.H_i.(\mathbf{g_{i+1}} - \mathbf{g_i})} + [(\mathbf{g_{i+1}} - \mathbf{g_i}).H_i.(\mathbf{g_{i+1}} - \mathbf{g_i}]u \times u \tag{2.19}$$

where

$$u = \frac{(\mathbf{x_{i+1}} - \mathbf{x_i})}{(\mathbf{x_{i+1}} - \mathbf{x_i}.(\mathbf{g_{i+1}} - \mathbf{g_i})} - \frac{[H_i \cdot (\mathbf{g_{i+1}} - \mathbf{g_i})]}{\mathbf{g_{+1}} - \mathbf{g_i}).H_i.(\mathbf{g_{i+1}} - \mathbf{g_i})} \tag{2.20}$$

Whilst this approximation holds, the estimated Hessian matrix approaches the true Hessian over increasing iterations. In this manner the Newton-Raphson method can provide fairly rapid convergence.

2.1.4 Periodic Boundary Conditions and Ewald Summation

When dealing with solid state systems it is necessary to transform the conceptually infinite lattice to some reduced representation to allow simulations to be performed. This is often achieved through the use of periodic boundary conditions, the specification of which can greatly reduce computational expense. Through the application of symmetry operations a crystalline material can be expressed as a unit cell, containing a relatively small number of ions, which repeats infinitely in all three dimensions. This is demonstrated in Figure 2-4. In this representation, during a simulation the unit cell is surrounded by identical repeating images of itself. These images influence the original unit cell, that is ions in the cell at $x = 0$ to $x = a$ will interact with the ions in the

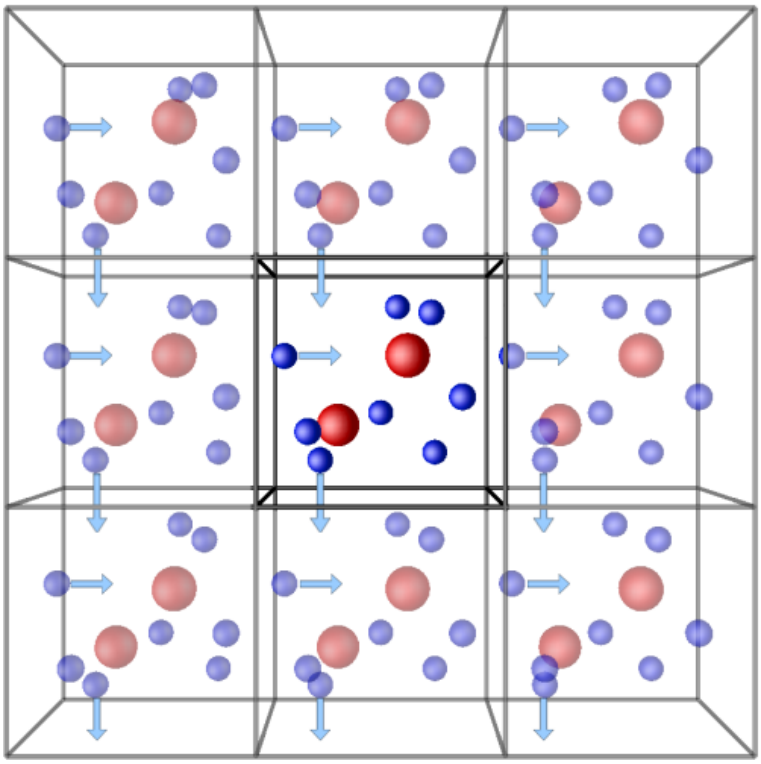

Figure 2-4: *Example of periodic boundary conditions [155].*

ions in its image at $x = -a$ to $x = 0$ where a is the unit cell vector along x. However, the ions within images only interact with the primary unit cell itself. In this manner periodic boundary conditions allow the unit cell to respond as if in an extended solid state system.

There are two important situations which must be treated with care in periodic boundary conditions. Firstly, simulations which break the long range symmetry of the unit cell must be treated extremely carefully. This typically includes simulations such as isolated defect calculations, wherein a lone defect is to be explored. To avoid the defect interacting with its own image a sufficiently large unit cell must used. Alternatively a Mott-Littleton type approach may be used, as employed in this work and discussed in **Section 2.2**. Secondly, it is important to correctly treat ions which migrate out of the initial unit cell during the simulation and into a neighbouring image. Generally this is done by introducing the ion into the unit cell at the coordinate it would have entered the image cell. This is particularly sensitive in molecular dynamics simulations and in the calculation of properties such as mean square displacements or the radial

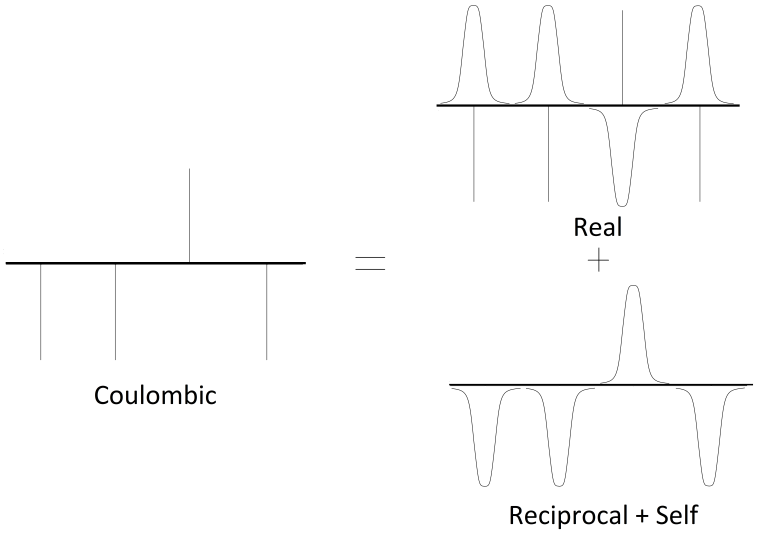

Figure 2-5: *A graphical example of an Ewald summation.The sum of a series of point charges (Coulombic) can be calculated from a series of screened charges (Real), combined with compensating charges to account for the screening (Reciprocal + Self).*

distribution function.

Furthermore the evaluation of the Coulomb energy is problematic for periodic systems as it is only conditionally convergent, meaning it is ill defined for infinitely extending 3-D materials. This is because although the interaction between ions decays as r^{-1}, the number of interacting ions increases as $4\pi r^2$ (i.e. the surface of a sphere). As such, rather than decaying with distance the interaction energy density increases. This problem is overcome through a technique proposed by Ewald, whereupon charge neutrality and zero dipole moment conditions are imposed on the system. The poor distance convergence of the resulting system is improved upon with a Laplace transformation and separation into two series. One is rapidly convergent in real space, the other in reciprocal space. This transformation is displayed graphically in Figure 2-5. Conceptually, the real space series is generated by masking the ionic charges with a series of opposing charges, with Gaussian distributions. The total charge on the Gaussian matches the ionic charge, and the interaction felt by neighbouring ions is equivalent to the fraction of the ionic charge, which has not effectively been screened. Therefore this rapidly converges to zero at increasing ionic separations, and can be evaluated in real space. The reciprocal series is composed of a counteracting set of Gaussian charges, such that summation of the two series in effect removes the Gaussian charge,

leaving just the ionic interaction. The compensating charge series forms a smooth periodic function in real space, which is amenable to description by a rapidly converging Fourier series in reciprocal space. Finally, the interaction between a point charge and its surrounding screening charge must be accounted for through a self interaction term. The added computational effort in performing the Ewald transformation is more than compensated for by the resultant speed up in convergence.

2.2 Point Defect Simulation

When considering solid state crystalline materials, it is often convenient to consider the solid as an infinitely extending perfectly repeating lattice as the basis for investigation. However, this concept is a fallacy, the perfect crystal does not exist for any real solid; instead the lattice will be populated with myriad departures from perfect repetition. These departures are a prerequisite of the third law of thermodynamics and are known as *defects*, with a significant influence on many properties of a system. Indeed, often to study a materials properties is to study its defects. Ionic conductivity for example is a material property largely driven by the existence of defects. Therefore, consideration of defects is vital to understanding the mechanisms that cause many properties to arise. It is point defects, changes at an atomistic level, which are of greatest interest in the study of the fundamental limits on conductivity of solid state materials, and as such they are discussed below [156].

There are three types of point defect observed to exist in real solids. Firstly, **vacancies** are composed of an absence of an ion from the crystal lattice at a point it would be expected to occupy. Secondly, **interstitials** are formed when ions occupy non-lattice points in the crystal, fitting into space between the main atoms of the crystalline array. The final form of fundamental defects, **impurities**, involve either the replacement of a lattice ion by a non-stoichiometric species (substitutional impurities) or the insertion of a new species at an interstitial site (interstitial impurity). All three types of defect are displayed in Figure 2-6. Much of the influence of defects comes from the relaxation of the crystal structure about the defect, a result of the crystal responding to the perturbation introduced into the potential landscape.

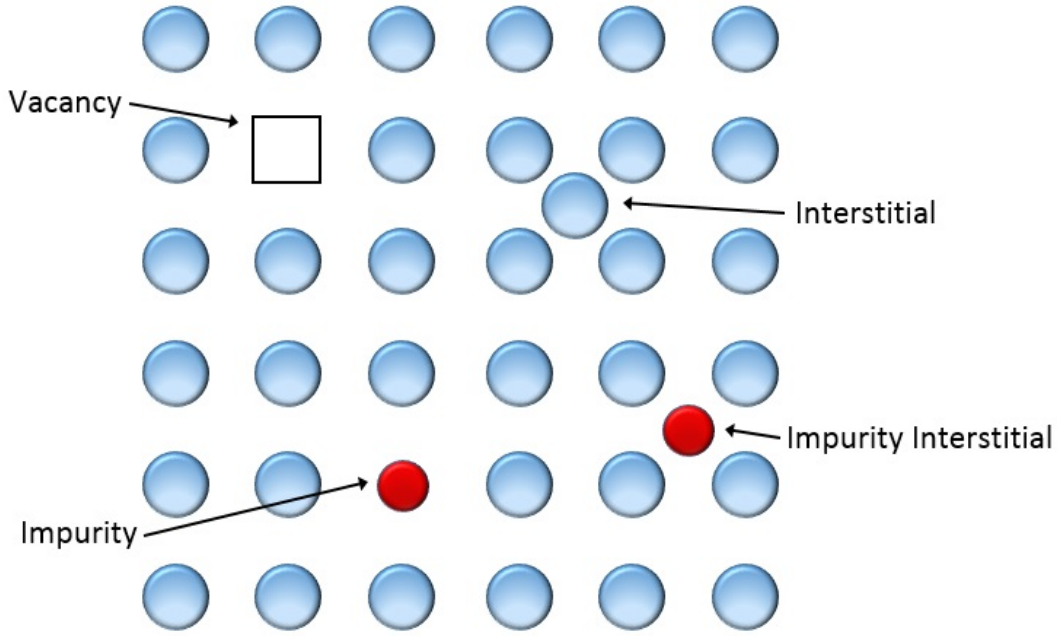

Figure 2-6: *Diagram showing point defects in crystals including vacancies, interstitials and impurities.*

Point defects are never found as a single isolated species in an otherwise perfect lattice, as they introduce a net charge to the crystal. For instance, an O^{2-} vacancy will introduce an effective +2 charge to the system. As such, to maintain charge neutrality point defects occur in specific groupings. There are two main groupings of intrinsic defects in ionic crystals, *Schottky* or *Frenkel*. Cation vacancies can be balanced by anion vacancies, forming *Schottky* defects. Alternatively, interstitials can be balanced by vacancies of the corresponding ion as is found in *Frenkel* defects. In addition, impurity defects such as aliovalent impurities, are balanced by either a vacancy, interstitial or another impurity compensation mechanism. Finally the double-impurity *antisite* defect, whereupon a cation and anion switch lattice sites, is commonly observed in solids [156]. Many properties of solids rely on the density and stability of these four defect types, and a thorough understanding of their influence on crystal structure is vital to grasping the fundamental processes occurring in the materials [156]. Defects are often described using Kroger-Vink nomenclature and this is the standard adopted in later chapters of this work. For an explanation of the notation see **Appendix A**. When simulating such systems it is necessary to include the effect of relaxation of the lattice around the point defect. It is also necessary to extend this relaxation over a large vol-

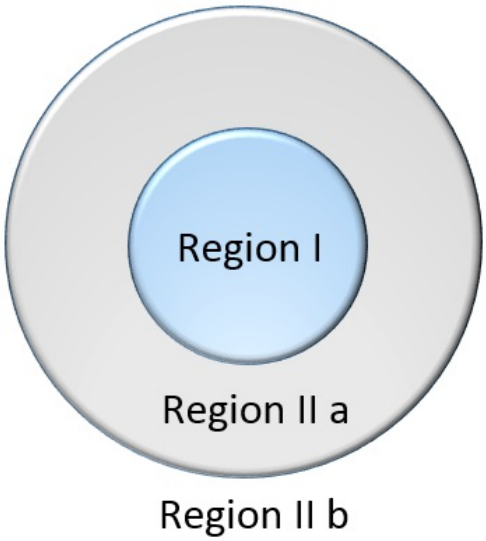

Figure 2-7: *Diagram of the three part relaxation structure employed in defect calculation.*

ume of the crystal, as the charged nature of defect provides an extensive perturbation of the surrounding lattice.

To model such perturbations a three region simulation is typically employed, as demonstrated in Figure 2-7. The crystal lattice surrounding the defect is divided into two primary regions (regions I and II), with the outermost region further subdivided into two secondary regions (regions IIa and IIb). The innermost primary region, usually composed of around 1000 ions, is simulated atomistically (i.e. explicitly using the full potential model). All coordinates are adjusted independently, subject to the full interatomic potential described above. This highly demanding process is required for the innermost region as the forces exerted by the defects lead to significant displacements in the surrounding ions. In the outermost region the forces exerted by the defect are somewhat diminished and, rather than full potentials based simulation, quasi-continuum methods can be employed through the *Mott-Littleton* approximation.

Within the region IIa the ions are treated as if trapped in a harmonic well, with corresponding quadratic energy function of the form

$$E_2(\gamma) = \frac{1}{2}\gamma^T B\gamma \tag{2.21}$$

whereby γ is the displacement from equilibrium of the ions in region IIa and B is a force constant matrix. The model is only valid for small perturbations from equilibrium positions, hence it is not applicable to ions in region I where the perturbations may potentially be large. It also introduces the requirement to calculate the equilibrium position of ions in region IIa before the defect is introduced (i.e. in the perfect lattice), although the computational time saved from the approximation greatly outweighs this burden. The ions in region IIa are still treated separately, with the perturbations being calculated on a per ion basis. In region IIb the response to the defect is assumed to be primarily dielectric in nature and the implicit polarization of sublattices is considered, rather than individual ion responses, to save computational expense.

Upon division of the system into the two primary regions the total energy of the system is given by

$$E = E_1(x) + E_{12}(x, \gamma) + E_2(\gamma) \tag{2.22}$$

including the energy of region I, E_1, the energy of region II, E_2, and the energy arising from the interaction between the two regions, E_{12}, as functions of the region I ion coordinates, x, and the region II ion coordinates , γ. Imposing the condition that the displacement of ions in region II must reach an equilibrium the explicit dependence on E_2 can be removed through the relation

$$E_2 = -\frac{1}{2}\gamma^T \frac{\partial E_{12}}{\partial \gamma} \tag{2.23}$$

leading to a significant reduction in computational expenditure.

Within the framework described above the calculation proceeds as follows:

1) Energy minimisation is performed on the perfect crystal lattice structure

2) The defect is introduced and energy minimisation performed on region I atomistically, determining the equilibrium values of x.

3) The displacements of individual ions are calculated for region IIa using the Mott-

Littleton approximation and the sum of all the charged defects in region I.

4) The value of $E_1(x)$ is calculated explicitly.

5) $E_{12}(x, \gamma)$ is calculated explicitly for region IIa, along with its derivative.

6) The displacements in region IIb are calculated for the crystal responding to the net charges on defects.

The greatest computational time is devoted to the energy minimisation of region I. As such, the size of region I must be chosen with care: large enough for the energy to converge to the required degree of accuracy, whilst not so large as to require unfeasible computational time. Assuming region I is sufficiently large the calculations are now known to be exact, within the assumptions and constraints implicit in the potential model employed.

2.2.1 Ion Migration Simulations

The migration of ions through materials is of utmost importance to many applications, including batteries. Several common migration mechanisms exist, such as vacancy hopping, direct interstitial migration and the intersticialcy mechanism. The two most typically observed in battery materials are vacancy hopping and interstitial migration, both of which are shown schematically in Figure 2-8. The direct interstitial-type mechanism is the most simple, in that an ion occupying an interstitial site simply transitions to another neighbouring interstitial site. Alternatively, in the vacancy hopping mechanism a lattice ion migrates from one site to a neighbouring lattice vacancy. Over repeated steps the vacancy migrates through the lattice, with net ion migration in the opposing direction.

Simulation of ion migration is achieved by producing a series of snapshots along the migration step, which are then combined to reproduce the energy profile of migration. This allows elucidation of the migration mechanism, path and activation energy, along with how the lattice itself responds during a single migration step. This is typically performed through either a nudged elastic band (NEB) or constrained minimisation

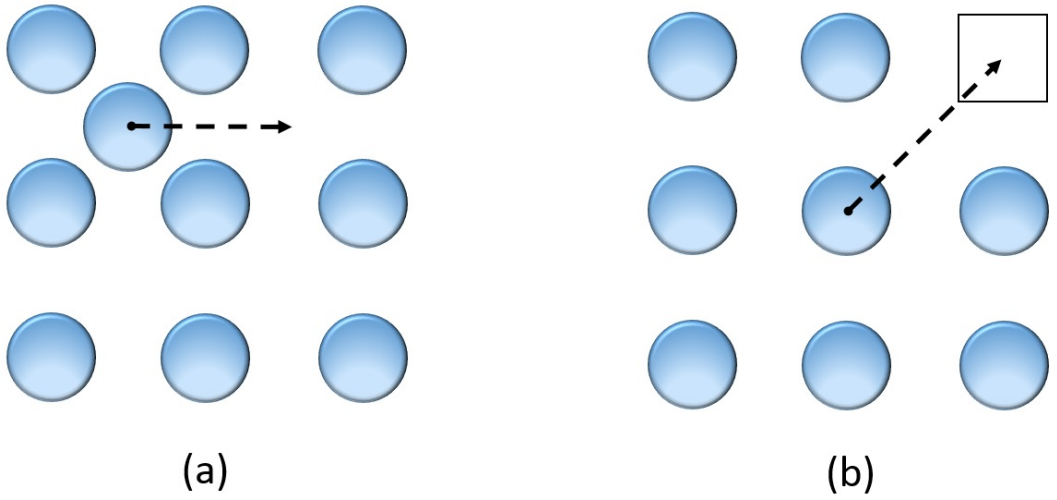

Figure 2-8: *Illustration of two common solid state ion diffusion mechanisms, including (a) interstitial migration and (b) vacancy hopping.*

technique, with the latter employed in this study.

In constrained minimisation a series of structures are generated, with the migrating ion located in an incremental series between two crystallographic sites. The motion of the ion is then constrained in one direction, preferably as close to the migration direction as possible, and energy minimisation performed, allowing the ion to relax in the directions orthogonal to the constraint direction. The resulting configurations and energies then allow mapping of the energy profile and migration path of the transition. To adequately map the curvature of the transition each increment should be small, typically no greater than 0.2 Å, otherwise the saddle point may be missed. Secondly, it is important to ensure each relaxed snapshot can be combined to produce a continuous path for the migrating ion. Although user intensive in terms of generating and interpreting the constrained series, the process is particularly robust for exploring ion migration.

2.3 Molecular Dynamics

A significant disadvantage of the atomistic methods described above is the failure to include the effects of kinetic energy, or explicitly detail dynamical information of the system. Calculations are performed at 0 K and as such are entirely based on potential energy, thermal effects are completely neglected.

Molecular dynamics (MD) overcomes these limitations by including the effects of temperature, and therefore kinetic energy, through randomly assigning particles a velocity as governed by statistical distributions. These distributions are chosen such that a desired system temperature is generated. The kinetic energy thus introduced allows particles to overcome energy barriers, exploring more of the energy surface. Given the limits placed on overall simulation time (typically ∼ns) by computational expense particles can typically overcome small energy barriers of the order of a few k_BT. This is particularly useful in studying diffusion processes, time averaged structure issues and dynamical properties. The basis of these MD techniques is discussed in the following section, although more extensive descriptions can be found elsewhere [145, 157].

In order to simulate dynamic crystal phenomena, ion position and velocities must be described as a function of time. This is achieved through integration of Newton's laws of motion over discrete time periods, for all particles in the system. This requires knowledge of the force ($\mathbf{f}$) acting on an atom (mass m), thereby allowing the determination of how acceleration ($\mathbf{a}$), velocity ($\mathbf{v}$) and position ($\mathbf{r}$) vary with time, as given by,

$$\mathbf{f} = \frac{d\mathbf{p}}{dt} = m\mathbf{a} = m\frac{d^2\mathbf{r}}{dt^2} \tag{2.24}$$

If the force acting on an ion were constant as a function of time and position,then all the requisite information could be calculated from

$$\mathbf{v_{t+dt}} = \mathbf{v_t} + \mathbf{a_t}dt \tag{2.25}$$

$$\mathbf{r_{t+dt}} = \mathbf{r_t} + \mathbf{v_t}dt + \frac{1}{2}\mathbf{a_t}dt \tag{2.26}$$

Unfortunately in real systems the force acting on an ion is a function of the proximity of other ions, itself a function of time and ion position. As such, the above equations are only valid for infinitesimal time steps, and overall system evolution become a coupled many-body problem. Describing the motion of ions over larger time scales requires numerical integration techniques.

2.3.1 Integration techniques: Verlet and Verlet-Leapfrog

In order to update the ion positions and velocities through numerical integration the simulation is broken down into a series of discrete time steps, separated by a finite time Δt, over which Newton's laws are applied. The forces acting on an ion at time t are calculated from the complete set of ion positions within the system. This can then be used to update the acceleration, and hence velocity and position, of the ion at time $t + \Delta t$. Within this lies the (incorrect) assumption that the forces acting on the ions remain constant over the time step Δt, a significant source of error in this technique.

The integration algorithm used in this work is based upon the Verlet algorithm. To begin with it is assumed that the position, velocity and acceleration of ions can be approximated by a Taylor series. Typically this is truncated at the third derivative term. The accuracy of simulations can be improved by including higher order terms, or by reducing the time step. The updated ion positions can be thus be derived from the current ion positions, $\mathbf{r_t}$, through the formula

$$\mathbf{r_{r+\Delta t}} = \mathbf{r_t} + \mathbf{v_t}\Delta t + \frac{\mathbf{a_t}}{2}\Delta t^2 + \frac{\mathbf{b_t}}{6}\Delta t^3 + \Theta(\Delta t^4) \tag{2.27}$$

where $\mathbf{v_t}$, $\mathbf{a_t}$ and $\mathbf{b_t}$ are the velocity, acceleration and jerk at time t respectively, whilst Θ is an error term. The velocity, acceleration and jerk are simply the first, second and third derivatives of position with respect to time. The third derivative, jerk, essentially represents the change in force with respect to time and is somewhat difficult to compute directly. To overcome this Verlet employed a method whereby information from the previous time step, $t-\Delta t$ can be used to include third derivative information implicitly. As above the Taylor series for time step $t - \Delta t$ can be derived

$$\mathbf{r_{r-\Delta t}} = \mathbf{r_t} - \mathbf{v_t}\Delta t + \frac{\mathbf{a_t}}{2}\Delta t^2 - \frac{\mathbf{b_t}}{6}\Delta t^3 + \Theta(\Delta t^4) \tag{2.28}$$

this can then be summed with the equation for time step $t + \Delta t$ to give

$$\mathbf{r_{r+\Delta t}} = 2\mathbf{r_t} - \mathbf{r_{t-\Delta t}} + \mathbf{a_t}\Delta t^2 + \Theta(\Delta t^4) \tag{2.29}$$

Therefore, by deploying information from two time steps the requirement to calculate the third derivative has been eliminated. However, the error term is increased since the errors from calculation of both $\mathbf{r_{t-\Delta t}}$ and $\mathbf{r_t}$ are carried into $\mathbf{r_{t+\Delta t}}$. From equation 2.29 it can be seen that the Verlet algorithm does not require explicit calculation of ion velocities in order to compute positions. However, in order to calculate total system energy the kinetic energy, and hence velocities, are required. In addition, maintaining system temperature requires velocity information as discussed below. Subtraction of $\mathbf{r_{t+\Delta t}}$ from $\mathbf{r_{t-\Delta t}}$ allows calculation of velocities

$$\mathbf{v_t} = \frac{\mathbf{r_{t+\Delta t}} - \mathbf{r_{t-\Delta t}}}{2\Delta t} + \Theta(\Delta t^2) \tag{2.30}$$

Therefore, in this scheme ion velocities cannot be calculated until the subsequent ion positions are found. In addition the error term is large, of the order Δt^2.

In an attempt to avoid these issues the Verlet-leapfrog variant algorithm can be deployed. Within Verlet-leapfrog the velocities are determined at half time steps, and the ion position are updated by a somewhat modified formula,

$$\mathbf{v_{t-\frac{1}{2}\Delta t}} = \frac{\mathbf{r_t} - \mathbf{r_{t-\Delta t}}}{\Delta t} \tag{2.31}$$

$$\mathbf{v_{t+\frac{1}{2}\Delta t}} = \frac{\mathbf{r_{t+\Delta t}} - \mathbf{r_t}}{\Delta t} \tag{2.32}$$

$$\mathbf{v_{t+\frac{1}{2}\Delta t}} = \mathbf{v_{t-\frac{1}{2}\Delta t}} + \mathbf{a_t}\Delta t + \Theta(\Delta t^3) \tag{2.33}$$

$$\mathbf{r_{t+\Delta t}} = \mathbf{r_t} + \mathbf{v_{t+\frac{1}{2}\Delta t}}\Delta t + \Theta(\Delta t^4) \tag{2.34}$$

During simulations the accelerations are evaluated from the forces at the current time step and used to update the velocities at $t - \frac{1}{2}\Delta t$ to those at $t + \frac{1}{2}\Delta t$. As such, the velocities operate in half time steps of the positions and in essence leapfrog over the positions at time t, which then leapfrog over the velocities at time $t + \frac{1}{2}\Delta t$. By including the velocities explicitly the accuracy to which they are calculated is an order of magnitude greater. However, since the velocities and positions are not synchronised the potential and kinetic energies cannot be calculated accurately at the same time.

The full step velocities can be taken from the average of two half step velocities from

$$\mathbf{v_t} = \frac{1}{2}(\mathbf{v_{t+\frac{1}{2}\Delta t}} + \mathbf{v_{t-\frac{1}{2}\Delta t}}) + \Theta(\Delta t^2) \tag{2.35}$$

However, this carries the error of both half step velocities through and as such is less accurate than Verlet alone when calculating $\mathbf{v_t}$.

It is important to note that these algorithms are not self starting, both require information from a previous step. As such, initial velocities are randomly assigned so as to bring the system to the desired initial temperature whilst setting total translational momentum to zero. This is expressed mathematically by,

$$\sum_{i=1}^{N} m_i \mathbf{v_i}^2 = 3Nk_BT \tag{2.36}$$

$$\sum_{i=1}^{N} m_i \mathbf{v_i} = 0 \tag{2.37}$$

where N is the total number of atoms and k_B is the Boltzmann constant.

2.3.2 Time Step, Ensembles and Equilibration

The choice of the size of time step is critical and non-trivial. Within the verlet-leapfrog algorithm the time step must also be small enough such that the ion positions and velocities (separated by $\frac{1}{2}\Delta t$) remain consistent. Additionally, the time step must be chosen such that it is not so large so as to introduce instabilities into the system, causing ions to possess unphysical energies or move unphysical distances. However, too small a time step will significantly increase computational expense and prohibit the simulation from exploring many of the available states. Therefore, the ideal choice should allow the greatest amount of simulation time, without introducing instabilities or significant errors. In practice this is typically between 0.1 and 2 femtoseconds. It is important to note that the use of the shell model of polarizability is especially sensitive to the size of time step, often requiring steps of no more than 0.1 femtoseconds. This is necessary to accurately model the motion of the nearly massless shell, describing

electron motion which is known to be rapid. To go to longer time steps a rigid ion model is often applied.

Another important aspect of molecular dynamics simulations is the influence of ensembles. An ensemble is a distribution of accessible states of a system, subject to a series of constraints. In MD simulations the states correspond to different arrangements of the ionic coordinates, which will vary with respect to time. Different ensembles relate to different sets of constraints, allowing one to impose various conditions. A common ensemble is the microcanonical ensemble (NVE) wherein the number of particles N, simulation cell volume V and total system energy E are held constant. That is, although the potential and kinetic energies can vary the total energy (or Hamiltonian H) remains constant. However, the microcanonical ensemble does not correspond strongly with real systems, as large temperature and pressure fluctuations are allowed. In order to study systems as a function of temperature or pressure the canonical (NVT) and isobaric-isothermal (NPT) ensembles can be used, although such ensembles require the ability to control both the temperature and pressure of the simulated system. This can be achieved using mathematical thermostats and barostats. An additional benefit of deploying such controls is that they assist in compensating for the accumulation of rounding errors compounded over multiple time steps.

The kinetic energy of the system can be related to the velocities and temperature of the system through the Boltzmann relation,

$$E = \frac{1}{2}\sum_{i=1}^{N} m_i {\mathbf{v_i}}^2 = \frac{3}{2} N k_B T \tag{2.38}$$

Therefore, one way to control temperature is to scale the velocities precisely at each control period. However, this technique prevents any fluctuations in temperature, which is unphysical when simulating real systems. A more realistic thermostat developed by Berendson et al. is comprised of a coupled mathematical heat sink kept at the desired temperature. The velocities are scaled at each control step, with the rate of change of temperature proportional to the difference between the heat sink and the simulation cell, given by

$$\frac{dT(t)}{dt} = \frac{1}{\tau}(T_{bath} - T(t)) \tag{2.39}$$

where τ is a simulation parameter which dictates how strongly the system is coupled to the external heat sink, and has a significant impact on the evolution of the simulation. The degree of coupling between the heat sink and the system is inversely proportional to the value of τ. If too small a value is chosen the coupling becomes too strong and unrealistically small temperature variations are observed. If τ is too large the coupling becomes too weak and the thermostat is effectively removed, leading the simulation to approach *NVE* conditions. Typical values for τ are roughly 2 orders of magnitude greater than the time step, leading to values around 100 femto-seconds. The Berendson thermostat approach can easily be modified for use as a barostat, scaling system pressure rather than temperature. The system is this time connected to a hypothetical pressure sink and updated as above by,

$$\frac{dP(t)}{dt} = \frac{1}{\tau}(P_{bath} - P(t)) \tag{2.40}$$

where τ is again the coupling parameter between the system and external pressure sink. The positions of the atoms are simply scaled, thereby compressing or expanding the system, depending on the pressure difference.

A final pseudo-parameter which must be considered in MD simulations is equilibration time. MD simulations commence with an equilibration period, during which the starting configuration with assigned velocities and ion positions is brought to a steady state. The most important property monitored during this process is the total energy (the sum of potential and kinetic energies) which is allowed to converge to a constant value. The actual length of simulation time required for equilibration is highly system and property specific, and must be judged on a simulation by simulation basis. However, equilibration often requires tens of thousands of time steps to allow the requisite properties to converge to stable configurations.

2.3.3 MD: Properties of Interest

Molecular dynamics can be used to investigate a vast number of solid state properties and the full range is beyond the scope of this discussion. However, several properties of interest are detailed below.

Mean Square Displacements

A particularly useful piece of information, which can be gleaned from MD simulations, is that of diffusion rates and energy barriers which can be derived from a mean square displacement (MSD) analysis. Mathematically the MSD is defined as

$$MSD(t) = \frac{1}{N}\Sigma|r_i(t) - r_i(0)|^2 \tag{2.41}$$

where N is the number of atoms, $r_i(0)$ is the initial ion positions and $r_i(t)$ is the current ion position. As such, the mean squared displacement (MSD) is a measure of the distance ions in the simulation have moved from their initial coordinates as a function of time. Considered over long time scales the MSD approaches a linear relation with respect to time, t, and is related to the self-diffusion coefficient D by the Einstein relation

$$MSD(t) = 2dDt \tag{2.42}$$

where d is the dimensionality of the system. As such, for a three dimensional system the diffusion coefficient is given by

$$D = \frac{1}{6}\lim_{t\to\infty}\frac{d}{dt}MSD \tag{2.43}$$

This provides a method for directly calculating the diffusion constant from the simulation. Furthermore, by obtaining MSD plots over several simulation temperatures the

activation energy for diffusion can be determined from the Arrhenius relation,

$$lnD = \frac{-E_a}{RT} + lnA \tag{2.44}$$

where R is the gas constant and E_a is the activation energy. The gradient of a plot of $ln(D)$ vs $\frac{1}{T}$ is equal to $\frac{-E_a}{R}$, allowing calculation of E_a, thereby taking statistical average information and deriving a single ion property. This can provide a complementary method, alongside static lattice energy minimization, for probing ion diffusion energetics.

Time Averaged Atomic Densities

When studying ion migration in crystalline materials it is important to be able to visualise the topological features of the migration, to discern the nature and mechanics of diffusion. A useful method for visualizing migration pathways is a time-averaged atomic density plot. This can be generated directly from trajectory data and used to view diffusion pathways. At a minimum the trajectory data must include the ion positions for a series of time steps, thereby detailing which locations ons have traversed over the course of the simulation. Producing time averaged atomic density plots can be approached by splitting the cell into a grid of three dimensional boxes, in which the positions of a particular ionic species at each time step can be superimposed and recorded. The number of ions in each box is then summed and normalised over the whole system. The result is a density plot detailing all of the grid spaces the ionic species has occupied during the simulation. The output of this technique is similar to neutron diffraction maximum entropy methods produced by experiment, detailing the diffusion pathways of ions in solids.

2.4 Density Functional Theory

Whilst empirical potential methods are based upon reproducing observed properties of real systems, *ab initio* techniques attempt to develop models directly from theoretical

considerations. There are two primary methods for exploring systems from *ab initio* considerations: *Hartree-Fock* and *Density Functional Theory (DFT)*. The Hartree-Fock method involves determination of the wavefunction of a many body system by approximating the N-body wavefunction with a single Slater determinant. In this way a set of N coupled equations for the N spin orbitals can be derived and solved in a self-consistent approach [158]. Although the Hartree-Fock method allows direct exploration of the wavefunction of a system, which DFT does not, over the last few decades DFT has become the most popular *ab initio* quantum mechanics technique for the study of solid state systems. This is largely due to the more modest computational expense of the DFT approach. Formulations and codes have now been developed to allow for the study of structure-property relationships of many-electron systems, and DFT is particularly favoured by condensed matter physicists and computational chemists. As such, the rest of this section deals with the theoretical underpinnings of DFT, although detailed discussions of the Hartree-Fock method can be found elsewhere.

The groundwork for DFT can be traced back to the 1920‘s and the work of Thomas and Fermi in developing a quantum mechanical model for the electronic structure of a many-body system, formulated in terms of the electronic density alone. This was then expanded upon by Dirac, who added a local density approximation for the electron exchange interaction [159]. Unfortunately, the substantial approximations involved in this work made it unsuitable for the calculation of the electronic structure of real systems, providing inaccurate or unreliable results. The major breakthrough in electronic structure prediction came in the 1960‘s through the development of the Hohenberg-Kohn Theorems and subsequently derived Kohn-Sham equations. This work provided the first practical framework for finding solutions to the Schroedinger equation for real systems and accurately predicting the electronic structure of many-electron systems. Indeed, Walter Kohn received the 1998 Nobel Prize in Chemistry for his contributions to the development of DFT. Since the 1960‘s much effort has been expended in improving upon the original work of Hohenberg, Kohn and Sham to make DFT into the hugely successful technique it is today. Many texts exist discussing DFT and its application to the solid state in detail [148–151], a brief overview of which is given below.

2.4.1 DFT Framework

The ultimate aim of all quantum mechanical techniques is to find a solution to the Schroedinger equation and hence determine the exact form for the wavefunction of the system. The simplest form of the time independent Schroedinger equation can be written in terms of the Hamiltonian, $\mathcal{H}$, total energy, $\mathcal{E}$ and wavefunction, ψ, as

$$\mathcal{H}\Psi = \mathcal{E}\Psi \tag{2.45}$$

All the information regarding the positions and spins of the particles within the system are contained within the many-body wavefunction. Therefore conceptually all material properties can be related back to the many-body wavefunction, knowledge of the wavefunction allows all material properties to be calculated. The eigenvalues of the full Hamiltonian operator correspond to the total energy of the system, so in principle simply knowing the correct form of the Hamiltonian would allow for the exact analytical solution to be derived. The full Hamiltonian can be described by (in atomic units):

$$\mathcal{H} = T_e + T_n + V_{int} + V_{nn} + V_{ext} \tag{2.46}$$

where T_e is the electronic kinetic energy, T_n is the nuclear kinetic energy and V_{int}, V_{nn} and V_{ext} refer to the three contributions to the potential energy. The potential resulting from electron-electron interaction is included in V_{int} whilst the electron-nuclei interaction potential is included in V_{ext}. Nuclear-nuclear repulsions are contained within the V_{nn} potential. These terms must be summed over all nuclei and electrons present in the system to provide a complete description. When done so explicitly this leads to:

$$\mathcal{H} = -\frac{h^2}{2m_e}\sum_i \nabla_i^2 - \sum_I \frac{h^2}{2M_I}\nabla_I^2 + \frac{1}{2}\sum_{i\neq j}\frac{e^2}{|r_i - r_j|} + \frac{1}{2}\sum_{I\neq J}\frac{Z_I Z_J . e^2}{|R_I - R_J|} - \sum_{i,I}\frac{Z_I . e}{|r_I - R_I} \tag{2.47}$$

Where the mass and position of nucleus I, of charge Z_I, are given by M_I and R_I respectively, the mass and position of the electron i is described by m_e and r_i respectively. It is clear from equation 2.47 that a formal evaluation of the Hamiltonian for a many-body system is an extremely complicated process, involving a large number of interdependent terms. So whilst the basic form of the time independent Schroedinger

equation is relatively simple, formulating a full analytical solution is exceptionally complex for anything other than trivial many-body systems. A full analytical evaluation of the Hamiltonian is beyond the capability of current computers and a series of approximations are required to make the problem tractable. Firstly, the Born-Oppenheimer approximation is employed to decouple the nuclear and electron motion. That is, due to the large difference in nuclear and electron mass and hence high speed of electron motion with respect to that of the nuclei, the electrons are assumed to move in a fixed nuclear arrangement. This allows the Hamiltonian to be rewritten in terms of the electronic Hamiltonian:

$$\mathcal{H}_{elec} = T + V_{int} + V_{ext} \tag{2.48}$$

$$\mathcal{H}_{elec} = -\frac{h^2}{2m_e}\sum_i \nabla_i^2 + \frac{1}{2}\sum_{i\neq j}\frac{e^2}{|r_i - r_j|} - \sum_{i,I}\frac{Z_I.e}{|r_I - R_I|} \tag{2.49}$$

$$\mathcal{H}_{elec} = -\frac{h^2}{2m_e}\sum_i \nabla_i^2 + \frac{1}{2}\sum_{i\neq j}\frac{e^2}{|r_i - r_j|} + \sum_i V_{ext}(r_i) \tag{2.50}$$

This removes many of the cross terms from the original Hamiltonian, thereby simplifying the problem significantly. The many-body wavefunction is now dependent only upon the electronic configuration of the system, with the nuclear configuration only evident as a component of the external potential (V_{ext}). However, solving this formulation is still beyond all but the simplest systems, primarily due to the large number of electron-electron interactions still present.

2.4.2 Hohenberg-Kohn Theorems

A viable framework for finding solutions to the many-body Schroedinger equation was provided by Hohenberg and Kohn. The validity of their approach was formalised and proven in 1964 with the publication of the Hohenberg-Kohn Theorems [160]. These two theorems form the underlying principles of DFT and are usually stated as:

1. The three dimensional electron density of a many electron system uniquely determines all the ground state properties of the system.

2. The energy of a system can be defined as a functional of the electron density, with the minimum of the energy functional corresponding to the ground-state electron density.

Although apparently straightforward these statements greatly reduce the complexity of the problem to be solved. From the first theorem, rather than requiring solutions for the N electron wavefunction $\psi(x_1...x_N)$ containing 3N spatial dimensions, we now simply require knowledge of the three dimensional electron density $\rho(r)$. Furthermore from the latter theorem, by defining the energy functional for the system the ground state electron density of the system can be derived which uniquely defines all other properties of the system. Much of the complexity of the initial problem is now contained in defining a suitable energy functional for the system of interest. In their original paper Hohenberg and Kohn define the energy functional according to:

$$E[\rho(r)] = \int V_{ext}(r)\rho(r)d(r) + F[\rho(r)] \tag{2.51}$$

The first term describes the electron interaction with the external potential $V_{ext}(r)$, which includes the interaction of the electrons with the nuclei. The second term, $F[\rho(r)]$, contains information regarding the kinetic energy of the electrons (summed over all electrons) along with terms resulting from electron-electron interactions. Unfortunately the Hohenberg-Kohn Theorems do not provide an exact form for $F[\rho(r)]$ and so information necessary to calculate the ground-state of a many-electron system is still lacking. However, by providing a clear approach for solving the many-electron Schroedinger equation they laid the foundations for the development of DFT.

2.4.3 Kohn-Sham Equations

In 1965, building on the Hohenberg-Kohn Theorems, Kohn and Sham published a series of equations that allowed for the calculation of the ground state of a many-electron system [161]. These became known as the Kohn-Sham equations and form the basis of modern DFT. They postulated that for a given system containing a set of interacting electrons, with electron density $\rho(r)$, an equivalent system of non-interacting electrons, also with electron density $\rho(r)$, could be derived. By applying this to the problem the

unknown energy functional $F[\rho(r)]$ can be separated into a series of component terms as described by equation 2.52.

$$F[\rho(r)] = E_{ke}[\rho(r)] + E_H[\rho(r)] + E_{xc}[\rho(r)] \tag{2.52}$$

Here $E_{ke}[\rho(r)]$ is the kinetic energy of non-interacting electrons and $E_H[\rho(r)]$ is the Hartree term, containing the Coulombic energy of the electron-electron interactions. It must be noted that the Hartree term does not account for the correlation of electron motion. Instead the term is defined by the summation of the classical pairwise interactions between charge densities,

$$E_H[\rho(r)] = \frac{1}{2}\int\int \frac{\rho(r_1)\rho(r_2)}{r_1 - r_2} dr_1 dr_2 \tag{2.53}$$

Importantly, in principal both the kinetic energy (E_{ke}) and Hartree (E_H) terms are known. The final term, $E_{xc}[\rho(r)]$, is known as the exchange-correlation term and represents the contribution from electron exchange and electron correlation interactions. In addition, the exchange-correlation term also defines the energy difference between the theoretical non-interacting many electron system and the real system of interacting electrons. In essence the exchange-correlation term can be viewed as a term containing all the unknowns of the problem into a single component. Unfortunately the exact form of this term is unknown, except for a small number of trivial systems. Defining a suitable approximation for the exchange-correlation term is a vital and active area of DFT research and is discussed in more detail in **Section 2.4.4**.

Taking the assumption behind the Kohn-Sham energy functional and combining it with the Hohenberg-Kohn Theorems leads to the Schroedinger-like Kohn-Sham equation, given by:

$$\left[\frac{-h}{2m_e}\nabla^2 + V_{eff}(r)\right]\psi_i(r) = \epsilon_i\psi_i(r) \tag{2.54}$$

where $\psi_i(r)$ are the Kohn-Sham orbitals of non-interacting electrons, ϵ_i are the orbital energies and $V_{eff}(r)$ is the effective potential of the system. By minimizing this equation a stationary solution to the Schroedinger equation (subject to the inherent

assumptions) can be found. The effective potential of the system is defined by:

$$V_{eff}(r) = V_{ext}(r) + \int \frac{\rho(r')}{[r - r']} dr' + V_{xc}(r) \tag{2.55}$$

where $V_{ext}(r)$ is the external potential and $V_{xc}(r)$ is the exchange-correlation potential which is related to the exchange-correlation energy functional by

$$V_{xc}(r) = \left(\frac{\delta E_{xc}[\rho(r)]}{\delta \rho(r)} \right) \tag{2.56}$$

This formalism provides DFT with a method for finding solutions to the Schroedinger equation for an adequately defined system through a self-consistent iterative approach. Initially a 'best guess' of the electron density is made, typically a superposition of the all the single electron densities. This is used to generate a form for the effective potential (V_{eff}) which is then used in the Kohn-Sham equations (eq. 2.54) to generate the Kohn-Sham orbitals of the system. From these an improved estimate for the electron density of the system can be calculated from:

$$\rho(r) = \sum_{i}^{N} |\psi_i(r_i|^2 \tag{2.57}$$

This improved estimate of $\rho(r)$ is then used to update $V_{eff}(r)$ in an iterative process until a single value for the electron density is converged upon. From the second Hohenberg-Kohn Theorem this electron density will correspond to the ground state electron density, from which all ground state properties can be defined. Due to the nature of this approach DFT is often referred to as an iterative self-consistent field method. It should be clear that to generate an accurate $V_{eff}(r)$ at each step requires a suitable $V_{xc}(r)$ to be specified. Since this is unknown, defining a valid approximation to this term is critical to the accuracy of the ground state electron density thus calculated.

2.4.4 Approximate Exchange-Correlation Functionals

Although the exchange-correlation functional is unknown for most systems there are a limited number for which it has been calculated. A particularly useful form has been

derived for the homogeneous electron gas, where the exchange energy is known analytically and Monte Carlo methods have been used to accurately calculate the correlation energy. However, for most systems of interest an approximate exchange-correlation functional must be used. The choice is non-trivial as the approximations within the exchange-correlation functional are often a significant source of error in DFT calculations. Indeed different exchange-correlation functionals often give wildly different, and even contradictory, results. This applies both when considering different systems and even when considering different ground state properties within a system. Therefore the accuracy of DFT calculations relies on employing a functional which is valid for both the system and properties of interest. A vast, and ever growing, number of functionals are now available for typical DFT calculations with varying levels of suitability, accuracy and computational expense. These are derived either semi-empirically or purely theoretically, although opinion is mixed over which approach is best and depends on the exact calculations to be performed. The functionals used within this work are based upon the Local Density Approximation (LDA), its expansion the Generalized Gradient Approximation (GGA) and the Hubbard U corrected versions thereof (LDA+U/GGA+U). As such these will be discussed in detail. However, it should be noted that many other forms exist such as the TPSS or Minnesota Functionals [162, 163].

Local Density Approximation

The Local Density Approximation was first suggested by Kohn and Sham and is regarded as one of the simplest exchange-correlation energy functionals. However, it has proved remarkably accurate at calculating a range of ground-state properties and as such has proven to be one of the most popular approximations [164]. Within LDA it is assumed that the exchange-correlation per electron is equivalent to that of the homogeneous electron gas with density $\rho(r)$, and takes the form:

$$E_{xc}^{LDA}[\rho(r)] = \int \rho(r)\epsilon_{xc}^{hom}(\rho(r))dr \tag{2.58}$$

where $\rho(r)$ is the electron density and ϵ_{xc}^{hom} is the exchange-correlation energy per par-

ticle. This approximation works well in reproducing ground-state properties such as bond lengths, crystal structure and phonon frequencies to a high degree of accuracy in many materials. Highly accurate reproduction is even seen in systems which are known to be inhomogeneous, that is even in materials in which the electron density does not resemble that of a homogeneous electron gas. In part this is due to a somewhat fortuitous situation whereby LDA consistently underestimates the correlation energy but overestimates the exchange energy. As such, some of the errors involved are systematically cancelled. However, there are significant limitations to an LDA approach. Notably, LDA typically underestimates the band gaps of materials, overestimates binding energies and incorrectly predicts some structures of electronic ground states. When these properties are of interest higher order theories are required, with a common expansion of LDA being the Generalized Gradient Approximation (GGA).

Generalized Gradient Approximation

The assumption that the electron density is homogeneous is clearly fallacious for real chemical systems. As such, advanced functionals include information regarding the variation of electron density with respect to position. Typically these take a semi-local approach, whereby the local electron density $\rho(r)$ is considered along with variations in electron density in space. These are known as gradient-correlated functionals, of which the GGA functional is often regarded as the simplest version. The form of the exchange-correlation functional employed is given by,

$$E_{xc}^{GGA}[\rho] = \int \rho(r)\epsilon_{xc}^{GGA}(\rho(r), \nabla\rho(r))dr \tag{2.59}$$

It must be noted that whilst in LDA there is only one form for ϵ_{xc} (ϵ_{xc}^{hom}), in GGA many forms for the GGA functional exist. Some commonly used formulations have been derived by Perdew and Wang (PW91) and Wu and Cohen (WC) [165, 166]. However, one of the most popular functionals is based on the work of Perdew, Burke and Ernzerhof (PBE) [167]. This functional (and its derivative PBEsol) is the form employed in this work. The GGA approach has been shown to be highly effective for many non-metallic systems, reproducing properties such as crystal structure and

binding energies more accurately than LDA. However, although GGA reproduces the band gaps of materials with greater accuracy than LDA, it still typically underestimates the band-gap energies. This is particularly evident in materials containing strongly correlated electron systems, such as those with partially filled d- and f- orbitals. To overcome this a Hubbard U correction is often applied.

GGA+U

Systems containing strongly correlated electrons are often poorly represented by a standard LDA/GGA approach for the exchange-correlation functional. This includes materials containing elements with partially filled *d*- and *f*- orbitals, such as transition metals and rare earths. These are particularly relevant to the materials discussed in this work, which all contain transition metal elements. Using an LDA exchange-correlation functional on transition metal, or rare earth, containing systems leads to the prediction of partially filled d-bands, with metallic type electronic structures with itinerant d electrons. However, experimentally transition metal and rare earth compounds are known to present localised d and f electrons, leading to distinct and separate d electron occupied and unoccupied bands. Therefore, to match theory to experiment the exchange-correlation functional is modified to account for the strong on-site correlation of the *d*- and *f*- electrons. This is achieved by separating out the treatment of s and p electrons from d and f electrons, with their Coulombic interaction accounted for by a Hartree-Fock mean-field approximation. The strength of the correction made to the exchange-correlation functional is governed by the Hubbard Coefficient (U) leading to an LDA+U/GGA+U approach. The value of U directly affects the energy gap between occupied and unoccupied bands in the system and must be chosen carefully to correctly represent the system of interest. Often the value is chosen empirically so as to reproduce known properties of the material. See **Appendix B** for a tabulated selection of U_{eff} values taken from a number of DFT studies on battery materials in the literature.

2.4.5 Applying DFT to Solids

Conceptually solid state systems would present a problem when attempting to solve the Schroedinger equation. Since we typically deal with the bulk behaviour of systems we must treat the lattice as infinite in space. Given that the electron wavefunction extends over the entire lattice this means the wavefunction would be infinite, and require an infinite number of basis sets to be properly described. Thankfully the repeating nature of solids allows periodic boundary conditions to be applied, using inherent internal symmetry to reduce the problem from an infinite system to a finite tractable arrangement. Furthermore, this approach allows certain aspects of the problem to be described in reciprocal space, as opposed to real space, greatly improving the speed of computation. Solids also typically employ a planewave, as opposed to localised, description of the wavefunction, alongside a suitable psuedopotential approach. These aspects are described in detail below.

The Reciprocal Lattice and k-space

Although solid systems can intuitively be described in real space it is often more convenient to use a reciprocal space projection to define lattice properties, this is known as k-space. A real space description, in terms of a, b and c, can be projected into a k-space description in terms of a^*, b^* and c^* using the relationships,

$$a^* = 2\pi \frac{b \times c}{a.b \times c} \tag{2.60}$$

$$b^* = 2\pi \frac{a \times c}{b.a \times c} \tag{2.61}$$

$$a^* = 2\pi \frac{a \times b}{c.a \times b} \tag{2.62}$$

In real space the infinitely repeating lattice can be completely described by a primitive unit cell composed of lattice vectors a, b and c. Analogously, the infinite extent of k-space can be reduced to a primitive cell composed of a^*, b^* and c^*. This cell is known as the Brillouin Zone and is a fundamental concept in periodic solid state systems as within its volume a complete description of the wavefunction can be provided. This

concept is neatly encapsulated within Blochl's theorem [168].

Blochl's Theorem

Blochl's theorem is based upon the Brillouin zone description of k-space and states that the wavefunction of electron i, within a periodic field, can be written as the product of two distinct components: a wave-like term and a term with the same periodicity of the external field. Within solid sate systems this periodic external field corresponds to the periodicity of the unit cell. In this formulation the wavefunction can be written as

$$\psi_i(r) = e^{ik.r} f_i(r) \tag{2.63}$$

where k is the wavevector in the Brillouin zone and controls the frequency and direction of the wavelike term, r is the position vector. The periodic component of the wavefunction can be constructed through a combination of a basis set of discrete planewaves ($e^{iG.r}$) wherein the wavevectors (G) represent all translations to symmetrically identical lattice points. In this approach $f_i(r)$ becomes:

$$f_i(r) = \sum_G c_{i,G} e^{iG.r} \tag{2.64}$$

Combining eq 2.63 with eq 2.64 leads to a planewave description of the wavefunction given by

$$\psi_i(r) = \sum_G c_{i,k+G} e^{i(k+G.r)} \tag{2.65}$$

the solution of which is defined by the coefficient $c_{i,k+G}$. Performing this summation up to a suitable value of G is essential in ensuring an adequate description of a solid state system.

Planewaves (G)

As alluded to above the choice of planewave basis is critical to providing accurate results at reasonable computational expense. This involves the application of two approximations to reduce the complexity of the problem. Firstly, higher order planewaves, i.e.

those with larger $|G|$, will have a higher kinetic energy and as such contribute relatively less to the ground state wavefunction. Therefore, a $|G|$ (or energy) cutoff is applied to the summation in equation 2.65, above which planewaves are not considered to contribute significantly to $\psi_i(r)$ and are not evaluated. Secondly, as ψ is a continuous function of k small variations in k will have a limited impact on ψ. Hence, a suitable description of k-space can be provided by sampling a finite number of points in k-space. The set of "k-points" to be sampled can typically be made much smaller than the sampling points that would be required for a real space projection of the wavefunction. Furthermore, the inherent symmetry in most solid state systems means that often many k-points sample equivalent points in the Brillouin zone. Such double sampling is redundant and the number of k-points to sample can be reduced further through symmetry operations. This is typically done using either a Gamma point ((0, 0, 0) in the Brillouin zone) centred k-point mesh or one chosen with the Monkhurst-Pack method.

It is necessary, in actual DFT calculations, to test the validity of these approximations through a process known as convergence testing. In essence both the k-point sampling grid and planewave cutoff are varied and the effect on ground state properties of the system recorded. Strictly speaking convergence testing should be performed against the ground state wavefunctions of the system. However, as should be clear from previous sections, this is not possible within the framework of DFT, hence ground state properties are used as a proxy for the wavefunction. Convergence is considered to have occurred when properties of interest do not vary upon further variations in k-point grid and planewave cutoff values. The exact properties against which convergence occurs will depend on which properties are of interest and both the rate of convergence, and degree of desired accuracy, can vary significantly across ground state properties. It is also important to consider that the lowest planewave cutoff (and coarsest k-point mesh) which satisfy all convergence criteria are typically used in practical calculations to minimise the computational expense, which can be significant for very large planewave cutoffs and fine k-point meshes.

Pseudopotentials

As the wavefunction approaches the nuclei of an atom it tends to vary significantly, with a large degree of fine spatial detail. As such, to accurately describe the wavefunction of the core electrons a large number of high energy planewaves would be required to encapsulate all this fine detail, due to the inverse relationship between energy and wavelength. As discussed above this adds considerably to the computational expense of the calculation, and significantly reduces calculation speed. However, the core electrons do not typically participate in chemical bonding and for a given atomic system can be considered essentially constant and independent of the atomic environment. Therefore a common approximation is to separate the treatment of the core and valence electrons of an atom into two distinct regions through the use of pseudopotentials.

The core potential is represented by a smooth function, the pseudopotential, whilst the valence electrons undergo full DFT treatment. Since the pseudopotential is designed to vary smoothly in space it can be accurately represented by a reduced set of planewaves, allowing a smaller cutoff energy to be chosen, reducing the computational expense. This approximation relies heavily on the definition of core and valence electrons, i.e. which electrons can accurately be described by a pseudopotential and which cannot. Typically the distinction is made through the use of a cutoff radius, within which a pseudopotential description is applied which suitably represents the original core potential. By applying this approximation the generated wavefunction will only provide a reliable representation of the valence electrons of the system. However, if the cutoff radius is chosen correctly then this is acceptable for many ground state properties of real systems. If the accurate representation of the core electron wavefunction is required then all electron codes, such as WIEN2K, can be used [169].

An important characteristic of a pseudopotential representation is it "softness", describing both the smoothness of the function and the size of the cutoff radius from the nuclei. A softer pseudopotential can generally be described by fewer planewaves. However, a very soft pseudopotential is poorly transferable between systems as it requires a large cutoff radius and leads to a less accurate representation of the atom. Therefore a trade off in "softness" is necessary, whereby an ideal pseudopotential will accurately reproduce the wavefunction for the valence electrons of the atom across a wide range (preferably all) chemical systems. Whilst pseudopotentials can be derived empirically

it has generally been found that the most effective pseudopotentials are derived from *ab initio* approaches. A particularly successful pseudopotential, and the one employed in this work, is contained within the Projected Augmented Wave (PAW) method [170]. The PAW method invokes a particularly soft pseudopotential in combination with local auxiliary functions to allow it to represent the complete all-electron wavefunction.

2.5 Surface Calculations

Previous sections describing computational techniques have dealt with bulk crystal simulations, where the lattice can be considered as extending infinitely along all spatial dimensions. However, electrochemical properties are often highly correlated with the surface structures and energetics of cathode materials, and many methods for modifying the electrochemical performance of battery materials involve producing nanoparticulates. Unfortunately, it is difficult to extract detailed surface information from experiment alone, indeed often even identifying which surfaces are present is a considerable challenge. Therefore, simulation can be used to explore surfaces on an atomistic level, detailing the energetics and local surface relaxation, along with how this gives rise to particular nanoparticle morphologies. To do so there are two potential methods for generating surface structures computationally. The first maintains 3-D periodic boundary conditions and essentially produces a series of non-interacting "slabs". The second requires breaking of the symmetry along one lattice vector so as to directly simulate a bulk to vacuum transition using 2D periodic boundary conditions. Both methods are used in this work and discussed below.

It important to note here that a variety of surface types exist, as defined by Tasker, and care must be taken in the setup of the simulation cell [171]. These surface types are known as types I, II and III depending in the structural nature of the 'as-cut' surface. Type I surfaces are formed by stoichiometric charge-neutral layers of cations and anions, thus no dipole moment is present normal to the surface. In type II surfaces, although each layer is not charge neutral a finite group of layers form a charge-neutral repeat unit, again leading to zero net dipole moment orthogonal to the surface plane. In type III surfaces a dipole moment always exists normal to the surface, irrespective of where

the surface is cleaved and how many layers are included in the repeat unit, meaning stable surfaces cannot be obtained. However, these surfaces are found in nature where surface reconstruction occurs, removing the perpendicular dipole moment. Typically this involves oxidation/reduction of surface ions or surface reconstruction, leading to a non-stoichiometric surface. Examples of the various surface types are given in Figure 2-9.

3D Periodic Surfaces

3D periodic surface calculations maintain full periodic boundary conditions, generating images of the cell along all Cartesian vectors. Each unit cell is composed of two regions, a slab region containing all the ions and a vacuum region separating slabs from their periodic images. This is shown schematically in Figure 2-10(a). The size of the vacuum region is critical to ensure that slabs are not influenced by their periodic images normal to the slab surface. That said an arbitrarily large vacuum region adds considerably to the computational expense of the technique. As such convergence testing is required, whereby the vacuum thickness is increased until surface energies remain constant, at which point the slabs are considered to be isolated from one another. The slab region is composed of a symmetric set of ions, such that inversion symmetry exists through the centre of the slab. Thus the slab is in essence composed of two identical surfaces with exactly opposed miller indexes. The surface energy per unit area must be calculated from the slab energy by,

$$E_{surface} = \frac{E_S - E_B}{2A} \tag{2.66}$$

where E_S is the total energy of the slab, E_B is the energy of an equivalent number of ions in the bulk and A is the area of one surface of the slab. The factor of 2 arises as each slab contains 2 identical surfaces. As with the vacuum region the thickness of the slab is critical to ensure accurate results. Ideally ions in the centre of the slab should demonstrate bulk behaviour, to ensure that all surface related relaxation is correctly accounted for. Therefore the slab should be sufficiently thick for this condition to hold. Increasing the slab thickness beyond this point will not give more accurate results but will considerably increase computational expense. As such, as with the size of the vacuum region, the slab thickness must be converged against surface energy.

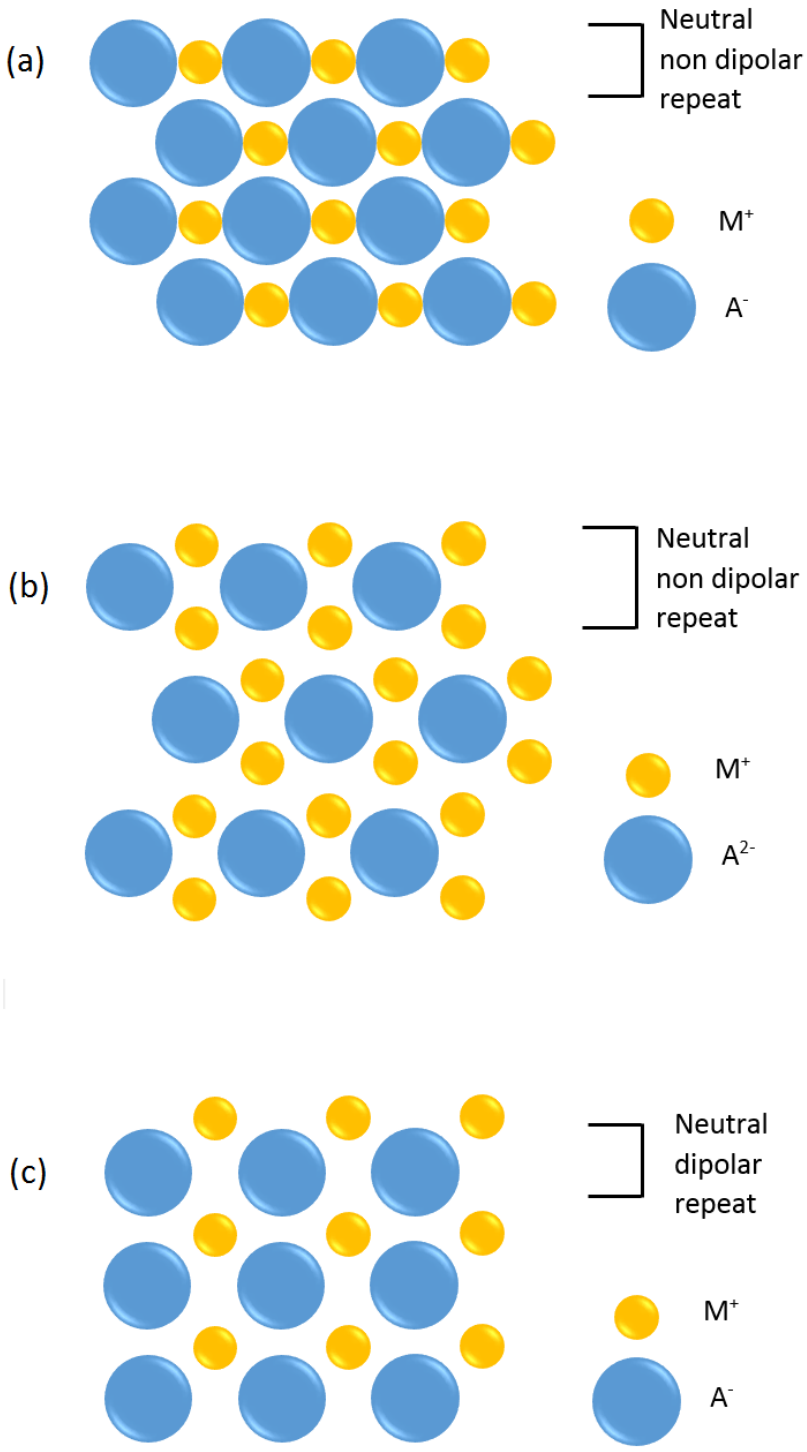

Figure 2-9: *Examples of Tasker Type I, II and III surfaces with (a) Type I, (b) Type II and (c) Type III.*

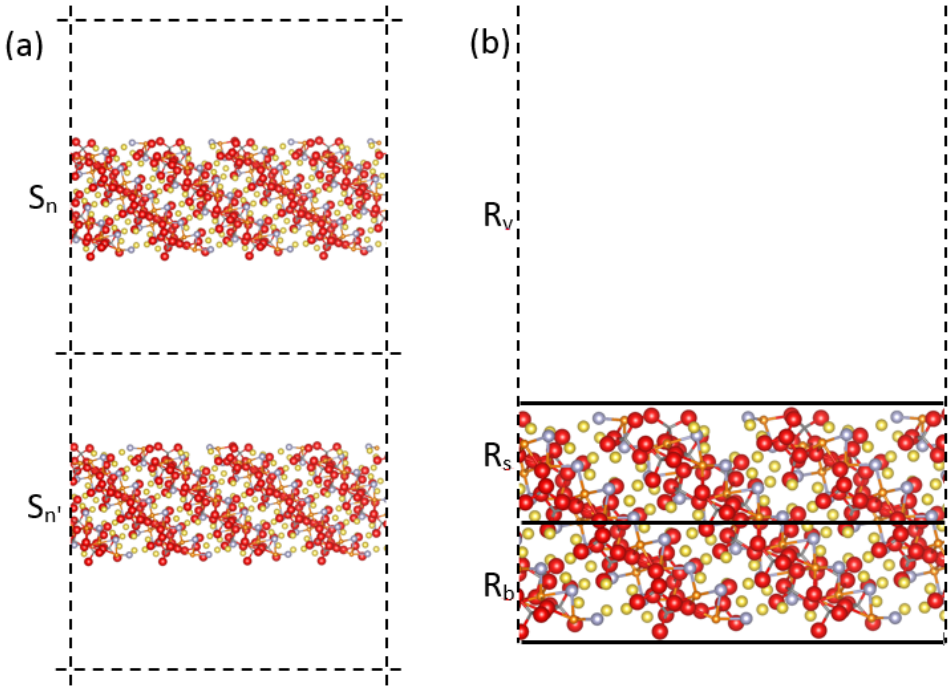

Figure 2-10: *Diagram of a (a) 3D periodic vs a (b) 2D periodic surface calculation model. In the 3D model boundary conditions (dashed lines) extend over* x, y *and* z *whilst in a 2D periodic model they extend only over* x *and* y. *As a result 3D periodic models contain and infinite series of non-interacting slabs (S_n, $S_{n'}$ ...). The 2D periodic model is split into 3 regions: a bulk region (R_b), a surface region (R_s) and an infinite vacuum region (R_v).*

2D Periodic Surfaces

For 2D periodic surface calculations the crystal section is composed of two regions. The ions within the upper region (region 1) are relaxed explicitly, using efficient energy minimisation techniques to locate the local minima, allowing surface relaxation effects to be taken into account. As such region 1 consists of the surface layer plus several layers into the bulk, in which significant relaxation can occur. This region is bounded on one side by an essentially infinite vacuum layer and on the other by a second crystal region (region 2) in which the crystal is assumed to behave as in the bulk, with the atoms fixed at their equilibrium positions. This setup is shown in Figure 2-10(b). The depths of region 1 and 2 must be chosen to be large enough to allow convergence of the surface energies, typically extending over 200-500 ions. Once the surface simulation has been constructed the surface energy per unit area can be extracted through equation 2.66, without the factor of 2 in the denominator. The advantage of this approach over a 3D periodic system is that it allows direct simulation of a single surface, rather than relying on a surface pair. Furthermore since the vacuum level is essentially infinite there is no need to spend resources converging the surface energy against this parameter.

Several points emerge in relation to both 2D and 3D methodologies. Firstly the simulations relate to planar surfaces and internal energies at zero Kelvin. Secondly, relaxation at the surface is conducted at constant volume, consequently permitting no lateral expansion/contraction of the unit cell. However, typically the constant volume constraint is a good approximation for the enthalpies at constant pressure, thereby being commensurate with experiment. This is discussed in more detail by Masri et al [172]. Finally, it should be noted that for 2D periodic systems the Ewald summation described previously is replaced by a similar method developed by Parry. This method accounts for the effects of the surface region and is used in computing the long-range Coulomb terms of the surface energy.

Morphologies

There are two methodologies commonly applied to calculate crystal morphologies from the crystal structure and surface energies, based either on equilibrium or kinetic considerations. The first, initially expounded by Gibbs, is based on the notion that a crystal

in equilibrium with its surroundings must act to minimise the net surface energy for a given volume, that is

$$\gamma = \sum_i \gamma_i A_i = \textit{minimum for constant volume} \tag{2.67}$$

where γ_i and A_i are the surface energy and area for the i^{th} crystallographic plane. This was expanded upon by Wulff, leading to the concept of a Wulff plot, in which the equilibrium morphology is obtained by taking the distance from the origin to the central point of a surface $\{hkl\}$ as directly proportional to the corresponding surface energy,

$$h_i = \lambda \gamma_i \tag{2.68}$$

where h_i is the normal vector to the i^{th} face and λ is a crystal size dependent constant. A crystal morphology derived from this method is often referred to as the 'equilibrium' morphology [173]. The second approach to calculating crystal morphologies is based on Hartman-Perdock theory, in which kinetic factors influencing crystal growth are accounted for by using the attachment energy of each crystal plane, rather than its surface energy. The attachment energy is defined as the energy per formula unit released when a new slice, of depth *d_hkl*, is attached to the crystal face. Mathematically this can be expressed by,

$$E_{attach} = \frac{E_{crystal} - E_{slice}}{n} \tag{2.69}$$

where $E_{crystal}$ is the energy of the crystal, E_{slice} is the energy between all the ions within the slice *hkl* and n is the number of formula units per slice. The attachment energy is assumed to be proportional to the growth rate in a layer-by-layer mechanism, hence surfaces with lower attachment energies will demonstrate lower growth rates and be significantly expressed in the crystal morphology. A crystal morphology produced from this approach is typically termed the 'growth' morphology. Calculation of E_{slice}, and subsequently E_{attach}, is readily implemented in the GULP code using a 2D periodic surface model. The composition of the growth slice can be defined in the input file, after which GULP calculates the attachment energy using the formula above.

It must be noted that significant approximations and assumptions are involved in both approaches. Firstly, as calculations are performed in a vacuum the effects of additional

species and precursors in the system are completely absent. Secondly, the effect of external conditions, such as temperature or pressure, are not explicitly accounted for despite the impact they are known to have on as synthesised nanoparticles. Finally, for the growth morphology the growth rate is assumed to be proportional to the attachment energy. However, there is no strong theoretical underpinning for this assumption. Despite this the methods have had many successes in exploring the fundamental properties of nanoparticles.

2.6 Calculation Information

To conclude this methods chapter, a summary of the key computer hardware features is presented.

Computational Equipment

The differing computational demands of atomistic, large scale MD and DFT calculations mean a variety of computer hardware was used in this work. Atomistic simulations (using the GULP code) were run in serial on local desktop machines. This typically involved a single core on a Quad-core i5 3.20 GHz processor with 4GB RAM. When a large number of distinct GULP simulations were to be run a CONDOR high throughput machine was used. Each calculation was run simultaneously, with calculations submitted when and as cores became available, with typical desktop specifications of 2 x Quad-Core AMD Opteron 2360 SE 2.5 GHz and 32GB RAM. The MD and DFT calculations are more computationally intensive, and therefore parallelization was used to reduce the real time required. In this way larger problems can be separated into smaller components and processed in parallel. All MD and DFT simulations were run on the UK's high performance computing facility ARCHER, with between 4-480 cores through the Materials Chemistry Consortium (MCC) led by UCL. MD calculations were performed in the DL_POLY [141] and LAMMPS [142] codes, whilst all DFT

calculations were run using the VASP [143, 144] code.

Calculation Speed

There is a hierarchy in the length of time taken to run calculations based primarily on the level of theory and size of simulation cell employed. The fastest calculations were typically atomistic single point energy minimisations (performed using the GULP code) taking 1-100 s. Defect simulations require the Mott-Littleton approach and as a result take around an order of magnitude longer to run, approximately $10^2 - 10^3$ s. This is highly dependent on the sizes of region I and IIa required to converge the defect energy, often found to be at least 12 Å and 24 Å respectively. All these types of calculation can be run on a single core on local machines. However, MD simulations need large supercells to provide adequate statistics, typically containing 15,000-30,000 ions run over 100,000-1,000,000 time steps. As such, these calculations require multiple cores (4-72) on ARCHER run in parallel for 12-48 hrs. Finally *ab initio* DFT calculations, performed in the VASP code, used between 144-480 cores on ARCHER run in parallel for 8-24 hrs.

3 Na-ion Mobility in Olivine $NaFePO_4$ and Layered Na_2FePO_4F

"The science of today is
the technology of tomorrow"
Edward Teller

3.1 Background

With the recent rise in prominence of Na-ion battery research, as introduced in **Chapter 1**, there is renewed impetus to discover and develop novel Na-ion cathodes. Materials such as NASICON [174], $NaVPO_4F$ [94], $NaFePO_4$ [92, 131, 175] and Na_2FePO_4F [110, 130, 176], which contain "polyanions" in their framework have recently been investigated. Unlike layered Na oxides, they usually display a flat voltage response upon Na-(de)intercalation due to their structural energetics that drives two-phase behaviour and formation of a well-defined phase boundary between Na-rich and Na-poor phases. Their robust and stable frameworks often display better capacity retention than the oxides at the expense of slower kinetics. While there have been many theoretical and experimental studies of Li-ion migration behaviour in such systems analysis of the energetics of Na-ion migration has been mush rarer [177].

Our interest here focuses on the polyanion materials owing to their potentially more sta-

ble cycling behaviour, and the insights that can be gleaned by comparing Na-ion transport in the one dimensional channels of the olivine, $NaFePO_4$, to that in the two dimensional layers of the phosphate, Na_2FePO_4F. Olivine $NaFePO_4$ can be synthesised by ion exchange from the parent lithium iron olivine [131, 133]. It (de)intercalates Na-ions at 3.2 V at very slow rates of discharge. The mixed Fe-Mn system $NaFe_{0.5}Mn_{0.5}PO_4$ was also synthesised recently by direct methods [133], and it gives a characteristically sloping electrochemical curve when cycled in a Na-ion battery. We note that conflicting reports have emerged regarding the electrochemical properties of olivine $NaFePO_4$. While the initial study by Moreau et al. [131] indicated that carbon coating of the parent material $LiFePO_4$ did not impact the electrochemical performance of olivine $NaFePO_4$, recent investigations by Zhu et al. [43] has demonstrated superior electrochemistry properties upon carbon coating (100 mAg^{-1} at 0.1 C rate) than that obtained previously. The performance is still inferior to that of the carbon coated lithium analogue, however.

Layered Na_2FePO_4F was first synthesised, and electrochemically investigated by Ellis et al. [130] The structural refinement was carried out on single crystals grown from a reaction melt. The unique ability of this structure to reversibly intercalate Li/Na ions without any significant stress stems from its robust 2D framework created by interconnected FeO_4F_2-PO_4 polyhedra that form two-dimensional slabs. Na^+ ions are nestled both near the sheets, and also between the layers in the interplanar region [109]. The interlayer cations are conserved during cycling, acting as pillars to stabilise the structure. Importantly, the material exhibits only a small volume difference (3.7%) when Na ions are de-intercalated from the 2-D layers of the structure. The initial electrochemical study demonstrated facile and reversible intercalation of Li^+ when the material was used as a cathode in a Li cell, via rapid exchange of Na^+ in one of the sites with Li^+. Na_2FePO_4F also intercalates Na^+ ions reversibly at an average of 3.0 V, as later demonstrated for both ionothermally [110], and solid state [111, 176] prepared materials. Capacities of about 110 mAg^{-1} were obtained at current densities of 12.4 mAg^{-1} with as little as 1.3 wt % carbon coating using ascorbic acid as the carbon source, which also had the positive effect of reducing particle size [111]. This suggests acceptable rate capability comparable to that obtained in the Li cell, despite the larger

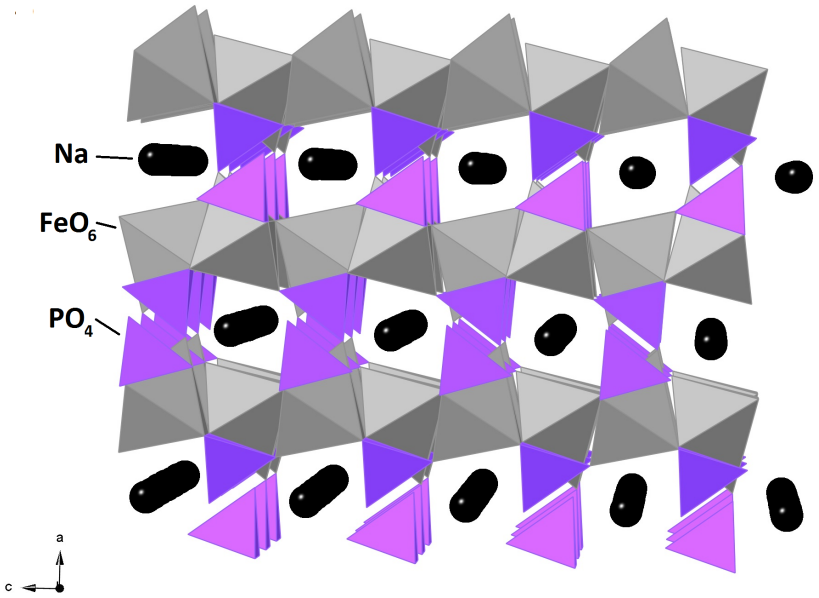

Figure 3-1: *Experimentally determined olivine crystal structure of $NaFePO_4$ with Na in black, FeO_6 octahedra in grey and PO_4 tetrahedra in purple [175].*

size of the Na^+ cation.

To gain a greater understanding of the atomic-scale features influencing the electrochemical properties of layered Na_2FePO_4F and olivine $NaFePO_4$, we report here a computational study using well-established atomistic simulation methods to investigate Na-ion transport and the formation of intrinsic defects in these two contrasting materials. The author acknowledges Dr Rajesh Tripathi and Prof. Linda Nazar (Waterloo, Canada) who performed some of the calculations relating to the $NaFePO_4$ compound. For a published version of this work see [132] and **Appendix H**.

3.2 Structural Modelling

In the olivine $NaFePO_4$ structure (space group: Pnma), FeO_6 octahedra link to each other via corner sharing in the *ab* plane. Sandwiched between these planes are PO_4 tetrahedra which share corners and edges with the MO_6 octahedra. This well-known framework provides open channels along the *b*-axis in which Na ions are located (Fig. 3-1). A unique ordered composition, $Na_{0.7}FePO_4$ is also reported to form on electrochemical oxidation of $NaFePO_4$, although its precise structure has not yet been

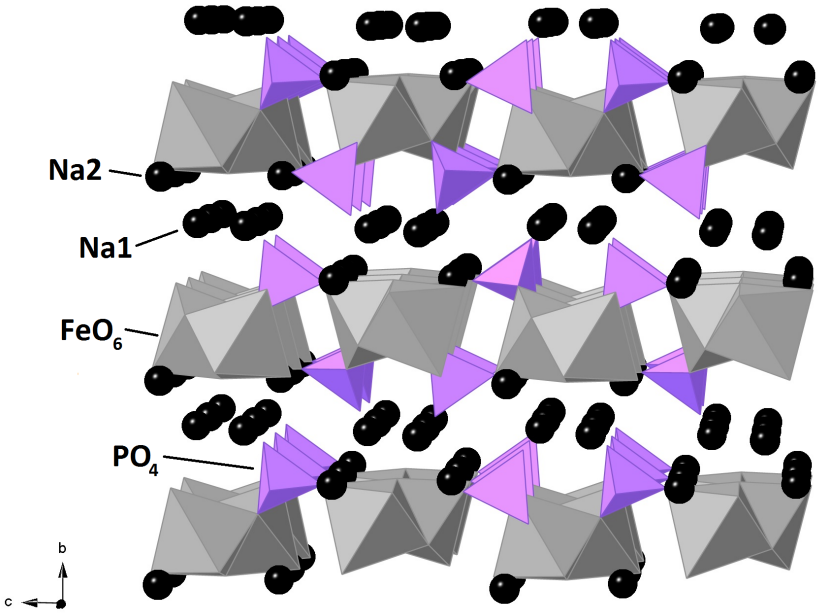

Figure 3-2: *Experimentally determined crystal structure of Na_2FePO_4F with Na in black, FeO_4F_2 octahedra in grey and PO_4 tetrahedra in purple [103].*

elucidated [131]. In the layered Na_2FePO_4F structure, Fe^{2+} ions are located on two crystallographic sites (Fe1 and Fe2) and coordination polyhedra around them are connected to form face-sharing bi-octahedral units. These units are connected in the *a*-direction to form Fe-F-Fe chains. The parallel chains are connected to each other by PO_4 tetrahedral units along the *c*-direction, thus forming a layer of $Fe_2O_6F_3$-PO_4 units in the *ac* plane. Na^+ ions reside in these interlayer spaces (Fig. 3-2).

These two structures, which differ greatly in their architecture - but not too significantly in chemical composition - provide a good platform to investigate the factors underlying the observed electrochemical properties. Initially, potential sets were developed to accurately reproduce these structures, along with providing sensible dieletric constants and bulk moduli (although exact experimental values for these are not known). Potentials published for $LiFePO_4$ and $NaFeSO_4F$ were taken as a starting point [178, 179]. Energy minimisations during fitting were performed at constant pressure to allow cell volume to relax along with ion positions. Through a least squares fitting regime the potential set given in Table 3.1 was refined. Separate Na-O potentials (Na-O and Na-O* for Na_2FePO_4F and $NaFePO_4$ respectively) were developed as initial work on the materials was performed independently. The calculated lattice parameters and com-

parison to the experimentally reported values for $NaFePO_4$ and Na_2FePO_4F are shown in Tables 3.2 and 3.3 respectively.

Table 3.1: *Potential parameters derived for Na_2FePO_4F and $NaFePO_4$. The Na-O potential was used to model Na_2FePO_4F whilst the Na-O* potential was used to model $NaFePO_4$, all other potentials were constant. k and Y refer to primary ion in potential.*

Buckingham

Interaction	A (eV)	ρ (Å)	C (eV.Å^6)	k	Y
Na-O	1497.830598	0.287483	0.0	9999	1.000
Fe-O	1105.240900	0.310600	0.0	19.26	-0.997
O-O	22764.30000	0.149000	44.53	65.00	0.960
P-O	897.2648000	0.357700	0.0	9999	5.000
Na-F	2810.326262	0.246520	0.0	9999	1.000
Fe-F	5609.254200	0.227000	0.0	19.26	-0.997
O-F	11555.389081	0.244179	41.184828	65.00	0.960
F-F	1153.000000	0.136500	0.0	63.5772	1.321
Na-O*	560.00000	0.3200	0.0	9999	1.000

Three Body

Interaction	k (ev.rad^{-2})	θ_0 (deg)
O-P-O	1.3226	109.47

Table 3.2: *Comparison of experimental and calculated structural parameters of $NaFePO_4$, displaying lattice parameters and mean bond lengths [175].*

Lattice Parameters for $NaFePO_4$

Parameter	Exptl	Calc	Δ
a (Å)	10.4109	10.3167	-0.0942
b (Å)	6.2283	6.1635	-0.0649
c (Å)	4.9521	4.9293	-0.0228

Mean Bond Lengths

Bond	Exptl (Å)	Calc (Å)	Δ
Na-O	2.344	2.333	-0.011
Fe-O	2.185	2.148	-0.037
P-O	1.539	1.551	0.012

Table 3.3: *Comparison of experimental and calculated structural parameters of Na_2FePO_4F, displaying lattice parameters and mean bond lengths [103].*

Lattice Parameters			
Parameter	**Exptl**	**Calc**	**Δ**
a (Å)	5.220	5.231	-0.011
b (Å)	13.854	13.847	0.008
c (Å)	11.7792	11.744	0.034
α (°)	90.0	90.0	0.0
β (°)	90.0	90.0	0.0
γ (°)	90.0	90.0	0.0
Mean Bond Lengths			
Bond	**Exptl (Å)**	**Calc (Å)**	**Δ**
Na-O	2.408	2.408	0.000
Na-F	2.401	2.459	0.058
Fe-O	2.121	2.090	0.031
Fe-F	2.134	2.141	0.077
P-O	1.537	1.547	0.010

Lattice parameters (unit cell lengths and angles) for the olivine and layered compounds were simulated within a maximum difference of 1.2% from experimentally reported values. The bond lengths were also very similar. Reproduction of the lattice parameters and bond lengths provides additional validity to the interatomic potentials used for simulating defects and Na-ion migration.

3.3 Intrinsic Defects

Insight into the defect properties of cathode materials is crucial to the full understanding of their electrochemical behaviour, especially the possibility of "blocking" anti-site defects in 1D ion conductors. The energy of formation of various types of Schottky and Frenkel defect were calculated by combining isolated vacancy and interstitial energies (see **Appendix D**) using the following types of equations (in Kroger-Vink notation):

$$Na_{Na}^{\times} \rightarrow V_{Na}' + Na_i^{\bullet} \tag{3.1}$$

$$Fe_{Fe}^{\times} \rightarrow V_{Fe}' + Fe_i^{\bullet} \tag{3.2}$$

$$2Na_{Li}^{\times} + O_O^{\times} \rightarrow 2V_{Na}' + V_O^{\bullet\bullet} + Na_2O \tag{3.3}$$

$$Fe_{Li}^{\times} + O_O^{\times} \rightarrow V_{Fe}' + V_O^{\bullet\bullet} + FeO \tag{3.4}$$

$$2Na_{Li}^{\times} + Fe_{Fe}^{\times} + P_P^{\times} + 4O_O^{\times} + F_F^{\times} \rightarrow 2V_{Na}' + V_{Fe}'' + V_P'''' + 4V_O^{\bullet\bullet} + V_F^{\bullet} + Na_2FePO_4F \tag{3.5}$$

Anti-site defects which form by exchanging cations (Li^+/Fe^{2+}) on neighbouring sites have been reported to significantly affect the electrochemical performance of the olivine $LiFePO_4$. We examined the possibility of such Na/M anti-site defect formation in both materials, which can be written as follows:

$$Fe_{Fe}^{\times} + Na_{Na}^{\times} \rightarrow Fe_{Na}^{\bullet} + Na_{Fe}' \tag{3.6}$$

Resulting defect energies are listed in Table 3.4. The high formation energies indicate that all of the Frenkel and Schottky defects are unfavourable in olivine-type materials and would only be present in negligible concentrations in the bulk. This trend is similar to the energies of defect formation previously reported for $LiFePO_4$[178]. In contrast, antisite defects are found to have low defect energies (Table 3.4) which indicates that these are the most favourable type of intrinsic disorder in olivine $NaFePO_4$. Indeed, the much lower energy of formation compared to $LiFePO_4$ (0.86 vs. 1.13 eV [178]) is consistent with the fact that upon heat treatment, olivine $NaFePO_4$ readily transforms to the more thermodynamically stable maricite phase[180], where, compared to the

olivine, the Na and Fe sites are switched in the structure[181]: i.e., the alkali cation occupies the M2 site, and the transition metal occupies the M1 site. The thermodynamic preference of the maricite structure over olivine for $NaFePO_4$ has also been confirmed by computation[131, 177].

Table 3.4: *Calculated formation energies of intrinsic defects in Na_2FePO_4F and $NaFePO_4$.*

		Energy (eV)	
Defect Type	**Equation**	**Na_2FePO_4F**	**$NaFePO_4$**
Na Frenkel	3.1	3.22	2.25
Fe Frenkel	3.2	5.24	6.6
O Frenkel	-	6.81	-
F Frenkel	-	2.85	-
Schottky	3.5	32.0	-
Na_2O Schottky	3.3	10.78	10.05
FeO Schottky	3.4	5.19	7.31
Na/Fe antisite	3.6	1.00	0.86

Site preference is driven by a complex interplay between cation charge and size effects. In olivine $LiFePO_4$, where Li^+ (r = 0.76 Å) or Fe^{2+} (r = 0.78 Å) are effectively the same size, the higher charge on Fe^{2+} results in preference for the M2 site. However, when the size mismatch is significant, the larger cation (Na^+; r = 1.02 Å) is driven onto the M2 site. As noted above, the only method for preparing electrochemically active olivine $NaFePO_4$ relies on the topotactic conversion of olivine $LiFePO_4$ via a delithiation-sodiation process or a low temperature synthesis method involving a topotactic conversion of $NH_4Fe_xMn_{1-x}PO_4.H_2O$ in $NaFe_xMn_{1-x}PO_4$. The fact that direct methods cannot be used to prepare crystalline olivine $NaFePO_4$ confirms the highly metastable nature of this phase and consequently its tendency for cation disorder. The topotactic synthesis method ensures that the obtained product forms with a minimum concentration of antisite defects. However, the extraction of Na during electrochemical charge may trigger the formation of antisite defects as has been observed for $Li_{0.90}Ni_{0.45}Ti_{0.55}O_2$ obtained from $Na_{0.90}Ni_{0.45}Ti_{0.55}O_2$ [182].

In the context of ion diffusion, the antisite defects bear more significance in the case of olivine materials as their presence blocks the only available 1D channel for alkali ion migration. Therefore, anti-site defects demand that diffusion occurs via higher energy pathways, ultimately raising the energy barrier for Na/Li ion migration in the structure[178]. This results in the reduced power and capacity of the cathode material. For layered Na_2FePO_4F (Table 3.4), all the Frenkel and Schottky defects are also unfavourable. The energy of formation of antisite defects is much lower, and also comparable to that of the olivine, and suggests a small, significant percentage of Fe on Na sites and vice versa in the layered structure. This is similar behaviour to other phosphates (e.g. $LiFePO_4$) and contrasts with fluorosulphates [132, 178, 179].

3.4 Na-ion Migration

For olivine $NaFePO_4$, we examined possible Na migration pathways already identified for Li migration in olivine $LiFePO_4$ [178]. These paths are: (i) along [010], (ii) along [001], and (iii) along [101]. The path along the *b*-axis [010] provides facile channels for Na-ion migration. Along the [001] path, Na^+ ions are at relatively long distances from each other and coordination polyhedra surrounding Fe and P provide a narrow window for ion migration. The path along [101] bisects the *a* and *c*-axes and passes through a narrow window formed by FeO_6 and PO_4 polyhedra. Table 3.5 lists the calculated energies for these pathways. Activation energies along the [001] and [101] paths are relatively high (>1.5 eV), as expected from the above descriptions and are therefore unfavourable for Na^+ ion migration. This finding is similar to that reported for Li ion migration in $LiFePO_4$ [183]. Interestingly, the activation energy along [010] is lower than the activation energy calculated for Li ion migration along the same direction in $LiFePO_4$ (0.55 vs. 0.31 eV). Our Na migration energy is very similar to that calculated by Ong et al. [177] using DFT methods, although they and find a slightly lower Li migration energy for $LiFePO_4$, and note that the energy barrier differences for Na and Li migration are highly structure dependent.

Figure 3-3 shows the minimum energy migration pathway for Na ions indicating a curved trajectory between Na sites along the 1D channel (rather than direct linear

Table 3.5: *Migration barriers for potential Na^+ diffusion pathways in $NaFePO_4$ relating to Figure 3-3.*

Direction	E_{mig} (eV)
[010]	0.32
[001]	2.73
[101]	3.03

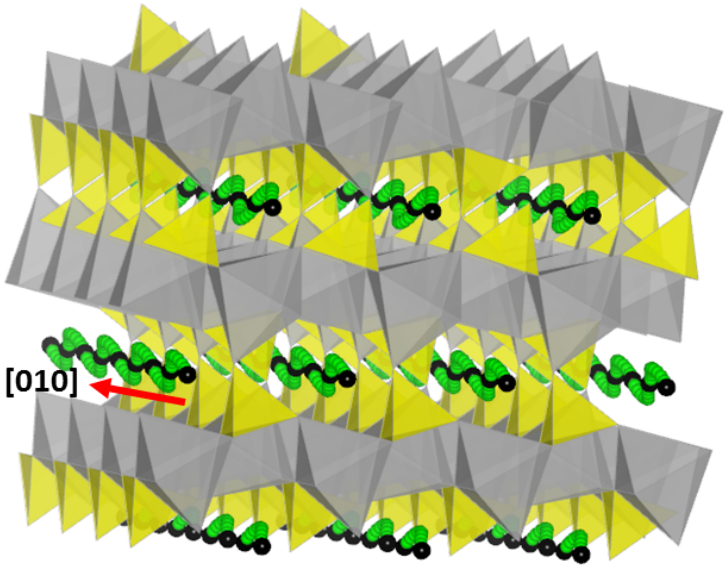

Figure 3-3: *Lowest energy Na migration pathways in $NaFePO_4$ with Na sites in black, FeO_6 octahedra in grey, PO_4 tetrahedra in yellow and low energy Na^+ paths in green.*

jumps). A very similar pathway for Li ion migration in $LiFePO_4$ was previously predicted by Islam et al. [178] and was subsequently confirmed by neutron diffraction maximum entropy methods [184].

The higher mobility of Na^+ in $NaFePO_4$ in comparison to Li^+ in isostructural $LiFePO_4$ could be attributed to much longer average lengths of Na-O bonds (2.34 Å) than Li-O bonds (1.96 Å). This suggests that the tunnels along the *b*-axis are more spacious in Na-compounds but naturally the size of the Na^+ cation is also larger than that of Li^+. In addition, it is known that polarizability effects are important as there are differences between the transport behaviour of highly polarizing cations such as Li^+ and that of less polarizing cations such as Na^+.

In contrast, the layered Na_2FePO_4F unit cell has six unique Na-Na distances (numbered

N1 to N6) leading to the possible migration paths that were considered and shown in Fig 3-4(a). Fig. 3-4(b) and (c) display examples of the migration window available for Na migration along the *a* and *c*-axes. Na^+ ion polyhedra connected by hops N2 and N6 share edges with each other, whilst polyhedra connected by hop N3 and N5 share faces. Fig. 3-5(a) and (b) illustrate the lowest energy migration paths for Na^+ and the associated energy barriers for Na_2FePO_4F. The activation energy for inter-layer transport was also calculated, but is not shown on the diagram since its value is much higher (>2 eV).

Table 3.6: *Migration barriers for potential Na^+ diffusion pathways in Na_2FePO_4F relating to Figures 3-4 and 3-5.*

Path	E_{mig} **(eV)**
N1	1.27
N2	0.59
N3	0.24
N4	0.31
N5	0.29
N6	0.44
Interlayer	>2

The results (Table 3.6) reveal that the lowest energy pathways in Na_2FePO_4F involve Na migration parallel to the *a*- and *c*-axes with energy barriers for long-range diffusion of about 0.3 and 0.4 eV respectively. Fig. 3-5 indicates that migration in the *c*-direction occurs through N4-N3-N6 hop sequences, and that migration in the *a*-direction occurs through an N3-N5 pathway. These results show that there should be high Na^+ mobility within the *a*-axis and *c*-axis channels, and 2D Na migration in the *ac* plane. This behaviour contrasts with that of $NaFePO_4$, which only allows Na^+ migration along 1D channels parallel to the *b* axis. Most importantly, ion blocking by anti-site defects is much less likely to make a significant difference to Na-ion migration in Na_2FePO_4F than it does in olivine materials exhibiting 1D diffusion. It is interesting that the calculated energy barriers in Na_2FePO_4F are almost the same as in olivine $NaFePO_4$ (∼0.3 eV), but much lower than the values found for tavorite-type $NaFeSO_4F$ (>0.6 eV) using similar simulation methods [179].

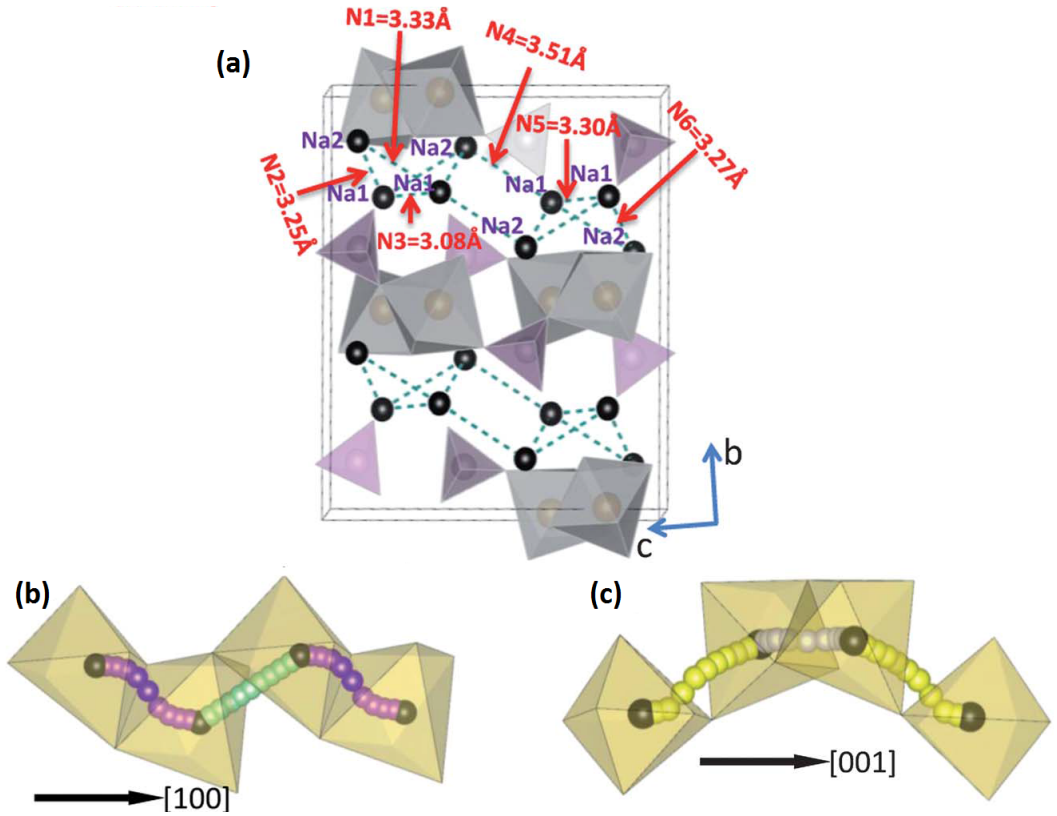

Figure 3-4: *Low energy Na^+ migration pathways in Na_2FePO_4F with Na sites in black, FeO_6 octahedra in grey and PO_4 tetrahedra in purple. (a) potential migration paths examined,(b) migration window along* a *axis and (c) migration window along* c *axis.*

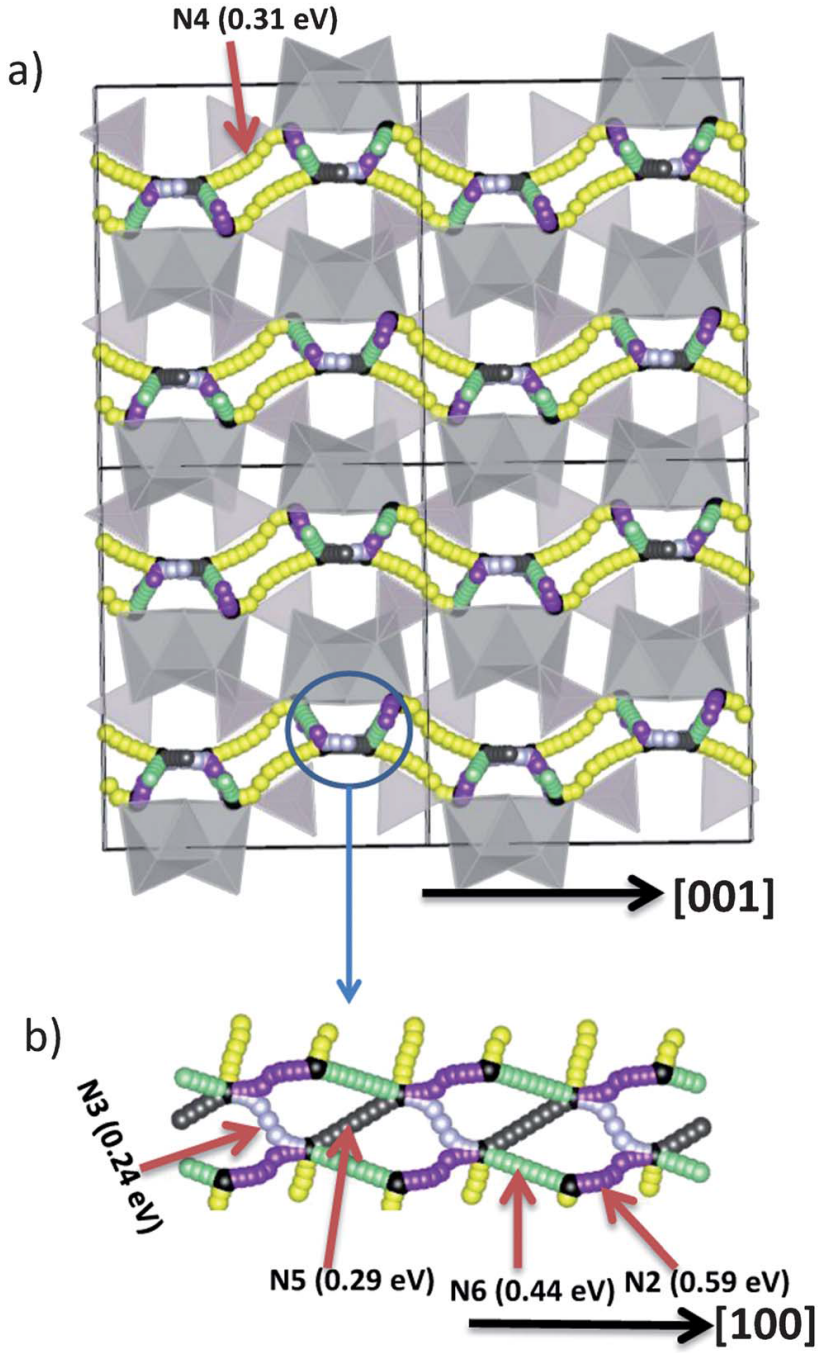

Figure 3-5: *Low energy Na^+ migration pathways in Na_2FePO_4F viewed along (a) the a axis and (b) the b axis. Na sites are in black, FeO_6 octahedra in grey and PO_4 tetrahedra in purple.*

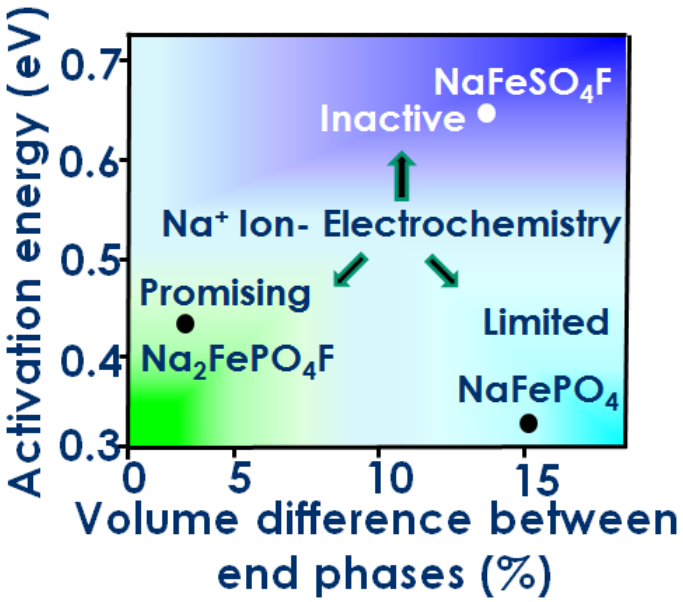

Figure 3-6: *Schematic summary of volume expansion (expt) against migration barrier (calc) for selected Na-ion cathodes and the predicted effect on electrochemical performance.*

Na-de-/intercalation from Na_2FePO_4F has been observed to be much more facile than olivine $NaFePO_4$ (*vide supra*) [43, 176]. Given the similarity in activation energy for migration, this suggests that the volume expansion between the reduced and oxidised phases is a major contributor to determining electrochemical performance of the olivine material. All of these compounds (including tavorite $NaFeSO_4F$, which is almost electrochemically inactive) form a phase boundary between oxidised and reduced phases during charge/discharge which imposes an additional activation energy barrier that corresponds to movement of the phase front in the material. Electrochemical performance is controlled by the amount of strain generated in this phase boundary, as well as by the activation energy barrier (E_a) for ion transport. Strain generated in the phase boundary is proportional to the difference in the unit cell volume (ΔV) of the oxidised and reduced phases which is ~17% for $NaFePO_4$, but only ~3.7% for Na_2FePO_4F. In the case of olivine $NaFePO_4$, it has been recently pointed out that the stress generated by formation of the phase boundary is the root cause for different electrochemical profiles during charge and discharge [128]. For the mixed transition metal phosphate $NaFe_{0.5}Mn_{0.5}PO_4$, it has been reported [175] that no phase boundary is formed upon Na de/-intercalation. However, a very large strain in the material can still be expected

during the charge-discharge process, as there is about a 21% unit cell volume difference between fully oxidised and fully reduced compositions.

A large volume change between the end members also induces very significant polarization during charge and discharge as seen for olivine $NaFePO_4$ [175]. In contrast, polarization is almost absent in the case of carbon coated layered Na_2FePO_4F [176]. At a moderate rate of 0.1 C, the reversible gravimetric capacity of carbon coated olivine $NaFePO_4$ and layered Na_2FePO_4F has been reported to be ∼110 $mAhg^{-1}$ and ∼100 $mAhg^{-1}$ respectively [43, 176]. Capacities obtained after 20 cycles are almost similar for both. This is despite the lower theoretical gravimetric capacity of Na_2FePO_4F than $NaFePO_4$ based on the $Fe^{2+/3+}$ couple. While a direct comparison cannot be made in these cases due to differing carbon content/coating techniques, in general it is well accepted that a minimal volume difference on redox provides better cyclability and lower polarization. This rationalises the trend in the electrochemical performance of the polyanion families that have been studied to date: specifically $NaFeSO_4F$ (E_a = 0.60-0.91 eV, ΔV = 14.3%) < $NaFePO_4$ (E_a = 0.32 eV, ΔV = 15%) < Na_2FePO_4F (E_a = 0.30 eV, ΔV = 3.7%), and summarised in Fig. 3-6.

3.5 Chapter Summary

This chapter has presented atomic scale insights into the defect chemistry, Na diffusion pathways and volume expansion effects of the compositionally similar, yet structurally distinct, Na-ion cathodes Na_2FePO_4F and $NaFePO_4$. The results reveal the following main features:

(a) The simulations show good reproduction of the observed structures of the olivine $NaFePO_4$ and layered Na_2FePO_4F materials that were investigated. The energy for antisite defect formation in olivine $NaFePO_4$ is lower than in $LiFePO_4$, suggesting a higher degree of Na on Fe sites in accordance with the known metastability of the ordered $NaFePO_4$ phases.

(b) Significantly, the activation energy barrier for Na-ion conduction in the $NaFePO_4$ olivine framework along the 1D channels is lower than for Li-ion migration in

$LiFePO_4$. The Na migration barriers in the layered Na_2FePO_4F are equally favourable, indicating high Na mobility through a 2D network in the *ac* plane.

(c) The relationship between ionic transport and electrochemical properties among these materials highlights the crucial importance of the volume expansion-induced strain on de(intercalation). This is generally more substantial for the larger Na^+ vs. the smaller Li^+ ion. In such systems the strain contributes significantly to the overall energy for redox phase transformation, and hence materials which display a large difference in the volume of the end member phases will invariably demonstrate a lower rate capability than similar materials with a reduced volume change difference between end members. Where this is coupled with a high activation energy for Na-ion transport (e.g. $\geq$0.8 eV) extremely poor electrochemical properties can be expected. An example of this detrimental combination can be found in $NaFeSO_4F$, which exhibits almost zero intercalation capacity despite having an open tavorite-like framework that appears favourable for cation migration.

(d) Intermediate volume expansion combined with good ion transport will give rise to better, but often still poor, electrochemical properties. This will be particularly evident in 1D conductors such as $NaFePO_4$, where antisite defects present additional barriers to Na^+ diffusion. Conversely, very promising electrochemical properties should be anticipated for Na- ion materials which demonstrate a low volume change upon cycling with low activation energy barriers to migration, as found in Na_2FePO_4F. However, it must be noted that other properties will also come in to play, particularly the influence of electronic conduction, and the impact of electrolyte compatibility.

Although the interplay of all the above factors is clearly complex and still under investigation, these findings provide guidelines for the future design and synthesis of high rate Na-ion positive electrodes for intercalation batteries.

4 Surfaces and Morphologies of Na_2FePO_4F

'We think there is colour,
we think there is sweet,
we think there is bitter,
but in reality there
are atoms and the void."
Democritus

4.1 Background

As discussed in **Chapter 3**, the compound Na_2FePO_4F, composed of Earth abundant elements with a strong polyanionic framework, has been proposed as a promising Na-ion cathode. Early reports on its electrochemical activity suggested most of the theoretical capacity of 135 $mAhg^{-1}$, could be accessed at reasonable C rates [103, 111]. Furthermore even at higher C rates much of the initial capacity is retained [103, 137]. However, these results apply only to certain nanoparticles of Na_2FePO_4F. Larger particle sizes lead to worse rate performance and significant capacity fade over repeated cycles [103, 111].

An effective method of improving the electrochemical performance of many electrode materials is the reduction of particle size to the sub-micron or nanometre scale. This is thought to be advantageous for several reasons. By decreasing the size of particles,

the distances Na^+ ions and electrons need to diffuse are greatly reduced, allowing more rapid de/intercalation. In addition, nanosizing dramatically increases the relative surface area of the electrode, thereby increasing the electrode-electrolyte interfacial (contact) area. Decreasing crystallite size is also thought to reduce the lattice strain during electrochemical cycling [185].

Modifying the particle morphology of the electrode material is another useful strategy, and is generally achieved by varying the synthesis conditions. Many synthesis methods have been employed in the fabrication of Na_2FePO_4F powders so far, including solid-state [103, 111, 137], hydrothermal [109], spray pyrolysis [108, 136], and sol-gel [138] techniques, leading to a wide range of particle sizes and morphologies. Typically the various approaches produce nanosized granular particles [103, 135, 137], but other morphologies have been synthesised, such as hollow nanospheres [108] and nanorods [103]. Morphological control of nanocrystalline materials can be critical, as many materials properties are crystal size- and shape-dependent. This is particularly true in the case of battery intercalation materials, as recent reports have shown that, through control of the nanoparticle size and morphology, capacity retention can be dramatically improved [108, 135].

Unfortunately, the large variety of synthesis techniques makes it difficult to extract information on the effect of surface features and particle morphologies from experiment alone, as the complex interactions between many factors can mask the fundamental behaviour of the system. Given the importance of surface features and their stabilities, along with particle morphology, an understanding of the atomistic processes governing this behaviour would be valuable.

Here we report a computational study of the surface structures, energetics and redox potentials of Na_2FePO_4F for a large range of surface orientations and terminations. Important surface features are identified and crystal morphologies are predicted from the simulated surfaces. These are compared to experimental structures and some of the processes governing nanoparticle formation are discussed.

4.2 Structural Modelling

Na_2FePO_4F forms a layered structure, crystallising in space group *Pbcn*, with the Fe^{2+} residing on two distinct crystallographic sites both octahedrally coordinated to four O^{2-} and two F^- ions. These octahedra connect to form face-sharing bioctahedra, leading to Fe-F-Fe chains running parallel to the *a* axis. These are connected by corner-sharing PO_4 tetrahedra to form $FePO_4F$ layers parallel to the *ac* plane. The sodium ions reside on two crystallographic sites found within the interlayer spaces, labelled Na1 and Na2 [103]. This structure is illustrated in Figure 4-1.

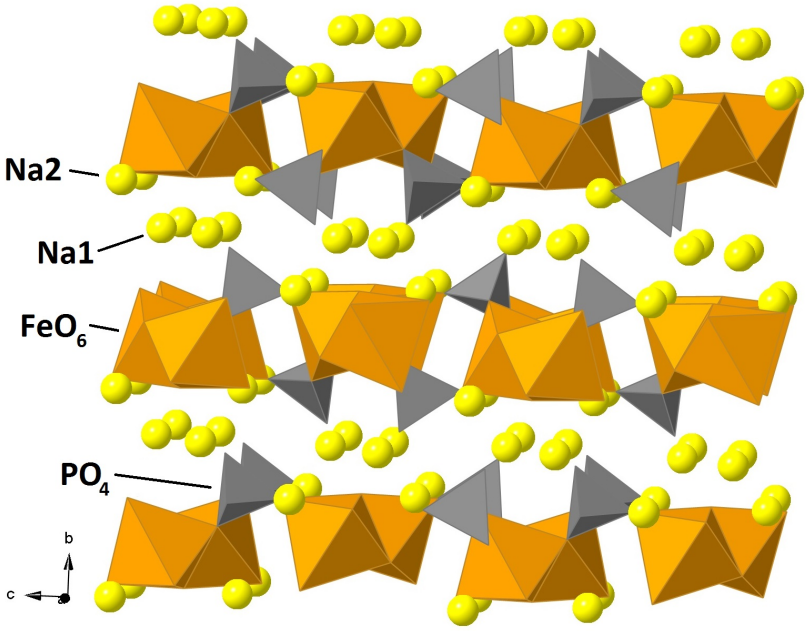

Figure 4-1: *Crystal structure of Na_2FePO_4F with FeO_4F_2 in orange, PO_4 in grey and Na in yellow [103].*

A set of interatomic potentials and shell model parameters have been derived in previous work on Na_2FePO_4F, discussed in **Capter 3**, based on effective Buckingham potentials and a three body O-P-O potential. This model has been shown to reproduce the crystal structure to a high degree of accuracy. A comparison between calculated unit cell parameters and XRD data is shown in Table 4.1, and are used again in this study to calculate surface energies and particle morphologies. It should also be noted that the bond lengths are also well reproduced. The potential parameters and a more

Table 4.1: *Comparison of experimental and calculated structural parameters of Na_2FePO_4F, displaying lattice parameters and mean bond lengths [103].*

Lattice Parameters			
Parameter	**Exptl**	**Calc (Potentials)**	**Calc (DFT)**
a (Å)	5.220	5.231	5.272
b (Å)	13.854	13.847	14.027
c (Å)	11.744	11.779	11.955
α (°)	90.0	90.0	0.0
β (°)	90.0	90.0	0.0
γ (°)	90.0	90.0	0.0
Mean Bond Lengths			
Bond	**Exptl**	**Calc (Potentials)**	**Calc (DFT)**
Na-O (Å)	2.408	2.408	2.446
Na-F (Å)	2.401	2.459	2.439
Fe-O (Å)	2.121	2.090	2.154
Fe-F (Å)	2.134	2.141	2.155
P-O (Å)	1.537	1.547	1.559

in depth discussion of the structural reproduction can be found in **Chapter 3**.

In addition, DFT methods have been employed to study the redox potentials at specific surfaces. These were performed in the VASP code using PAW potentials and the Generalized Gradient Approximation of the PBE functional. A Hubbard U correction of (U_{eff} = U-J = 4.0 eV), which has been shown to give a good description in a variety of other Fe containing battery materials [186–189]. A planewave basis cutoff energy of 800 eV and minimum grid of 3×3×3 k-points was required to adequately converge the forces and energies for the bulk structure. For surface calculations the k-point grid was scaled appropriately and a plane wave cutoff of 500 eV was applied. Furthermore, a minimum slab and vacuum thickness of 20 Å was required to converge the surface energies. Full geometrical relaxation of the ionic positions was performed to incorporate surface relaxation effects. The calculated lattice parameters for the bulk system are given in Table 4.1 and can be seen to be in good agreement with experimental parameters, although the common tendency for PBE+U to slightly overestimate the unit cell volume is apparent.

4.3 Surface Structures and Energies

Surface structures and energies were examined for all dipole-free orientations with a Miller index less than two. In addition all surfaces with indexes higher than two and a d-spacing greater than 3.0 Å were also simulated, giving a total of 21 unique surface orientations. All non-equivalent terminations were considered for each surface orientation and the lowest energy termination taken as the most favourable. Terminating structures were constrained such that they were stoichiometric with zero dipole moment normal to the surface plane. In all cases PO_4 tetrahedra were kept intact. This is a reasonable assumption since breaking the strongly covalent P-O bonds would lead to high energy, unstable structures. All the surfaces constructed are necessarily uneven on the atomic scale due to the large size difference between the PO_4 groups and the metal cations. All potentials based calculations were performed with a 2D periodic model in the GULP code, whilst electronic structure calculations employed a 3D periodic model in the VASP code. Furthermore, as mentioned in **Section 2.5**, it is important to be aware that simulations are performed in a vacuum, whilst experimental conditions will include a wide variety of additional species, along with pressure and temperature effects. Indeed it is well known that such conditions can have a large impact on surface properties. Although their omission places limitations on the interpretation of computational results, these techniques are now widely used in the study of surface features and have demonstrated good agreement with experiment, providing insight into real world phenomena.

The d-spacing, Tasker type, surface energy and attachment energy of all the resultant surfaces are summarised in Table 4.2. All surfaces underwent significant relaxation, with surface energies typically 15-40% lower after relaxation. Furthermore, the ranking of surfaces according to their surface energies also changes upon relaxation, highlighting the importance of incorporating surface relaxation effects when evaluating relative stabilities. As expected, the low-energy terminations generally displayed the lowest changes in surface energy upon relaxation. This is because the smaller the distortion from bulk crystal structure upon cleavage, the smaller the change in internal energy, which gives a low surface energy.

Table 4.2: *Surface energies of Na_2FePO_4F.*

Plane	Surface type	d-spacing, d_{hkl}/Å	Surface energy/J m^{-2}		Attachment energy/Jm^{-2}
			Unrelaxed	Relaxed	
(010)	II	6.92	1.74	1.44	-0.42
(02$\bar{1}$)	II	5.96	2.37	1.87	-0.28
(1$\bar{3}$0)	II	3.47	3.56	2.57	-0.46
(1$\bar{1}$0)	II	4.89	4.11	2.81	-0.47
(1$\bar{2}\bar{2}$)	II	3.40	4.07	2.83	-0.50
(1$\bar{2}\bar{1}$)	II	3.93	4.15	2.93	-0.49
(001)	II	5.87	4.35	2.97	-1.12
(1$\bar{3}$1)	II	3.32	4.37	3.04	-0.51
(1$\bar{1}\bar{2}$)	II	3.76	4.93	3.36	-0.49
(02$\bar{3}$)	II	3.41	5.01	3.43	-0.33
(11$\bar{3}$)	II	3.06	5.27	3.48	-0.68
(01$\bar{1}$)	II	4.48	5.51	3.61	-1.39
(2$\bar{1}\bar{1}$)	II	2.51	5.51	3.62	-0.73
(2$\bar{2}\bar{1}$)	II	2.40	5.50	3.63	-0.66
(10$\bar{2}$)	III	3.91	5.51	3.66	-0.66
(1$\bar{1}\bar{1}$)	II	4.52	5.66	3.69	-0.64
(2$\bar{1}\bar{2}$)	II	2.35	6.42	4.13	-1.00
(10$\bar{1}$)	II	2.39	6.95	4.43	-2.46
(04$\bar{1}$)	II	3.32	9.74	6.04	-1.53
(01$\bar{2}$)	II	2.70	10.07	6.12	-2.46
(100)	II	2.62	15.11	8.94	-6.11

Table 4.2 shows that the vast majority of surfaces examined are of Tasker type II (discussed in **Section 2.5** Fig. 2-9). The only type III surface, (10$\bar{2}$), had its dipole removed by moving two F^- ions from the outermost layer to the opposite side of the crystal slab. The (10$\bar{2}$) surface thus intrinsically contains 50% F^- vacancies at the surface relative to the bulk. Unlike olivine-type $LiFePO_4$ and $NaFePO_4$, where a higher proportion of surfaces are Tasker type III [190, 191], in Na_2FePO_4F the equal numbers of PO_4 tetrahedra and FeO_6 octahedra are aligned opposite to one another within crystal layers in all three crystallographic directions, so that their individual dipole moments cancel out for the majority of low-index crystal orientations considered here.

As can also be seen in Table 4.2, the lowest surface energies are found for (010), $(02\bar{1})$, $(1\bar{3}0)$, $(1\bar{1}0)$ and $(1\bar{2}\bar{2})$ surfaces, whilst the lowest attachment energies are found for $(02\bar{1})$, $(02\bar{3})$, (010), $(1\bar{3}0)$ and $(1\bar{1}0)$. These low energy surfaces are discussed in detail below.

(010) Surface: The (010) surface is the lowest energy surface calculated for Na_2FePO_4F and its relaxed structure is shown in Figure 4-2. The lowest-energy termination corresponds to a cut through an Na channel, leaving an intact $FePO_4F$ layer at the surface containing several Na ions. The outermost moeities comprise Na, PO_4 and F groups, with the Fe groups residing below them and shielded from the vacuum region. Consequently all Fe atoms remain six-coordinated, and displacements from the ideal lattice sites are minimal for all atoms, particularly for those in the polyanion framework. Even though these slight relaxations extend to atoms up to ∼1.4 nm from the outermost layer, representing a relatively thick surface region, overall the energy difference between the unrelaxed and relaxed (010) surfaces remains small, making this surface the most stable of all those examined.

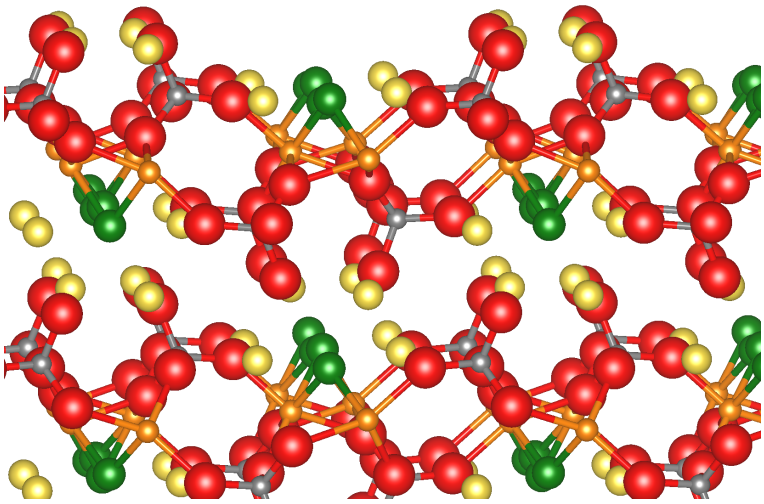

Figure 4-2: *Relaxed structure of the (*010*) surface of Na_2FePO_4F (side view), with Fe in orange, Na in yellow, P in grey, O in red and F in green.*

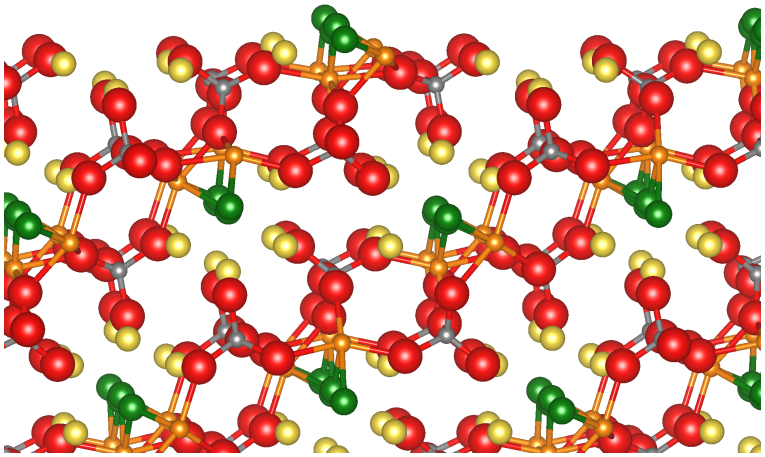

Figure 4-3: *Relaxed structure of the* $(02\bar{1})$ *surface of* Na_2FePO_4F *(side view), with Fe in orange, Na in yellow, P in grey, O in red and F in green.*

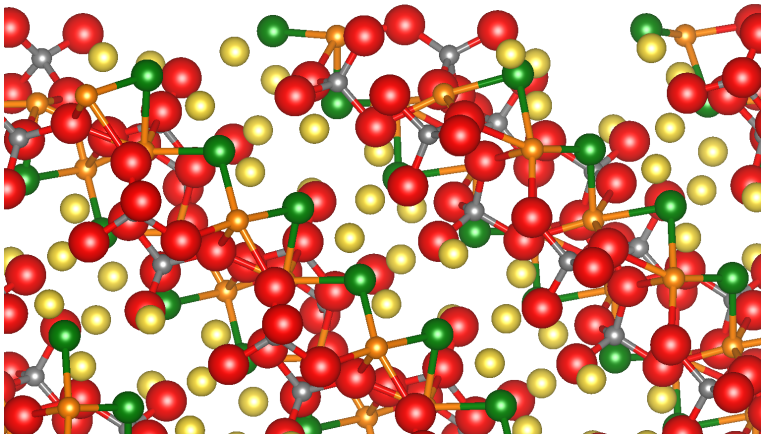

Figure 4-4: *Relaxed structure of the* $(1\bar{3}0)$ *surface of* Na_2FePO_4F *(side view), with Fe in orange, Na in yellow, P in grey, O in red and F in green.*

$(02\bar{1})$ Surface: The $(02\bar{1})$ surface also has a very low surface energy. The outermost layer is stoichiometric and relatively even at the atomic scale, with few outlying atoms, as can be seen in Figure 4-3. Furthermore, Fe ions remain well coordinated, with 50% Fe 6-coordinated and 50% 5-coordinated. The surface relaxation of individual moieties is relatively small, with a slight rotation of the PO_4 groups and displacement of the exposed Na ions ~0.1 Å into the bulk, but the deformed region extends to ~1.2 nm into the crystal. Importantly, unlike the (010) surface, the $(02\bar{1})$ surface does provide access to the Na layers so Na^+ intercalation into the bulk is possible through this surface.

$(1\bar{3}0)$ Surface: As can be seen in Figure 4-4, the $(1\bar{3}0)$ surface is particularly flat at the atomic scale, except where the Na layers protrude, with PO_4 and Fe polyhedra most prominent at the surface termination. Fe is found in both 5-coordinate (75%) and 4-coordinate (25%) environments at the surface. As with the $(0\bar{2}1)$ surface, this surface provides relatively facile access to the Na layers. Furthermore surface relaxation is confined to within just ~1.0 nm from the surface termination, meaning the surface region itself is relatively thin.

$(1\bar{1}0)$ Surface: As a low energy surface the $(1\bar{1}0)$ surface is of particular interest because the Na layers are aligned closer to the surface normal than for any other low energy surface. As such, Na^+ intercalation into this surface should occur most easily. This structure is illustrated in Figure 4-5. At the surface termination, Fe is found in both 5-coordinate and 4-coordinate environments in equal proportion, reflecting a trend whereby the greater the disruption to the 6-coordinate bulk environment of Fe, the greater the surface energy. As with the $(1\bar{3}0)$ surface, atoms ~1.0 nm into the crystal relax away slightly from their bulk positions.

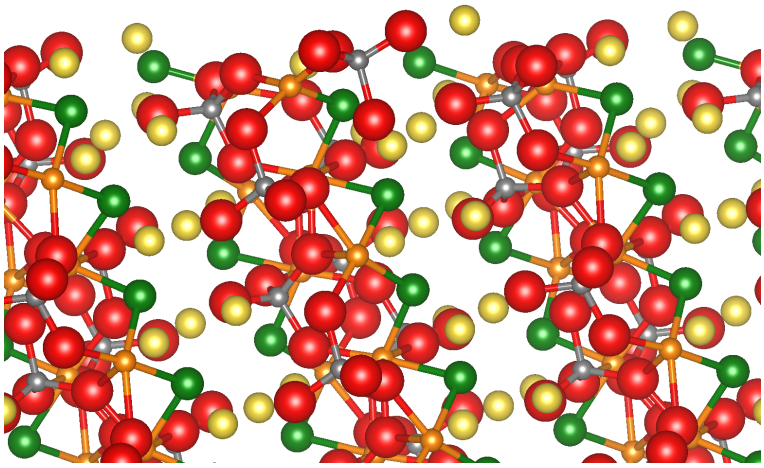

Figure 4-5: *Relaxed structure of the $(1\bar{1}0)$ surface of Na_2FePO_4F (side view), with Fe in orange, Na in yellow, P in grey, O in red and F in green.*

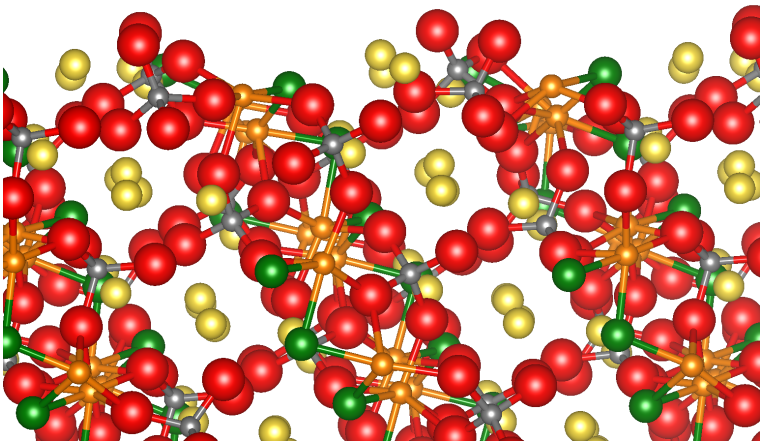

Figure 4-6: *Relaxed structure of the $(1\bar{2}\bar{2})$ surface of Na_2FePO_4F (side view), with Fe in orange, Na in yellow, P in grey, O in red and F in green.*

$(1\bar{2}\bar{2})$ Surface: The $(1\bar{2}\bar{2})$ plane is also close to parallel to the Na layers, although not as close as the $(1\bar{1}0)$ plane. The surface is dominated by PO_4 and Na groups, as can be seen in Figure 4-6, with surface relaxation effects extending ∼1.0 nm into the bulk. Multiple Fe environments exist in the terminating layer, including 4-coordinate, 5-coordinate and 6-coordinate, with 5-coordinate environments accounting for ∼60% of Fe sites in the terminating layer..

4.4 Particle Morphologies

The equilibrium crystal morphology, as calculated from the relaxed surface energies, is shown in Figure 4-7 (a). $\{02\bar{1}\}$, $\{010\}$ and $\{1\bar{2}\bar{2}\}$ surfaces dominate, making up 31.3%, 24.5% and 21.9% of the total surface area respectively. The remaining area is composed of the $\{1\bar{1}0\}$, $\{1\bar{3}0\}$ and $\{001\}$ surfaces, leading to an octagonal-type particle compressed slightly along the [010] direction. This is the morphology that would be expected for small nanoparticles grown under close-to-equilibrium conditions. The prevalence of $\{010\}$ surfaces is undesirable as $\{010\}$ planes run parallel to the Na layers in the bulk Na_2FePO_4F crystal. Previous work has shown interlayer migration possesses a prohibitively high energy barrier, Ea > 2.0 eV and, as such, intercalation of Na^+ into the nanoparticle through a (010) or $(0\bar{1}0)$ face is kinetically restricted [132].

Conversely all other surfaces provide access to the Na^+ layers, with the $\{1\bar{1}0\}$, $\{02\bar{3}\}$ and $\{1\bar{1}\bar{2}\}$ surfaces particularly open, and are likely to play an important role in Na^+ intercalation. It is also worth noting that the equilibrium morphology is similar in some respects to that previously reported for $NaFePO_4$ [191], which has a roughly isotropic hexagonal shape that is also slightly thinner along the [010] direction.

Figure 4-7 (b) shows the calculated growth morphology, which is very different from the equilibrium morphology. Here again $\{02\bar{1}\}$ surfaces are dominant, comprising 47.4% of the total surface area. However, other important surfaces include $(02\bar{3})$, $(1\bar{1}0)$ and $(1\bar{1}\bar{2})$, which are not seen in the equilibrium morphology but make up 20.8%, 18.5% and 10.7% of the total surface area, respectively. $\{1\bar{2}\bar{1}\}$ and $\{1\bar{3}0\}$ surfaces also appear, albeit with small surface areas. Significantly $\{010\}$ surfaces are absent, which has important implications for Na^+ intercalation in this material. All the surfaces present in the growth morphology provide access to the Na layers, suggesting Na^+ intercalation is possible across the entire nanoparticle surface, unlike for the equilibrium morphology, in which only ∼75% of the total surface area provides access to the Na layers. This finding suggests that nanoparticles grown with a kinetically limited synthesis technique may provide better rate performance than those produced under close to equilibrium conditions.

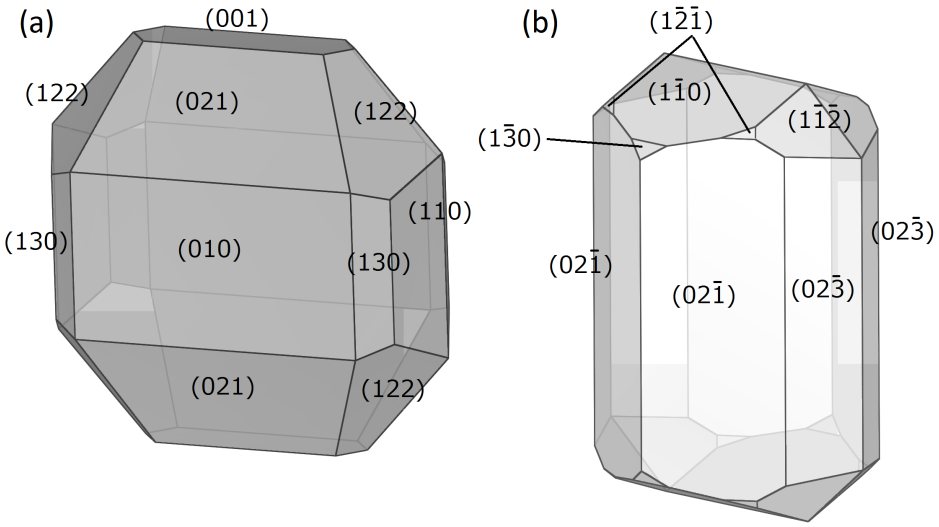

Figure 4-7: *Crystal morphologies of Na_2FePO_4F from calculated surface and attachment energies with (a) the equilibrium morphology and (b) the growth morphology.*

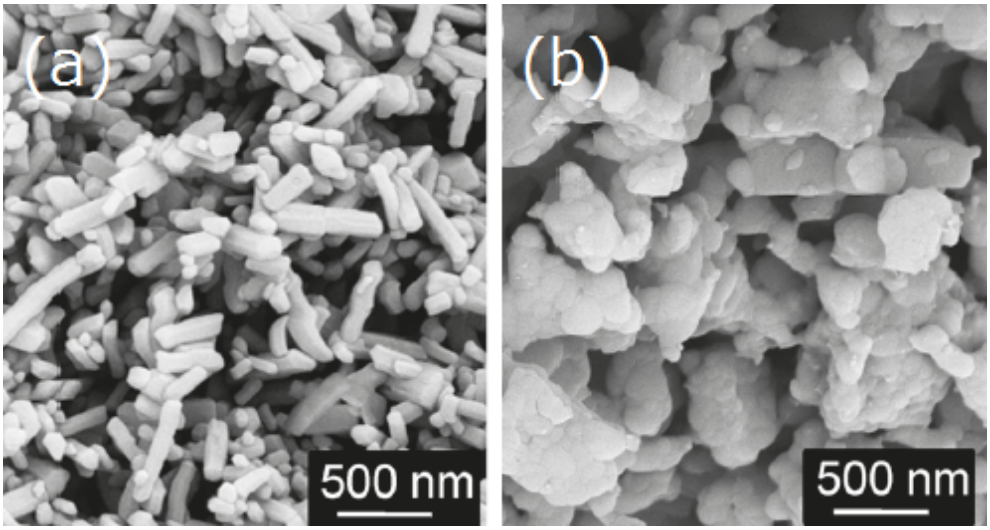

Figure 4-8: *SEM images of nanoparticles of Na_2FePO_4F produced by (a) hydrothermal and (b) sol-gel sythesis techniques [103].*

Ellis et al. have synthesised Na_2FePO_4F through a variety of methods; solid-state and sol-gel routes produced relatively isotropic crystallites, whilst a hydrothermal approach led to a more rod-like morphology compatible with our calculated particle shapes [103, 130]. Scanning electron microscopy (SEM) images of these two different powders are shown in Figure 4-8. Interestingly the rod-like nanoparticles demonstrated greater rate capability than the more isotropic particles, consistent with the expected behaviour of our calculated morphologies [139]. Crystallographic orientations of the surfaces of the nanorods have yet to be reported, but such data would provide a useful means by which the simulation results could be validated.

4.5 Surface Redox Potentials

It is possible to calculate the redox potentials for removal of Na ions from individual surfaces using DFT, particularly those prominent in the predicted morphologies. The extraction of x Na ions from a slab containing y formula units can be described by

$$(Na_2FePO_4F)_y \rightarrow xNa + (Na)_{2y-x}(FePO_4F)_y \tag{4.1}$$

From which the voltage can be calculated as

$$V = -\frac{G[(Na_2FePO_4F)_y - G[(Na)_{2y-x}(FePO_4F)_y]}{x} + \mu(Na) \tag{4.2}$$

Where $G[Y]$ is the Gibbs free energy of slab Y and $\mu(Na)$ is the chemical potential of Na. The Gibbs free energy can be approximated using the ground-state energy. Only the Na in the outermost top (and symmetrically equivalent bottom) layers of each surface slab are removed. As such the calculated voltage refers to the average redox potential of Na^+ insertion/extraction from the terminating layer of a given surface. The same calculation was performed for removal of an Na ion from the crystal bulk for comparison.

Table 4.3: *Calculated surface redox potentials of Na_2FePO_4F.*

Surface Plane	Redox Potential (V)
Bulk	2.91
$(1\bar{3}0)$	2.76
(001)	2.83
$(1\bar{1}\bar{2})$	3.05
$(1\bar{1}0)$	3.10
$(1\bar{2}\bar{2})$	3.14
(010)	3.24
$(02\bar{3})$	3.37
$(02\bar{1})$	3.72

Calculations were performed for the 8 most prominent surfaces in the equilibrium and growth morphologies, and the results are given in Table 4.3. The surface redox potentials vary between 2.76 V and 3.37 V, compared to a value of 2.91 V for extraction from bulk Na_2FePO_4F. Most significantly, the lowest energy potential is found for the $(1\bar{3}0)$ plane (2.76 V). This suggests that upon charging, Na^+ will first be extracted from the $(1\bar{3}0)$ surface, and inserted lastly through the $(1\bar{3}0)$ surface upon discharging. As the (001) surface has a similarly low redox potential (2.83 V) and Na diffusion occurs normal to the surface, extraction is also likely to occur initially through this surface. Moreover, as $\{1\bar{3}0\}$ and $\{001\}$ surfaces provide ready access to the bulk layered structure and display a lower voltage than the bulk, upon discharge a driving potential will exist between the surface and the bulk, encouraging rapid movement of Na^+ into the

particle. Therefore, nanoparticles with these surfaces are expected to display enhanced discharge kinetics. Conversely, the $(0\bar{2}1)$ surface, with the highest calculated voltage of 3.72 V, will have surface Na^+ removed last on charging and added first on discharging. Furthermore, a number of the surfaces demonstrate a higher potential than the bulk, indicating that Na^+ ions are more tightly bound at these surfaces than in the bulk. This may provide an additional barrier to be overcome upon sodium insertion, impacting the discharge kinetics of particles composed of these surfaces, which warrants further investigation.

4.6 Chapter Summary

The surface structures and energetics of the promising Na-ion cathode material Na_2FePO_4F have been investigated using atomistic simulation and DFT techniques. The particle morphologies provide interesting insights into the electrochemical properties of Na_2FePO_4F. The main results are as follows:

(a) All crystal surfaces were found to undergo significant relaxation, with computed surface energies decreasing by ∼15-40% compared to the as-cut structure. Relaxation was smallest for the low energy surfaces (∼15-30%); these surfaces tend to have the highest atom densities and least disruption to Na and Fe coordination environments.

(b) The equilibrium morphology of Na_2FePO_4F is octagonal in appearance, thinner along the [010] direction than the [100] and [001] directions, with (010), $(02\bar{1})$, $(1\bar{2}\bar{2})$ and $(1\bar{1}0)$ surfaces prominent. In contrast, the growth morphology has a more extended rod-like appearance, with $\{02\bar{1}\}$, $\{02\bar{3}\}$, $\{1\bar{1}0\}$ and $\{11\bar{2}\}$ surfaces dominant.

(c) The lowest energy surface, (010), lies parallel to the Na-containing *ac* layers of the orthorhombic crystal. Previous calculations (**Section 3.4**) suggest that interlayer Na^+ intercalation is unfavourable. Hence, the prevalence of {010} surfaces in the equilibrium morphology, and their absence from the growth morphology, suggests nanoparticles synthesised in a kinetically limited regime should demonstrate better

rate performance than those grown under close to equilibrium conditions.

(d) The redox potentials of selected surfaces were also investigated with DFT. Surface redox potentials vary between 2.76 and 3.37 V, compared to a value of 2.91 V for extraction from bulk Na_2FePO_4F. Most significantly, the lowest energy potentials are found for the $(1\bar{3}0)$ and (001) planes, suggesting that upon charging Na^+ will first be extracted from these surfaces, and inserted lastly upon discharging.

5 $Na_4M_3(PO_4)_2P_2O_7$ Mixed Phosphates (M = Fe, Mn, Ni, Co) as High Rate Cathodes: Defects, Na-ion Diffusion and Voltage Trends

"The true delight is in the finding out
rather than in the knowing"
Isaac Asimov

5.1 Background

As discussed in **Chapter 1**, mixed phosphates of the formula $Na_4M_3(PO_4)_2P_2O_7$ (M=Fe, Mn, Ni or Co) have recently been considered as potential cathodes for sodium-ion batteries. The Co system, $Na_4Co_3(PO_4)_2P_2O_7$, has been synthesised through a sol-gel process by Iba et al [122, 192] and shown to reversibly intercalate Na-ions at high voltage (∼4.7 V), with a capacity of ca. 99 $mAhg^{-1}$ extracted at a 0.2 C rate. Furthermore, the material demonstrated excellent rate performance, retaining 89 $mAhg^{-1}$ capacity at 5C rate [122, 192]. The $Na_4Fe_3(PO_4)_2P_2O_7$ material has been studied by Kang et al [24, 139] in combined experimental and DFT studies. A theoretical capacity of 129 $mAhg^{-1}$, delivered at approximately 3.2 V, is highly competitive with other Na-ion cathodes [11]. It has been shown that $Na_4Fe_3(PO_4)_2P_2O_7$ forms a solid solution upon sodium extraction, with a volume change of just 4% upon cycling. This compares favourably with other Na-ion battery materials, such as $NaFePO_4$, $NaFeSO_4F$

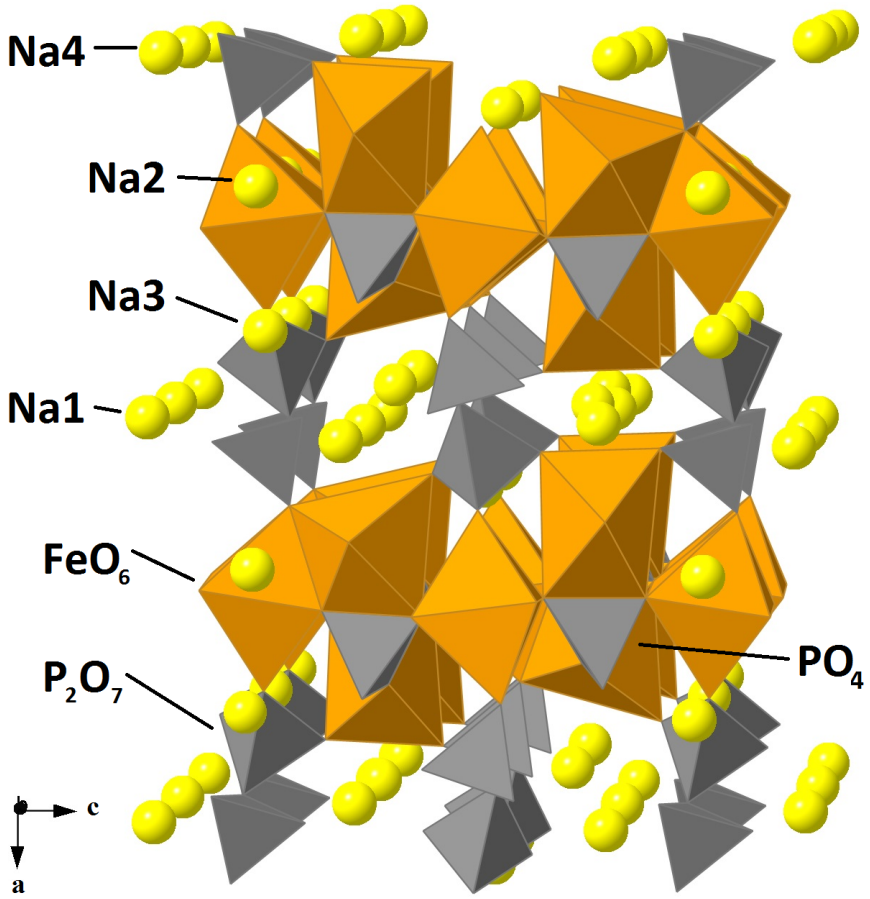

Figure 5-1: *Experimental structure of $Na_4Fe_3(PO_4)_2P_2O_7$, isostructural with the Co, Ni and Mn analogs. The sodium is given in yellow, FeO_6 octahedra in orange and PO_4 tetrahedra in grey [139].*

and $Na_{0.95}Li_{0.15}(Ni_{0.15}Mn_{0.55}Co_{0.1})O_2$ which demonstrate a volume change of 15%, 14.5% and 20% respectively upon cycling [132, 193, 194]. This low volume change is attributed to the P_2O_7 dimers undergoing rotation and distortion to accommodate structural changes [24, 139].

Our focus here is in probing the defect, diffusion and voltage trends of the $Na_4M_3(PO_4)_2P_2O_7$ (M=Fe, Mn, Co, Ni) class of materials. In this study, we have applied a combination of atomistic energy minimization and molecular dynamics methods to examine the processes governing the defect chemistry and ion migration. In addition, we have employed DFT methods to study the trends in cell voltage across a variety of transition metal configurations. This work was published recently [195], (see **Appendix H**).

Table 5.1: *Buckingham potential parameters derived for defect calculations of $Na_4M_3(PO_4)_2P_2O_7$[M = Fe, Mn, Ni and Co] .*

Interaction	A	ρ	C	k	Y
Na-O	2612.00	0.2644	0.0	9999	1.000
P-O	1194.00	0.3385	0.0	9999	5.000
O-O	22764.3	0.1490	44.53	65.00	0.960
Fe-O	1450.00	0.2977	0.0	19.16	-0.997
Mn-O	1068.80	0.3154	0.0	81.20	-1.000
Ni-O	1900.08	0.2800	0.0	2.880	0.000
Co-O	3245.00	0.2644	0.0	110.5	-1.503

5.2 Structural Modelling

The starting point for our simulations is the reproduction of the observed crystal structures. The structures of $Na_4M_3(PO_4)_2P_2O_7$ (where M=Fe, Co, Mn, Ni) all adopt a similar crystal structure with a *Pna2₁* space group [121, 139, 192]. The $Na_4Fe_3(PO_4)_2P_2O_7$ structure is shown in Figure 5-1. The transition metals reside in octahedral sites which are joined by phosphate $(PO_4)^{3-}$ groups to form layers in the *bc* plane. These layers are bridged parallel to the *a* axis by pyrophosphate $(P_2O_7)^{4-}$ groups, forming a 3D framework. The Na^+ ions are found in four non-equivalent sites with Na1 and Na4 residing in two channels in the phosphate framework parallel to the *b* axis. The interatomic potentials for all four systems $Na_4M_3(PO_4)_2P_2O_7$ (where M=Fe, Mn, Ni, Co) were derived simultaneously, which is not trivial for such complex structures. A comparison between the calculated structures based on these effective potentials (Table 5.1) and experimental data is given in Table 5.2.

The calculated unit cell parameters differ from experiment by at most 1.74% and in most cases the deviations are substantially less. The mean deviations in bond lengths are 0.043 Å, 0.085 Å and 0.025 Å for the M-O, P-O and Na-O bonds respectively. The accurate reproduction of all structures, including the iron analogue, with the same interatomic potentials gives us confidence that the model can be used reliably in subsequent defect simulations to explore trends in properties.

To increase the total simulated time, the MD simulations used a variant of the partial

Table 5.2: *Comparison between calculated and experimental structures [121, 139] of $Na_4M_3(PO_4)_2P_2O_7$ using potentials from Table 5.1.*

Cell Parameter/ Bond	M = Fe		M = Mn		M = Ni		M = Co	
	Expt	**Calc**	**Expt**	**Calc**	**Expt**	**Calc**	**Expt**	**Calc**
a (Å)	18.07517	18.17429	17.991	18.304	17.999	18.062	18.046	18.052
b (Å)	6.53238	6.56807	6.648	6.593	6.4986	6.4827	6.533	6.566
c (Å)	10.64760	10.63666	10.765	10.678	10.420	10.510	10.536	10.649
α (°)	90.0	90.0	90.0	90.0	90.0	90.0	90.0	90.0
β (°)	90.0	90.0	90.0	90.0	90.0	90.0	90.0	90.0
γ (°)	90.0	90.0	90.0	90.0	90.0	90.0	90.0	90.0
M-O (Å)	2.145	2.113	2.207	2.137	2.109	2.064	2.134	2.108
P-O (Å)	1.565	1.635	1.558	1.635	1.535	1.635	1.543	1.635
Na-O (Å)	2.513	2.504	2.501	2.455	2.472	2.426	2.457	2.46

Table 5.3: *Potential model developed, for use in MD simulations, based on potentials of Pedone et al [196].*

Interaction	D **(eV)**	α **(Å^2)**	**r (Å)**	**C**	**Y**
Fe-O	0.066171	1.772638	2.658163	2.0	1.2
Mn-O	0.032616	2.719217	2.0255701	3.0	1.2
Na-O	0.023363	1.763867	3.006315	5.0	0.6
P-O	0.831326	2.585833	1.800790	1.0	3.0
O-O	0.042395	1.379316	3.618701	22.0	-1.2

charge potential model of Pedone et al, [196] which has been explicitly developed to allow rapid simulation of finite temperature properties in complex polyanion compounds. Moving from a shell model to the Pedone rigid ion model allows a larger timestep to be used and thus a greater simulation time explored for a given computational expense. The potentials are given in Table 5.3, and the structural reproduction from this model is extremely good (shown in Table 5.4). The structure is reproduced to almost the same degree of accuracy as the model developed for the defect calculations.

Finally, DFT simulations were run to explore the influence of the transition metal species on the average voltage of the material. The PBESol exchange-correlation functional was used along with a Hubbard U correction, with values for $U_{eff}(=U-J)$ of 4.3 eV, 3.9 eV and 6.0 eV for $Fe^{2+/3+}$, $Mn^{2+/3+}$ and $Ni^{2+/3+}$ respectively. These are the mode values used in a selection of DFT studies of similar materials, as categorised

in **Appendix B**, and were found to accurately reproduce known material properties.

Table 5.4: *Comparison of calculated and experimental structures of $Na_4M_3(PO_4)_2P_2O_7$ from Pedone potential model used in MD calculations [121, 139].*

Cell Parameter/Bond Length	M=Fe		M=Mn	
	Expt	**Calc**	**Expt**	**Calc**
a (Å)	18.07517	18.47168	17.991	18.486
b (Å)	6.53238	6.60949	6.648	6.630
c (Å)	10.64760	10.89843	10.765	10.992
α (°)	90.0	90.0	90.0	90.0
β (°)	90.0	90.0	90.0	90.0
γ (°)	90.0	90.0	90.0	90.0
M-O (Å)	2.145	2.216	2.207	2.261
P-O (Å)	1.565	1.518	1.558	1.519
Na-O (Å)	2.513	2.561	2.501	2.525

Table 5.5: *Comparison between calculated and experimental structures of $Na_4Fe_3(PO_4)_2P_2O_7$ from DFT model [121, 139].*

Cell Parameter/Bond Length	M=Fe	
	Expt	**Calc**
a (Å)	18.07517	18.11671
b (Å)	6.53238	6.53176
c (Å)	10.64760	10.64427
α (°)	90.0	90.0
β (°)	90.0	90.0
γ (°)	90.0	90.0
Fe-O (Å)	2.145	2.152
P-O (Å)	1.565	1.555
Na-O (Å)	2.513	2.496

Due to the large size of the unit cell (1257.20 Å^3) the Brillouin zone in reciprocal space is relatively small. As such a k-point mesh of 1×2×2 was adequate to converge the energies and stresses of the cell, whilst a planewave cuttoff of 800 eV was required for adequate convergence. Density of state plots, demonstrating the expected non-metallic behaviour, are contained within **Appendix F**. Furthermore, van der Waals interactions were considered as these have been shown to influence cell voltage in some polyanionic systems [187]. However, for these materials, they were found to have a

negligible effect on calculated voltages, probably due to the paucity of unscreened dispersion interactions. The structural reproduction from these parameters is given in Table 5.5, and can be seen to be highly accurate.

5.3 Intrinsic Defects

To investigate the intrinsic defect chemistry a series of isolated point defect energies (vacancy, interstitial and impurity) were calculated for all four transition metals in $Na_4M_3(PO_4)_2P_2O_7$ (M= Fe, Mn, Ni and Co). Combining the energies of these point defects, energies of formation for Frenkel and Schottky-type disorder can be derived. In Kroger-Vink notation these take the general form:

Na Frenkel

$$Na_{Na}^{\times} \rightarrow V_{Na}' + Na_i^{\bullet} \tag{5.1}$$

M Frenkel

$$M_M^{\times} \rightarrow V_M'' + M_i^{\bullet\bullet} \tag{5.2}$$

O Frenkel

$$O_O^{\times} \rightarrow V_O^{\bullet\bullet} + O_i'' \tag{5.3}$$

Schottky

$$4Na_{Na}^{\times} + 3M_M^{\times} + 4P_P^{\times} + 15O_O^{\times} \rightarrow 4V_{Na}' + 3V_M'' + 4V_P''''' + \tag{5.4}$$

$$15V_O^{\bullet\bullet} + Na_4M_3(PO_4)_2P_2O_7$$

We also examined Na/M "antisite" pair defects involving the exchange of positions of a pair of Na^+ (radius 1.02Å)[16] and M^{2+} (radius Mn=0.83Å, Fe=0.78Å, Co=0.75Å and Ni=0.69Å) [16] ions.

$$M_M^{\times} + Na_{Na}^{\times} \rightarrow Na_M' + M_{Na}^{\bullet} \tag{5.5}$$

Table 5.6: *Intrinsic defect formation energies (in eV) for $Na_4M_3(PO_4)_2P_2O_7$[M=Fe, Mn, Ni and Co].*

Defect Type	Energy (eV)			
	Fe	**Mn**	**Ni**	**Co**
Na Frenkel	1.85	1.97	2.29	1.86
O Frenkel	5.26	5.35	5.90	7.59
P Frenkel	24.11	24.26	24.35	25.43
M Frenkel	5.14	4.80	6.27	6.36
Schottky	102.55	106.54	117.80	111.02
Na_2O Schottky	11.16	11.50	12.48	11.26
MO Schottky	7.10	8.66	10.77	9.76
Antisite	1.19	1.37	1.72	1.44

This type of defect is worth considering as it has been observed in other polyanionic battery systems such as $NaFePO_4$ and Na_2FePO_4F [132]. It has also been predicted to have significant impact on the electrochemical performance of some materials. The defect formation results are listed in Table 5.6 (with isolated point defect energies in **Appendix D**) from which three main points emerge.

Firstly, the high energies associated with M Frenkel, O Frenkel, P Frenkel and Schottky defects (for all transition metals) suggest that such defects are unfavourable. Hence, such disorder is unlikely to exist in significant concentrations in the undoped materials.

Secondly, the most favourable type of intrinsic defect is predicted to be the Na/M antisite pair for all compounds; as has been found in previous computational studies of $LiFePO_4$ and $Li_2FeP_2O_7$ [178, 197]. This prediction has been confirmed in scanning tunneling electron microscope studies of $LiFePO_4$ [198] and may have an impact on electrochemical performance as antisite defects have the potential to "block" sodium-ion migration, especially in 1D Na^+ conductors. In addition, from energetic considerations the concentration of antisite defects would be expected to be greatest in $Na_4Fe_3(PO_4)_2P_2O_7$ and least in $Na_4Ni_3(PO_4)_2P_2O_7$. This trend in antisite defect formation energy (going as Fe<Mn<Co<Ni) can largely be rationalized through considerations of the ionic radii and average metal-oxygen bond lengths. The ionic radius of Na^+ (1.02 Å) is larger than all four transition metal cations, which follow the series Mn>Fe>Co>Ni. Furthermore, the average Na-O bond length (∼2.45Å) is larger than

the transition metal M-O bond lengths, which again follow the series Mn>Fe>Co>Ni. It can be seen that generally the defect formation energy increases as the size mismatch (and difference in metal-oxygen bond lengths) between exchanged cations increases. As such, although other properties (including electronic configuration and polarization effects) will influence antisite formation energy, the trend can largely be accounted for by ionic radii and bond length considerations.

Third, Na Frenkel defects demonstrate a relatively low formation energy suggesting a minor intrinsic population of Na interstitials and vacancies. As with Na/M antisites the population is predicted to be highest in $Na_4Fe_3(PO_4)_2P_2O_7$ and lowest in $Na_4Ni_3(PO_4)_2P_2O_7$. The relative ranking of defect energies, with Na/Fe antisites and Na Frenkels being the most stable, is consistent with both phosphate and pyrophosphate materials such as $NaFePO_4$, Na_2FePO_4F and $Na_2FeP_2O_7$ [132, 199].

5.4 Na-ion Migration

Sodium diffusion properties are of vital interest when examining electrode kinetics. Our MD simulations focused on the Fe and Mn based materials, as these two are of greatest practical interest because of their high natural abundance. Simulations over significant timescales and various operating temperatures have been conducted for the compositions $Na_{3.8}M_3(PO_4)_2P_2O_7$ for (M = Fe, Mn). MD simulations over ∼750 ps to ∼1.2 ns and at various temperatures were conducted with a large total simulation cell size (∼25,000 ions) and long equilibration time (∼500ps).

Initially, the mean square displacements (MSDs), $<[r(t)]^2>$, of Na^+ ions were resolved (Examples of which are shown in Figure 5-2) and then used derive Na-ion diffusion coefficients (D_{Na}) from the relation:

$$D = \frac{1}{6}\frac{d < [r(t)]^2 >}{dt} \tag{5.6}$$

yielding D_{Na} values of 6.1×10^{-11} cm^2s^{-1} and 3.1×10^{-10} cm^2s^{-1} at 325 K for the Fe

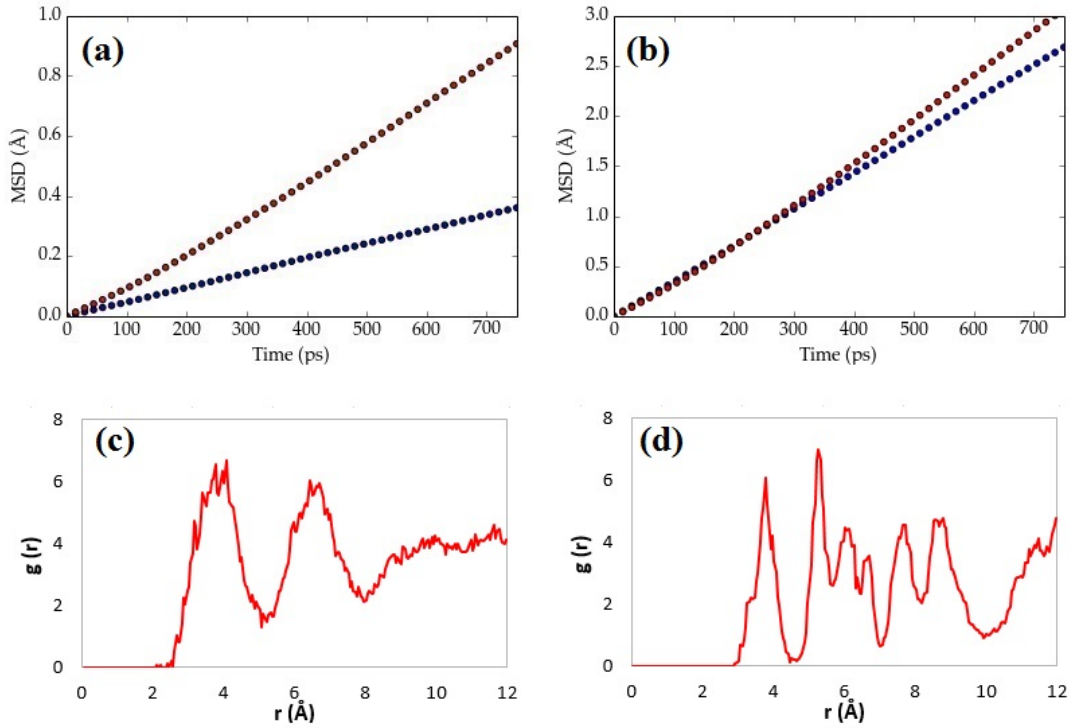

Figure 5-2: *Mean square displacement (MSD) plots of Na-ion diffusion in $Na_{3.8}M_3(PO_4)_2P_2O_7$ for M=Fe (blue) and M=Mn (red) at (a) 625 K and (b) 1225K. Radial distribution function (RDF) plots of $Na_{3.8}Fe_3(PO_4)_2P_2O_7$ from a single timestep at 325K for (a) Na-Na and (b) Fe-Fe ion pairs.*

and Mn materials respectively. Although no experimentally measured diffusion data are available for direct comparison, these values compare well to other Na-ion cathodes; these include layered oxides Na_xMnO_2 (10^{-11} cm^2s^{-1}) [200] and polyanionic materials such as $Na_3V_2(PO_4)_2F$ (10^{-10} cm^2s^{-1}) [201]. See **Appendix C** for a selection of Na diffusion coefficients from the published literature. Our diffusion data can also be used to estimate activation barriers (E_a) of Na-ion migration from an Arrhenius plot (lnD vs $1/T$), shown in Figure 5-3. A diffusion barrier of 0.2-0.24 eV is predicted for the two materials, indicative of fast Na-ion mobility and high rate performance in the polyanion framework. Comparable activation barriers between Li and Na-ion cathodes have been found in various materials, [24, 132, 177, 199] despite the larger ionic radius of Na^+ ion (1.02 Å) compared to the Li^+ ion (0.76 Å) [16]. This is typically rationalised by the tendency of sodium to form longer Na-O bonds, providing a more open framework structure, coupled with polarizability differences arising from the contrast between the highly polarizing Li^+ cation and the less polarizing Na^+. Furthermore, it is worth

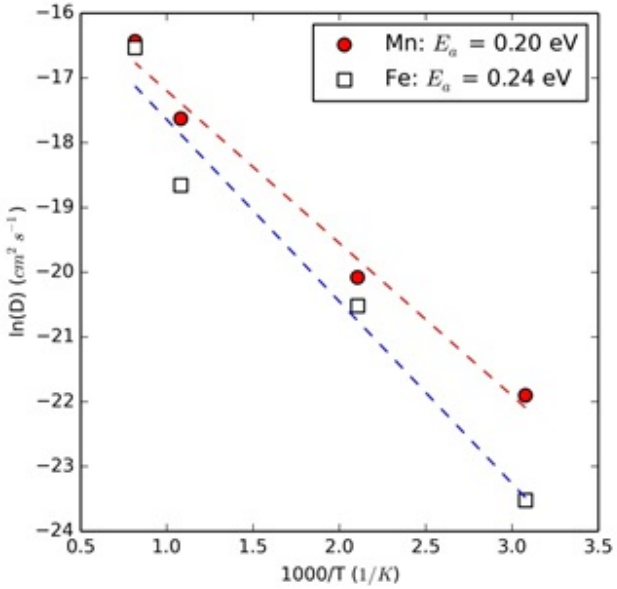

Figure 5-3: *Arrhenius plot for Na ion diffusion in $Na_{3.8}Fe_3(PO_4)_2P_2O_7$ and $Na_{3.8}Mn_3(PO_4)_2P_2O_7$.*

stressing that the activation energy of 0.2-0.24 eV is found to be the same for all Na sites, suggesting from energetic considerations alone that all Na sites should be equally accessible under cycling. It must be noted that previous DFT analysis [24] of the Fe material found a higher activation barrier (∼0.5 eV), although this was determined from nudged elastic band (NEB) calculations for a single migrating Na-ion.

A useful means of visualizing diffusion trajectories is plotting accumulated Na-ion densities, which indicates the lattice sites most frequently traversed over the course of the simulation run. These plots are shown in Figure 5-4 for the Fe system; we note that the same behaviour is found for the Mn-based material. The broad distribution and significant overlap of Na-ion densities demonstrates the highly mobile nature of Na-ions in this material involving all Na sites. This diffusion extends over a 3D network throughout the material, in which *b*-axis channels (containing sites Na1 and Na4) are connected by intralayer migration through Na2 and Na3 sites. Within this context, the low antisite defect energy is likely to have less of an impact than would be expected in the case of 1D diffusion where it would block the 1D channel. The 3D network and low activation barriers, as well as the low volume change upon cycling, are promising features for good rate capability of these cathodes.

Closer analysis indicates that the topology of the migration paths varies throughout the diffusion network. The pathways involving only Na2 and Na3 are essentially linear, i.e. span a shortest path trajectory, as can be seen in Fig 5-4 (a). Conversely, for diffusion involving Na1-Na1 and Na4-Na4 paths down the *b*-axis channels, a curved trajectory is found, which provide the lowest energy pathways, as shown in Fig 5-4 (b). Such curved trajectories have also been observed in other polyanion materials, such as $NaFePO_4$ [132]. The trajectories for Na-ion diffusion are largely consistent with previous DFT analysis of the Fe material [24]. The complex 3D network and low activation barriers, with low volume change upon cycling, are promising for good rate capability of these cathodes, as explained in **Chapter 3**.

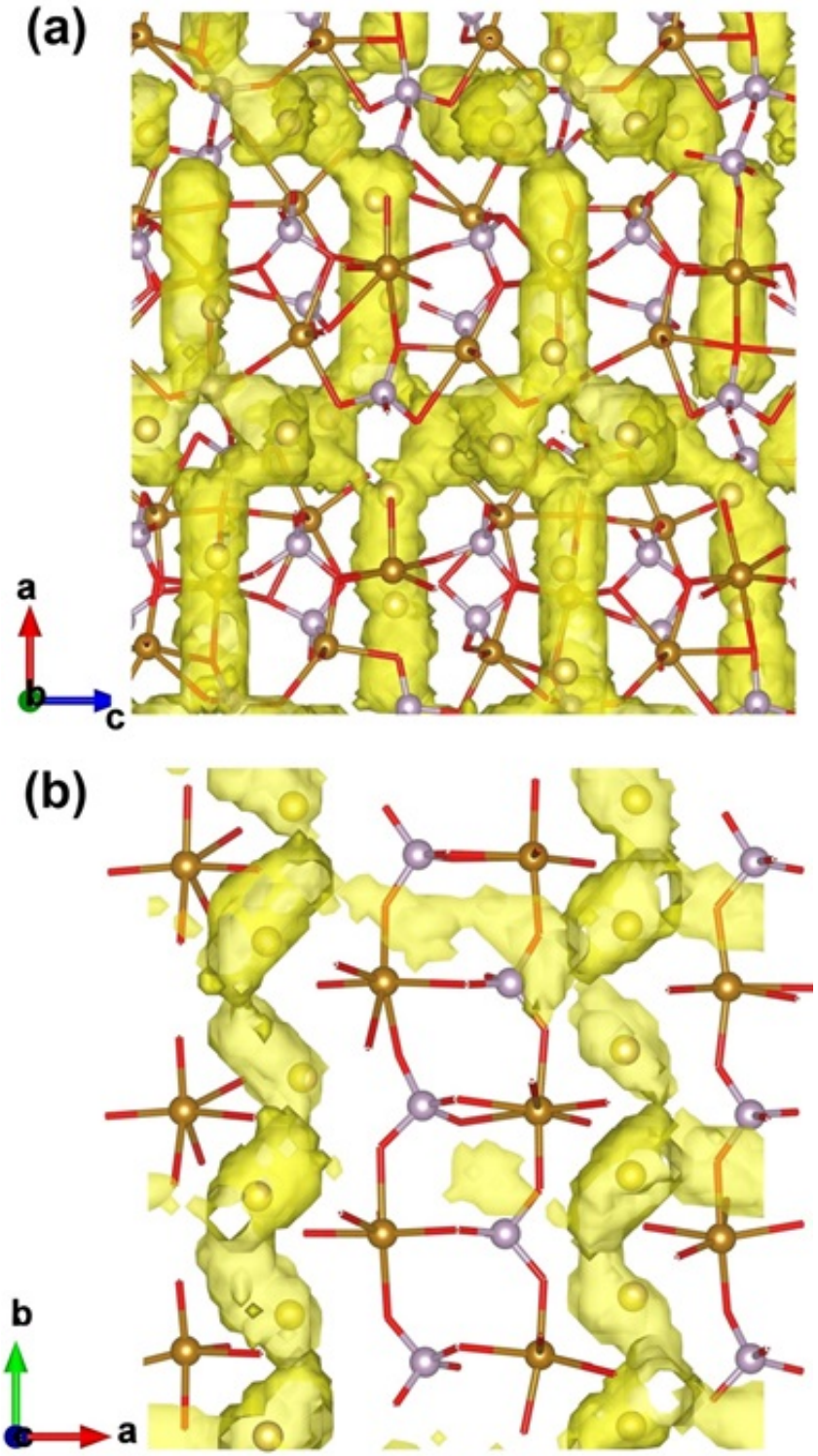

Figure 5-4: *Na-ion density plots for $Na_{3.8}Fe_3(PO_4)_2P_2O_7$ overlayed on initial lattice sites. Lattice sites are given by spheres of Na=yellow, Fe=brown, P=grey and O=red; yellow details Na-ion migration pathways. (a) demonstrates 3D network with ac plane view and (b) close-up view showing the curved paths along the c axis channels.*

5.5 Voltage Trends

Tailoring the cell voltage is key to achieving optimal battery performance and maximizing energy density. DFT calculations were thus used to explore transition metal doping of the $Na_4Fe_3(PO_4)_2P_2O_7$ material and its influence on the cell voltage. To calculate the cell voltage the relevant sodium ions are removed from the structure, which is subsequently energy minimised to determine the most stable structure. Numerous vacancy configurations were tested, based on the results of both screening using potentials-based simulations and previous DFT studies [139]. The voltage was extracted from the lowest energy configurations using the equation,

$$V = \frac{\epsilon[Na_4M_3(PO_4)_2P_2O_7] - \epsilon[Na_xM_3(PO_4)_2P_2O_7] - (4-x)\mu[Na]}{4-x} \tag{5.7}$$

where $\epsilon[Y]$ is the total energy of composition Y and x is the number of sodium atoms remaining per formula unit, taken as $x = 1$ to produce the end member $NaM_3(PO_4)_2P_2O_7$. The chemical potential of sodium, $\mu[Na]$, was calculated using metallic sodium, which is standard practice for cell voltage calculations. Numerous vacancy configurations were tested based on the results of both atomistic potentials screening and previous DFT studies [139]. The cell voltage for $Na_4Fe_3(PO_4)_2P_2O_7$ is calculated to be 3.0 eV vs Na/Na^+, in good agreement with the experimental value of 3.2 V vs Na/Na^+ [139]. The voltage, and energy density, of $Na_4Fe_3(PO_4)_2P_2O_7$ would generally be considered too low for optimal battery performance. Therefore, to raise the calculated voltage, doping with Mn and Ni has been explored, as both cations typically display higher voltages than Fe containing materials.

The trend in voltage across transition metal compositions is detailed in Figure 5-5 as a function of Fe content. The transition metal end members ($Na_4Fe_3(PO_4)_2P_2O_7$, $Na_4Mn_3(PO_4)_2P_2O_7$ and $Na_4Ni_3(PO_4)_2P_2O_7$) follow the series Fe (3.0 V) <Mn (3.5 V) <Ni (4.9 V); this trend is consistent with other battery material series such as $LiMPO_4$[202, 203], $Li_2MP_2O_7$ [204] and Na_2MPO_4F [138], which are known experimentally to follow a similar pattern. In addition, the voltage of the Ni end member (4.9 eV) is outside the stability window of standard electrolytes. Whilst the voltage of

the Mn material is more attractive, Mn-based phosphates often experience problems with redox cycling, typically on account of Jahn-Teller effects.

Compositions of $Na_4Fe_{3-x}Mn_x(PO_4)_2P_2O_7$ (for x=1,2) are calculated to have a voltage of 3.2 V, suggesting Mn doping provides a relatively minor increase in cell voltage and energy density. Conversely, Ni doping is predicted to deliver a significant increase in cell voltage, providing a high degree of voltage control through varying the doping concentration. Furthermore, the composition $Na_4Fe_2Ni(PO_4)_2P_2O_7$ is predicted to have a cell voltage of 3.7 V, close to the upper limit on voltage set by typical electrolyte stability windows. Therefore, we predict that doping $Na_4Fe_3(PO_4)_2P_2O_7$ with a relatively modest level of Ni would lead to a ∼25% enhancement in voltage; this is a significant increase to a viable voltage in terms of energy density and electrolyte stability.

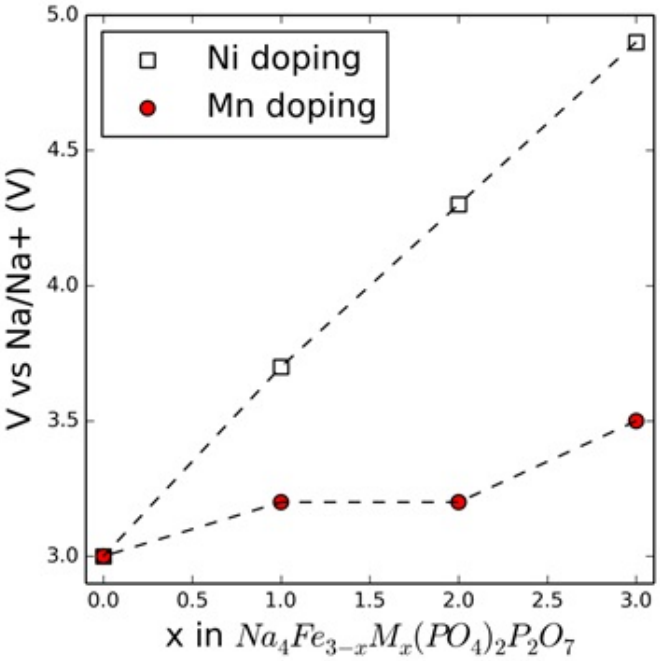

Figure 5-5: *The trend in voltage as Mn and Ni are doped onto the Fe site in* $Na_4Fe_3(PO_4)_2P_2O_7$.

5.6 Chapter Summary

A combination of atomistic energy minimisation, molecular dynamics (MD) and DFT simulation techniques have been used to provide insight into the defect chemistry, Na-

ion diffusion and voltage trends in the Na-ion cathode materials $Na_4M_3(PO_4)_2P_2O_7$ [M = Fe, Mn, Ni, Co].

(a) First, our atomistic potential model provides an accurate reproduction of the complex structures for all four compositions. In all materials the most favourable intrinsic defect is found to be the Na/M antisite pair.

(b) Large-scale MD simulations allowed us to explore Na-ion diffusion kinetics and transport mechanisms. Na^+ diffusion coefficients (D_{Na}) are of the order $10^{-10} - 10^{-11} cm^2 s^{-1}$ at 325 K and activation barriers are found to be 0.20-0.24 eV in the Fe- and Mn-based materials. These values compare favourably to successful Li-ion cathodes indicating rapid Na-ion transport which, coupled with the small volume change observed on cycling, suggests high rate capability and good cycle life. In addition, the MD trajectories suggest a 3D network of migration pathways, with all sodium ions diffusing. Closer analysis indicates that all pathways involving Na2 and Na3 sites are essentially linear, whilst for diffusion down the *b*-axis channels (Na1 and Na4 sites) curved trajectories are found.

(c) Finally, DFT methods have been used to explore voltage trends. The experimental voltage of $Na_4Fe_3(PO_4)_2P_2O_7$ is reproduced and higher cell voltages for $Na_4Mn_3(PO_4)_2P_2O_7$ and $Na_4Ni_3(PO_4)_2P_2O_7$ are predicted. Moreover, we demonstrated that doping $Na_4Fe_3(PO_4)_2P_2O_7$ with Ni can lead to a significant increase in voltage.

These results will assist in developing strategies for optimizing these novel phosphates as possible high-rate Na-ion cathodes, especially for the more cost-sensitive stationary storage sector.

6 Surface Structures and Morphologies of K^+-stabilised α-MnO_2

"Nature composes some of her loveliest poems
for the microscope and the telescope."
Theodore Roszak

6.1 Background

MnO_2 exists as a large number of polymorphs, many of which have been studied as Li-ion or Na-ion intercalation hosts, as discussed in **Chapter 1**. One of the most studied is hollandite α-MnO_2 which contains large channels running throughout the structure facilitating ion diffusion. However, in Li-ion cells bulk α-MnO_2 has struggled with poor capacity retention over many cycles. In mitigation both cation inclusion and nanosizing have been shown to alleviate capacity fade. Given the improvements in cycle life afforded by cation doping and synthesis control this approach has received considerable interest [11, 80–83].

Controlled synthesis is necessary to produce tunnel-based nanostructures with various tunnel sizes, morphologies and atomic ordering. However, this process is not fully understood and requires fundamental understanding of the surface structures and particle shapes on the nanoscale. The growth process of α-MnO_2 is believed to be dominated by an oriented attachment (OA) mechanism where the one-dimensional nanostructure forms by the oriented self-assembly of primary nanoparticles [205–207]. The driving

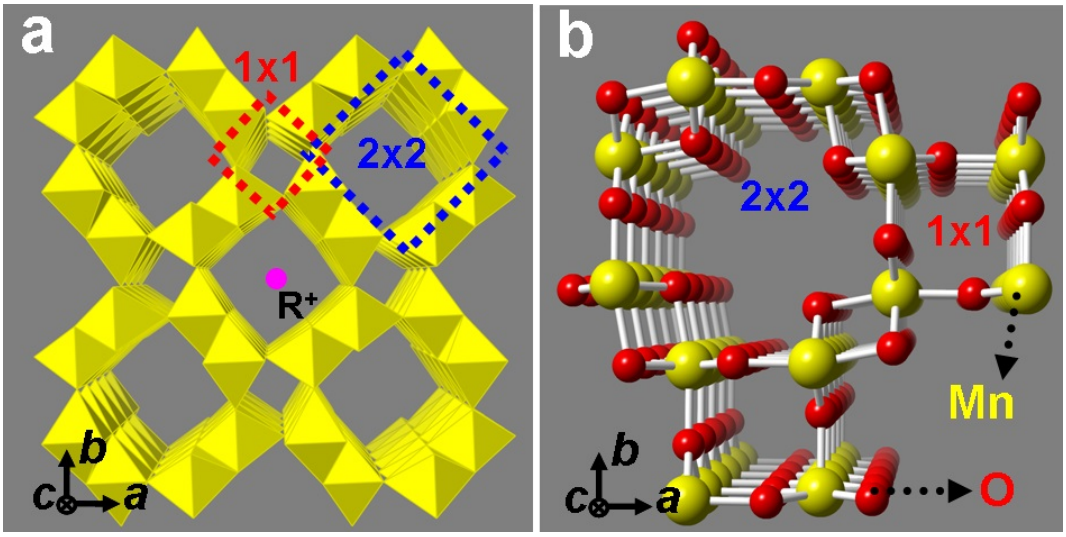

Figure 6-1: *Crystal structures of α-MnO_2. (a) [MnO_6] octahedra model (b) atomic model viewed along [001] (c-axis). The 2×2 and 1×1 tunnels are indicated by blue and red dashed squares, respectively, in (a); The typical definition of a tunnel is based on the number of [MnO_6] octahedra in each tunnel wall. R^+ indicates the position of 2×2 tunnel stabilisers such as NH_4^+, Ba_2^+, and K^+.*

force for the self-assembly is thought to be the reduction of the surface energy when primary particles attach together [208]. Understanding the atomic structure of tunnel-based materials is crucial for designing nanomaterials for desired applications.

α-MnO_2 represents an important family of tunnel-based structures with well-aligned 2×2 (4.6 Å × 4.6 Å) and 1×1 (1.9 Å × 1.9 Å) tunnels [209], shown as both polyhedral and atomic models of α-MnO_2 in Figure 6-1. The larger 2×2 tunnels are generally stabilised by various cations, such as NH_4^+, Ba^{2+}, and K^+[205]. Here, K^+-stabilised α-MnO_2 nanowires were investigated to understand their tunnel-based structures during growth. The morphology evolution of α-MnO_2 nanowires in aqueous solution environment was observed using liquid cell transmission electron microscopy (TEM), and sub-angstrom imaging of the tunnelled interfaces was obtained using aberration-corrected scanning TEM (AC-STEM). This microscopy and nanowire growth work was carried out by collaborators Yifei Yuan and Reza Shahbazian-Yassar at Michigan Technological University. The structural characterization was complemented by *ab initio* calculations to elucidate the surface energetics of K^+-stabilised α-MnO_2. Although Li^+ insertion into β-MnO_2 or α-MnO_2 has been studied by both interatomic potentials[210–212] and DFT methods[88, 213–215], to our knowledge, this work gives the first computational

insights into K^+-stabilised α-MnO_2, allied to high resolution electron microscopy.

6.2 Computational and Structural Modelling

The *ab initio* calculations were performed in the VASP code with PAW potentials. The Generalized Gradient Approximation (GGA) of PBE was applied with Hubbard U corrections (U_{eff} = *U*-*J* = 5.2 eV), which has been demonstrated to give a good description of Li-ion insertion, surface energies and electronic structure of α-MnO_2 [88]. A planewave basis set cut off energy of 520 eV and a minimum grid of 3×3×7 k-points was used in the Brillouin zone for bulk calculations and scaled appropriately for surface simulations.

To assist in determining the atomic-scale structure, we performed DFT calculations on the α-$K_{0.25}MnO_2$ bulk system with K^+ ions on either the Wyckoff 2a (0, 0, 0) or 2b (0, 0, $\frac{1}{2}$) sites, as illustrated in Figure 6-2(a). From these simulations the 2a site was found to be at least 300 meV lower in energy than the off-centre 2b site. This difference is significantly greater than the thermal energy at room temperature (k_BT $\sim$ 26 meV), which suggests that the K^+ ions will reside in the central 2a site. This is in good agreement with the structural observations.

Table 6.1: *Comparison of experimental [216] and calculated structural parameters of α-MnO_2 and α-$K_{0.25}MnO_2$.*

Parameter/ Å	**MnO_2**		**$K_{0.25}MnO_2$**	
	Exptl	**Calc**	**Exptl**	**Calc**
a	9.788	9.923	9.866	9.990
b	9.788	9.923	9.866	9.955
c	2.865	2.941	2.857	3.022
Mn-O	1.906	1.938	1.915	1.968

The calculated lattice parameters for α-$K_{0.25}MnO_2$ with this configuration agree well with experiment, as displayed in Table 6.1, although the common tendency for PBE+U to slightly overestimate the unit cell volume is apparent.

Surface energies are calculated based upon slabs with a minimum thickness of ∼20 Å,

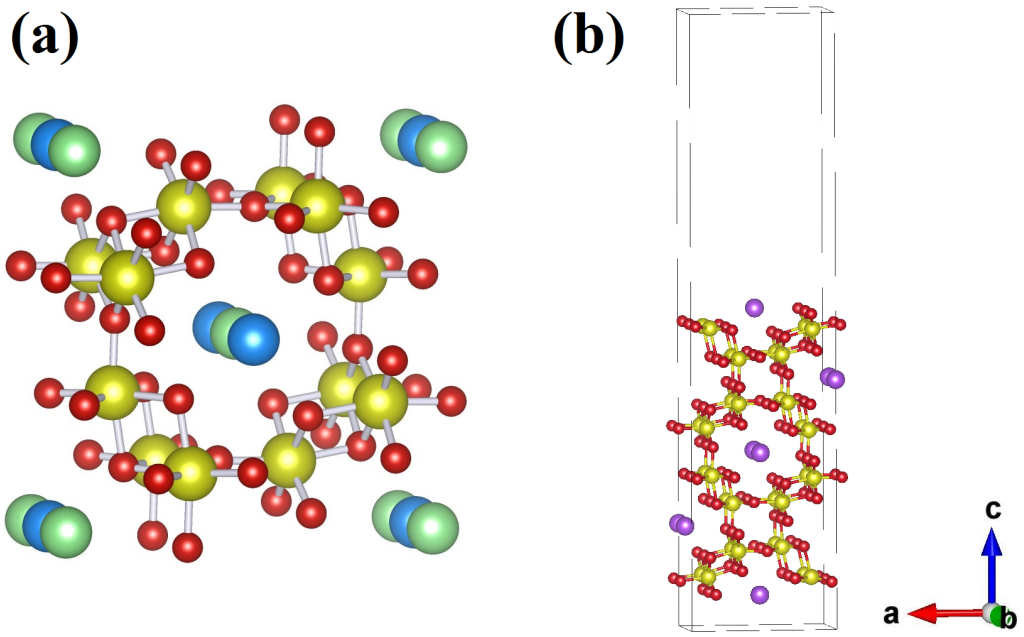

Figure 6-2: *(a) Bulk structure of α-$K_{0.25}MnO_2$ with Mn in yellow and O in red. The Wyckoff 2a sites are shown in green, the 2b sites in blue. (b) Simulation cell for the {100} surface of K^+-stabilised α-MnO_2; with O in red, Mn in yellow and K in purple.*

with slab thickness converged against surface energy. A typical surface cell, set up using the 3D periodic methodology described in **Chapter 2 (Section 2.5)**, is shown in Figure 6-2(b). Full geometrical relaxation of the ionic positions was performed to incorporate surface relaxation effects.

6.3 Surface Energies and Morphologies

In Table 6.2 the surface energies for α-$K_{0.25}MnO_2$ are listed. The lowest energy surfaces correspond to the {100}, {110} and {211} planes; with the {100} surface considerably lower in energy than all other terminations. This is consistent with TEM and HAADF (high angular annular dark field) measurements of K^+-stabilised α-MnO_2, as seen in Figure 6-3, in which the {100} surface is observed to be the most prevalent. In addition, the {110} surface is sufficiently favourable that it could be expected to be expressed in the nanostructures, in agreement with the experimental morphology where it appears as the interface between primary nanowires, as shown is Fig. 6-3(d).

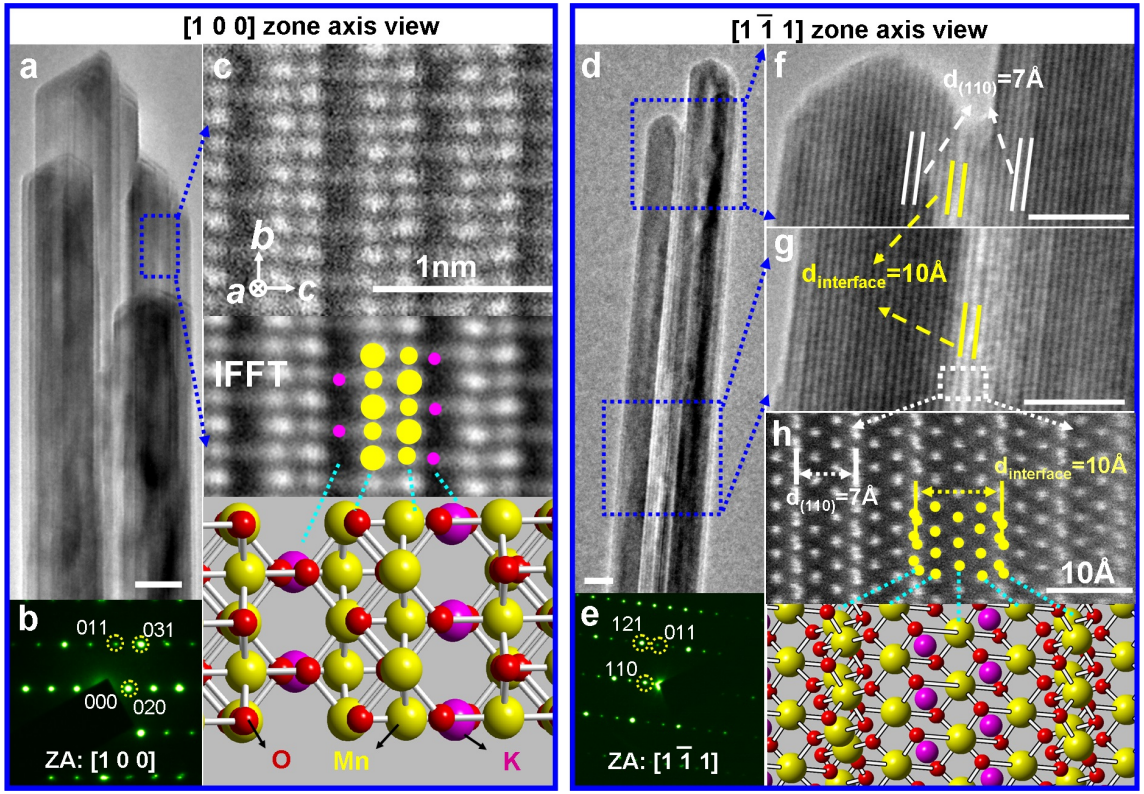

Figure 6-3: *Microscopy image of α-$K_{0.25}MnO_2$ nanorods (from Shahbazian-Yassar et al [217]): (a) A TEM image of secondary α-MnO_2 nanowires taken along [100]; (b) SAED pattern of the same region as (a); (c) A HAADF image of the blue-framed region of a primary nanowire in (a); the corresponding IFFT is given in the middle with the atomic model illustrated at the bottom, where yellow dots represent Mn, red O and pink K^+; the signal of K^+ during HAADF imaging is weaker than that of Mn due to its smaller atomic weight; (d) A TEM image of another secondary α-MnO_2 nanowire taken along [1$\bar{1}$1], where the {110} interface can be directly imaged; (e) SAED pattern of the same nanowire in (d); (f, g,h) HRTEM images and atomic model of the OA-induced interface from the terminated and centre parts of the nanowire,*

Table 6.2: *Calculated surface energies for α-$K_{0.25}MnO_2$ from DFT.*

Plane	**Surface Energy (Jm^{-2})**
(100)	0.44
(110)	0.74
(211)	0.78
(210)	1.14
(001)	1.17
(101)	1.17
(201)	1.19
(111)	1.35

The complete list of surface energies can be used to generate an equilibrium morphology Wulff plot, which is displayed in Figure 6-4 alongside an experimental image of an α-$K_{0.25}MnO_2$ primary nanowire. Given the exceptionally low energy of the (100) surface it is not surprising that it comes to dominate the equilibrium morphology, leading to a square-like cross sectional area for the morphology, in agreement with experiment. Furthermore, the capping surface to the nanowires is expected to be the (211) surface, forming a sloping capping structure. As can be seen in Figure 6-4 this compares well with the SEM and HAADF images. This result combined with the prevalence of the other low energy surfaces (the (110) surface, observed particularly at the primary nanowire interfaces) and in conjunction with the attachment mechanism proposed below suggests that the growth mechanism of α-$K_{0.25}MnO_2$ nanowires is close to an equilibrium process.

We now turn to the edge structure of the low energy surfaces {100} and {110}, in an attempt to understand how the fundamental characteristics of the exposed surfaces in solution drive the formation of 2×3 tunnel-based {110} interfaces. The structure of a (100) surface obtained from HAADF imaging is shown in Figure 6-5(a), with the atomistic relaxed surface from DFT calculations given for comparison in Figure 6-5(b). It can be seen that the (100) surface is essentially composed of a series of intact 2×2 tunnels with a bisected 2×2 tunnel sitting between the intact tunnels, agreeing well with the simulated structure. There is little calculated distortion between the

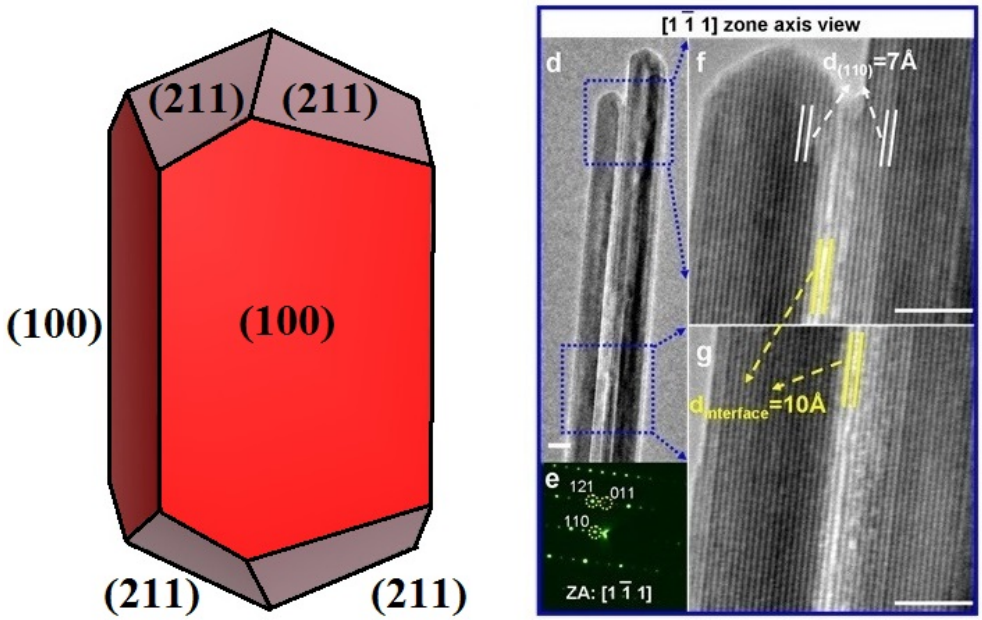

Figure 6-4: *Calculated equilibrium morphology of α-$K_{0.25}MnO_2$ alongside microscopy images of nanowire morphology.*

unrelaxed and relaxed surfaces for this cleavage plane. In addition, Figure 6-5(b) indicates that the Mn ions in the surface region remain well coordinated with 75% in 6-fold coordination, identical to Mn ions in the bulk. The remaining 25% of Mn ions have 5-fold coordination and are unsaturated. In addition, half of the surface K^+ ions reside within intact 2×2 tunnels in their preferred 8-fold coordination (as found in the bulk structure), with the other half in a reduced 4-fold coordination. These structural features are likely to account for the low surface energies calculated for the {100} surfaces, and suggest that such {100} surfaces will be stable during the growth process. The fact that the {100} surface is covered by 2×2 tunnels instead of 1×1 tunnels is important for the improvement in performance of α-MnO_2 nanostructured materials. The direct exposure of large 2×2 tunnels is likely to reduce the distance and energy barrier for ion diffusion, improving the rate performance of α-MnO_2 in applications such as rechargeable battery electrodes [217–220], supercapacitors [221–223] and Li-O_2 battery catalysts [224–227]. Indeed, future generations of these energy storage technologies will depend crucially on new nanostructured materials.

The structure of a (110) surface before the OA process begins can be seen in the HAADF image in Figure 6-5(c). The simulated atomistic structure of the same surface

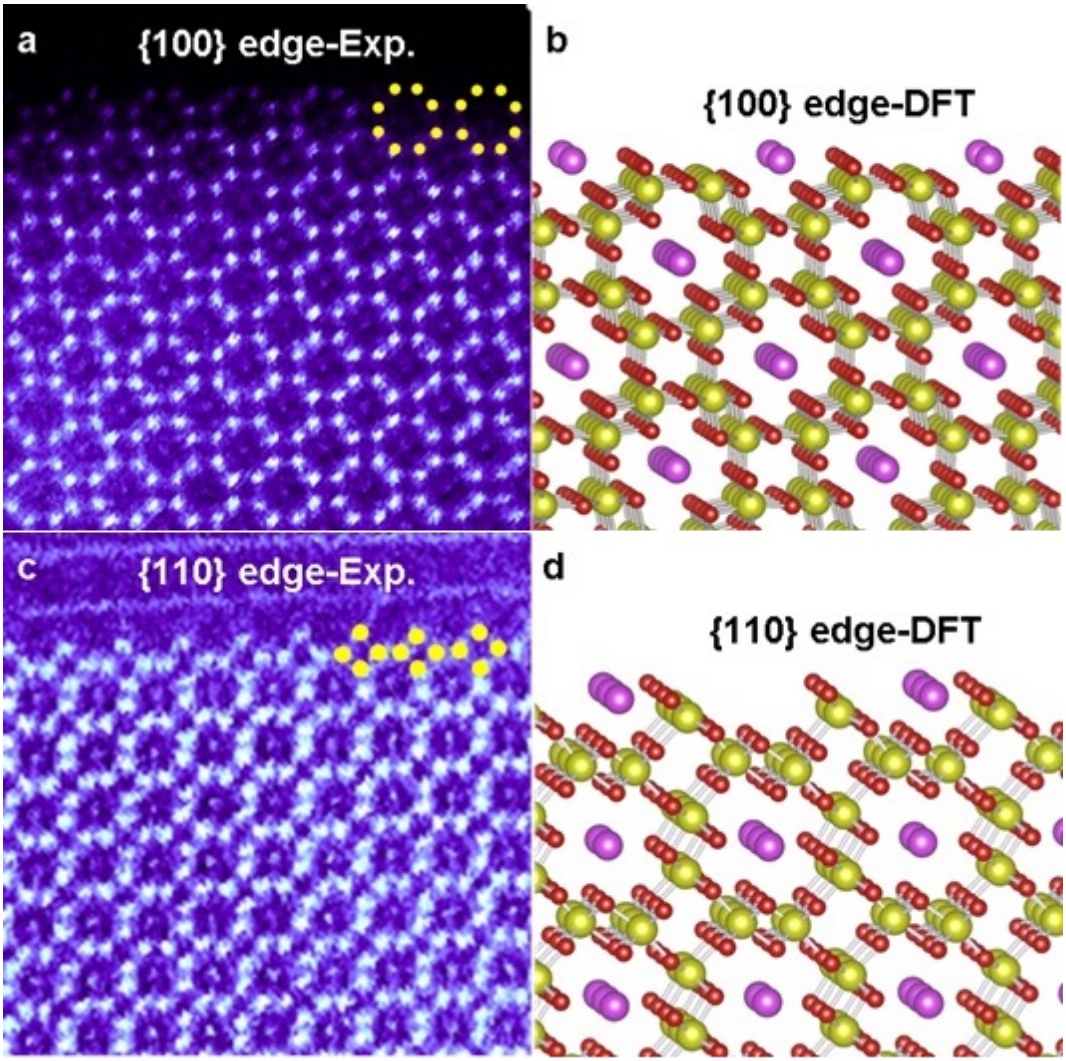

Figure 6-5: . *(a) Atomic-resolution HAADF image of a (100) edge in an α-$K_{0.25}MnO_2$ nanowire compared with (b) the calculated relaxed (100) surface structure of α-$K_{0.25}MnO_2$. (c) Atomic-resolution HAADF image of a (110) edge in an α-$K_{0.25}MnO_2$ nanowire compared with (d) the calculated relaxed (110) surface structure of α-$K_{0.25}MnO_2$. Yellow balls are Mn, red are O, and purple are K.*

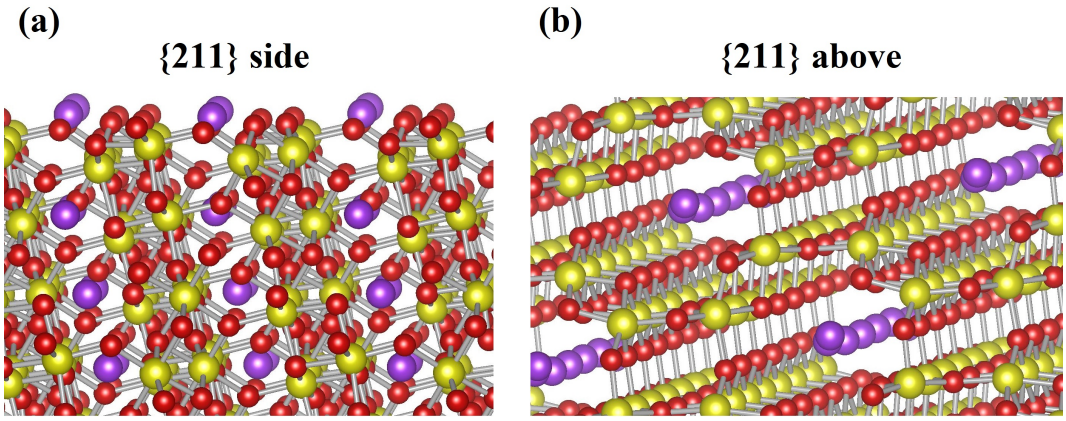

Figure 6-6: *(211) surface of $K_{0.25}MnO_2$ (a) side view and (b) above view showing access to 2×2 tunnels; O in red, Mn in yellow and K in purple.*

is given in Figure 6-5(d). The (110) surface forms a step-like edge that is covered by 1×1 tunnels, matching the theoretical model very well. Like the (100) surface, there is relatively little calculated distortion between the unrelaxed and simulated relaxed structures, indicating that this surface is relatively stable. The atomistic model also shows that the Mn ions at the (110) surface remain in a high coordination environment, with two thirds in 6-fold coordination sites. The remaining Mn ions, corresponding to the most exposed ions, are in 5-fold coordination. Furthermore, the outermost K^+ ions are stabilised by a slight relaxation into the surface, which has the effect of increasing their coordination number from 4 to 5. It is worth mentioning that the (110) surface has more unsaturated [MnO_5] units than the (100) surface, a consequence of which is that the (110) surface is predicted to be less stable than (100). All the other surfaces have larger amounts of unsaturated [MnO_5] units, with some even containing [MnO_x] (x<5) units, making them unstable in solution.

Finally, the (211) surface forms with an essentially planar surface, displayed in Figure 6-6, exposing the (001) tunnels containing the K^+ ions. As such this surface is particularly interesting as is provides access to the 2×2 channels in the α-MnO_2 framework. The exposed tunnel structure allows the outermost K^+ ions to relax slightly at the surface around the tunnel entrance, with relatively little surface relaxation of the Mn ions. A slight distortion of the outermost O ions is found around the 2×2 tunnel entrance, although the effect on the size of the tunnel opening is negligible. All the surface Mn ions are found in 5-fold coordination, which contrasts with other surfaces with a

(001) component (such as the (001) and (111) surfaces) where a fraction of the Mn ions have 4-fold or 3-fold coordination. These structural features, in particular the coordination environment of surface Mn ions, are likely to account for the low surface energies calculated for the (100), (110) and (211) surfaces.

Based on the sub-angstrom resolution image of the (110) edge structure (Figure 6-5) and the calculated surface energies an atomistic model has been proposed by Shahbazian-Yassar et al [217] to explain the formation of 2×3 tunnels at a {110} interface between two primary crystals (termed I_a and I_b). This process is illustrated in Figure 6-7, and is divided into three steps. At the beginning of the first step when I_a and I_b initially form in solution, the dominant surfaces should be {100} and {110} as both types of surface possess lower surface energies than other crystal planes. Since {110} surfaces are less stable than {100}, there is a tendency among the primary crystals to attach to each other along their {110} surfaces to minimise the overall energy. Consequently, as the reaction proceeds, I_a and I_b attract each other through van der Waals forces and orient themselves parallel to {110} surfaces. In the second step, as I_a and I_b come into close proximity, the large repulsive force between exposed K ions on the {110} surfaces prevent them bonding. However, extra [MnO_x] radicals in the surrounding solution are able to squeeze between the I_a and I_b crystals. In the third step, the extra [MnO_x] radicals between the crystals bond with the dangling [MnO_5] units from both {110} surfaces, resulting in the elimination of the two surfaces and formation of one 2×3 tunnel-based {110} interface as proposed by Shahbazian-Yassar et al [217]. This process should be energetically favourable as the unsaturated [MnO_5] units of the {110} surfaces become saturated, forming the more stable [MnO_6] units. Following similar steps, more primary α-MnO_2 nanowires can be gradually attached together across their exposed {110}, and the diameter of the secondary nanowire could be gradually increased during the subsequent high order self-assembly in solution.

Although this study is not exhaustive, it does highlight an important area for further work on tunnel-based oxide nanostructures. Indeed, future studies could include rational design of various tunnelled structures and large-scale molecular dynamics simulations in solution-based systems.

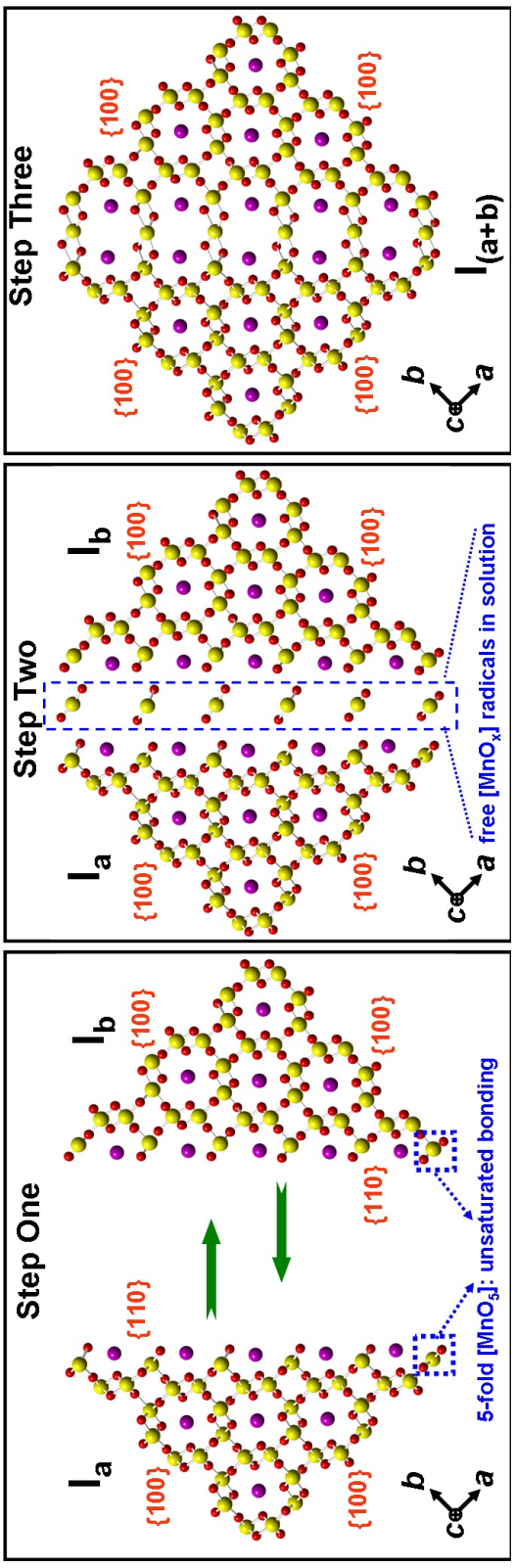

Figure 6-7: *Schematic diagrams illustrating the formation of a 2×3 tunnel-based $\{110\}$ interface during OA of two primary α-MnO_2 nanowires at the atomic level. The nanowires (I_a and I_b) are orientated parallel to the c axis ([001]) with their stable $\{100\}$ surfaces and metastable $\{110\}$ surfaces exposed in solution. Surrounding the nanowires is the aqueous solution environment containing $MnSO_4$ and $KMnO_4$ in excess [217].*

6.4 Chapter Summary

A combination of *ab initio* simulation and aberration corrected-STEM techniques has been used to examine the surface structures and nanowire morphologies of K^+-stabilised α-MnO_2. The main findings can be summarised as follows:

(a) α-$K_{0.25}MnO_2$ grown through a hydrothermal synthesis methods is found to produce primary nanowires with preferential growth along the [001] direction. Primary nanowires attach through a shared (110) interface to form larger secondary nanowires.

(b) DFT calculations on α-$K_{0.25}MnO_2$ indicate that the (100) surface is lowest in energy and will dominate the equilibrium morphology, in excellent agreement with observed microscopy images. The next lowest energy surface is (110), providing an explanation for its presence in the nanowires, particularly at the primary nanowire interfaces. The (211) surface displays the lowest surface energy containing a [001] component and is predicted to form the capping surface to the nanowires. The ranking of surface energies is driven by Mn coordination environments and surface relaxation.

(c) Finally, the calculated equilibrium morphology (dominated by (100) surfaces) is consistent with the observed primary nanowires suggesting that their growth is close to an equilibrium process.

These results offer insight into the surfaces structures of K^+- stablised α-MnO_2. The good agreement between DFT calculations and observed structures from electron microscopy should aid the rational design of tunnel-based oxide nanostructures for future energy storage applications.

7 Conclusions and Further Work

"I may not have gone where I intended to go, but I
think I have ended up where I intended to be."
Douglas Adams

7.1 General Remarks

This thesis has described computer modelling studies of a range of cathode materials for rechargeable batteries. Such work has been motivated by the knowledge that the emerging technologies of electric vehicles and grid storage require next generation battery materials, with greatly improved electrochemical performance. This is fundamentally a materials science challenge and, as such, simulations have been used to explore the atomic-scale properties of various compounds. A broad range of properties have been considered including structural, defect, diffusion, voltage and surface related phenomena. Much of the work herein has been focused on understanding experimental observations at the atomistic level. In addition, where possible there are predictive results acting as a guide to future studies to facilitate materials development. It seems pertinent to conclude this thesis with a summary of the main results and conclusions, as well as suggestions of avenues for further work.

7.2 Na-ion Mobility in Olivine $NaFePO_4$ and Layered Na_2FePO_4F

Chapter 3 details an investigation comparing the atomistic properties of the compositionally similar yet structurally distinct Na-ion cathodes Na_2FePO_4F and $NaFePO_4$ using potentials based techniques. Insights have been provided into the defect chemistry, Na diffusion pathways and volume expansion effects of the two materials. The simulations show good reproduction of the observed structures of the olivine $NaFePO_4$ and layered Na_2FePO_4F materials that were investigated. The energy for antisite defect formation in olivine $NaFePO_4$ is lower than in $LiFePO_4$, suggesting a higher degree of Na on Fe sites in accordance with the known metastability of the ordered $NaFePO_4$ phases. Significantly, the activation energy barrier for Na-ion conduction in the $NaFePO_4$ olivine framework along the 1D channels is lower than for Li-ion migration in $LiFePO_4$. The Na migration barriers in the layered Na_2FePO_4F are equally favourable, indicating high Na mobility through a 2D network in the *ac* plane.

Furthermore, the relationship between ionic transport and electrochemical properties among these materials highlights the crucial importance of the volume expansion-induced strain on de(intercalation). The strain contributes significantly to the overall energy for redox phase transformation, hence materials which display a large difference in the volume of the end member phases will invariably demonstrate a lower rate capability than similar materials with a reduced volume change between end members. $NaFePO_4$ displays intermediate volume expansion combined with a low activation barrier leading to reasonable, but not especially impressive, electrochemical properties. This is exacerbated by the 1D nature of diffusion, where antisite defects will present additional barriers to Na^+ diffusion. Conversely, very promising electrochemical properties are anticipated for Na- ion materials, such as Na_2FePO_4F, which demonstrate a low volume change upon cycling coupled with low activation energy barriers to migration. However, it must be noted that other properties will also come in to play, particularly the influence of electrical conduction and electrolyte interactions. Although the interplay of all the above factors is clearly complex and still under investigation, these findings provide guidelines for the future design and synthesis of high rate Na-ion

positive electrodes for intercalation batteries.

Further Work: Perhaps one of the most useful avenues for further work would involve exploring the effects of doping on the Na_2FePO_4F material. At 3.2 eV vs Na/Na^+ the voltage of $NaFePO_4F$ is lower than ideal for an Na-ion cathode. Therefore, a DFT study into the effects on voltage of transition metal doping would be valuable. For example, Na_2CoPO_4F is known to be isostructural to Na_2FePO_4F and thus may be miscible over a range of compositions. In addition, running large scale MD on both $NaFePO_4$ and Na_2FePO_4F systems, with similar levels of antisite defects inserted, could be used to probe the relative influence of antisites in 1D vs 2D Na^+ conductors. This would provide fundamental quantitative information into the importance of an effect which is often only discussed in qualitative terms.

7.3 Surfaces and Morphologies of Na_2FePO_4F

In **Chapter 4** work on Na_2FePO_4F has been extended, using DFT techniques, to include the surface structures and energetic, with the morphologies of nanoparticles computed and considered with respect to the electrochemical properties of Na_2FePO_4F as a Na-ion cathode. The lowest energy surfaces are found to be the (010), $(02\bar{1})$, $(1\bar{3}0)$, $(1\bar{1}0)$ and $(1\bar{2}\bar{2})$ planes, all of which are Tasker type II surfaces. All surfaces were found to undergo significant relaxation, with computed surface energies decreasing by ∼15-40% upon energy minimisation. However the low energy surfaces tended towards the lower end of this spectrum (∼15-30%), suggesting the most stable surfaces are those that remain most similar to the bulk structure. Indeed a positive correlation is found between the number of surface Fe remaining 6-coordinate (as in the bulk) and the relative surface stability.

The equilibrium morphology of Na_2FePO_4F forms a hexagonal structure, compressed along the [010] direction, with the (010), $(02\bar{1})$, $(1\bar{2}\bar{2})$ and $(1\bar{1}0)$ surfaces prominent. The overall morphology is not dissimilar to that calculated for $NaFePO_4$, although different surfaces are significant in each case. Conversely, the growth morphology forms a more extended rod-like structure, with the $(02\bar{1})$, $(02\bar{3})$, $(1\bar{1}0)$ and $(1\bar{1}\bar{2})$ surfaces domi-

nant. The (010) surface lies parallel to the Na containing *ac* layers of the bulk structure and previous calculation suggest interlayer Na^+ intercalation is unfavourable. As such, the prevalence of the (010) in the equilibrium morphology, and absence from the growth morphology, suggests nanoparticles synthesised in a kinetically limited regime should demonstrate better rate performance than those grown in close to equilibrium conditions. This is in qualitative agreement with experimental studies synthesizing different Na_2FePO_4F nanoparticle morphologies.

Finally, the redox potentials of selected surfaces have been investigated with DFT. Surface redox potentials vary between 2.76 - 3.37 V, in comparison to a value of 2.91 V calculated for insertion/extraction in bulk Na_2FePO_4F. Most significantly the lowest energy potentials are found for the $(1\bar{3}0)$ and (001) planes suggesting that upon charging Na^+ will first be extracted from these surfaces, and inserted lastly upon discharging.

Further Work: Given the variety of surfaces predicted for the Na_2FePO_4F morphologies, most of which provide access to the Na layers, it would be useful to have a deeper understanding of the energetics of Na^+ intercalation into the surfaces. This could be explored in a series of constrained minimisation or nudged elastic band calculations on each surface plane. Such an approach would provide a map of the activation barriers for Na^+ diffusion into the surfaces, assisting in identifying which surfaces are most promising for facile Na^+ intercalation and should therefore be promoted in crystal growth.

7.4 $Na_4M_3(PO_4)_2P_2O_7$ Mixed Phosphates (M = Fe, Mn, Ni, Co) as High Rate Cathodes: Defects, Na-ion Diffusion and Voltage Trends

In **Chapter 5** a combination of atomistic energy minimisation, MD and DFT simulation techniques have been used to provide insight into the defect chemistry, Na-ion diffusion and voltage trends in the $Na_4M_3(PO_4)_2P_2O_7$ [M = Fe, Mn, Ni, Co] Na-ion cathodes. All of the models employed provide an accurate reproduction of the complex

structure for all compositions. In each transition metal compound the most favourable intrinsic defect is found to be Na/M antisite pairs. This is a similar situation to that observed in other phosphate materials such as Na_2FePO_4F and $Na_2FeP_2O_7$.

Large-scale MD simulations allowed us to explore Na-ion diffusion kinetics and transport mechanisms. Na^+ diffusion coefficients (D_{Na}) are of the order $10^{-10}-10^{-11} cm^2 s^{-1}$ at 325 K and activation barriers are found to be 0.20-0.24 eV in the Fe- and Mn-based materials. These values compare favourably to successful Li-ion cathodes indicating rapid Na-ion transport which, coupled with the small volume change observed on cycling, suggests high rate capability and good cycle life. In addition, the MD trajectories suggest a 3D network of migration pathways, with all sodium ions diffusing. Closer analysis indicates that all pathways involving Na2 and Na3 sites are essentially linear, whilst for diffusion down the *b*-axis channels (Na1 and Na4 sites) curved trajectories are found.

Finally, DFT methods have been used to explore voltage trends. The experimental voltage of $Na_4Fe_3(PO_4)_2P_2O_7$ is reproduced and higher cell voltages for $Na_4Mn_3(PO_4)_2P_2O_7$ and $Na_4Ni_3(PO_4)_2P_2O_7$ are predicted. Moreover, we demonstrated that doping $Na_4Fe_3(PO_4)_2P_2O_7$ with Ni can lead to a significant increase in voltage.

These results will assist in developing strategies for optimizing these novel phosphates as possible high-rate Na-ion cathodes, especially for the more cost-sensitive stationary storage sector.

Further Work: Extending the transition metal doping work to ternary compositions (e.g. $Na_4FeNiMn(PO_4)P_2O_7$) would be interesting and provide a more complete overview of the effects of such doping. In a similar theme many Li-ion and Na-ion cathodes have been shown to be influenced by Mg doping, often improving electrochemical cyclability. The thermodynamics of such doping, in either binary, ternary or quaternary compounds, could be probed with DFT and promising compositions identified. Finally, the substitution of alternative polyanion groups will modify the cathode voltage and energy density. It would be interesting to explore this with DFT, across both isovalent and aliovalent groups with compensating defects, over common polyanions including silicates, sulphates, borates and carbonates.

7.5 Surface Structures and Morphologies of K^+-stabilised α-MnO_2

In **Chapter 6** a combination of *ab initio* DFT simulation and AC-STEM techniques has examined the surface structures, nanowire morphologies and growth mechanism of K^+-stabilised α-MnO_2. α-$K_{0.25}MnO_2$ grown through a hydrothermal synthesis methods is found to produce primary nanowires with preferential growth along the [001] direction. Primary nanowires attach through a shared (110) interface to form larger secondary nanowires. DFT calculations indicate that the (100) surface is lowest in energy and will dominate the equilibrium morphology, in excellent agreement with experiment. The next lowest energy surface is the (110) termination, providing an explanation for its presence in the nanowires, particularly at the primary nanowire interfaces. The (211) surface displays the lowest surface energy of all surfaces containing a [001] component and is predicted to form the capping surface to the nanowires. The ranking of surface energies is driven by Mn coordination environments and surface relaxation and provides a mechanism for primary nanowire attachment to form secondary nanowires, proceeding via a three step process so as to minimise the total surface energy. Finally, the calculated equilibrium morphology is consistent with the observed primary nanowires suggesting, alongside the proposed secondary nanowire growth mechanism, that their growth is a close to equilibrium process.

These results offer insight into the surfaces and growth mechanism of α-$K_{0.25}MnO_2$. The good agreement between DFT calculations and observed structures from microscopy should aid the rational design and synthesis of tunnel-based oxide nanostructures for future energy storage applications.

Further Work: As this chapter has dealt with the influence of K^+-stabilization on the nanostructure of α-MnO_2 two further themes are immediately apparent. Firstly, a systematic investigation over a range of K^+ doping levels would provide useful information as to how such variations would affect the fundamental surface structures and morphologies. Following on from this, employing other computational techniques (energy minimisation, MD) the Li^+ or Na^+ intercalation properties of the as synthesised

K^+-stabilised αMnO_2 could be explored, providing fundamental insight into the defect and diffusion properties.

Bibliography

[1] Department of Energy and Climate Change, *2011 UK Greenhouse Gas Emissions, Provisional Figures and 2010 Greenhouse Gas Emissions, Final Figures by Fuel Type and End User*, Department of Energy and Climate Change technical report, 2011.

[2] Tesla Motors, online at http://www.teslamotors.com/enGB/, 2015.

[3] M. Miller, A. Holmes, B. Conlon and P. Savagian, *SAE Int. J. Engines*, 2011, **4**, 1102–1114.

[4] The Economist, *A sparky new motor*, 2010.

[5] J. M. Tarascon and M. Armand, *Nature*, 2001, **414**, 359–367.

[6] A. Ponroach, D. Monti, A. Boschin, B. Steen, P. Johansson and M. R. Palacin, *J. Mater. Chem. A*, 2015, **3**, 22–42.

[7] D. Kundu, E. Talaie, V. Duffort and L. F. Nazar, *Angew. Chem. Int. Ed.*, 2015, **54**, 3431–3448.

[8] K. H. Wedepohl, *Geochim. Cosmochim. Ac.*, 1995, **59**, 1217–1232.

[9] J. B. Goodenough and Y. Kim, *Chem. Mater.*, 2010, **22**, 587–603.

[10] M. S. Whittingham, *Chem. Rev.*, 2004, **104**, 4271–4301.

[11] M. S. Islam and C. A. J. Fisher, *Chem. Soc. Rev.*, 2014, **43**, 185–204.

[12] M. Winter, J. O. Besenhard, M. E. Spahr and P. Novak, *Adv. Mater.*, 1998, **10**, 725–763.

[13] M. Winter and R. J. Brodd, *Chem. Rev.*, 2004, **104**, 4245–4269.

[14] M. D. Slater, D. Kim, E. Lee and C. S. Johnson, *Adv. Funct. Mater.*, 2013, **23**, 947–958.

[15] Y. Nishi, *J. Power Sources*, 2001, **100**, 101–106.

[16] H. P. R. Frederikse, *CRC Handbook of Chemistry and Physics*, CRC Press, 2005.

[17] M. S. Whittingham, *Prog. Solid State Ch.*, 1978, **12**, 41–99.

[18] A. S. Nagelberg and W. L. Worrell, *J. Solid State Chem.*, 1979, **29**, 345–354.

[19] U. S. D. of the Interior, *Rare Earth Elements - Critical Resources for High Technology*, USGS Fact Sheet 087-02, 2002.

[20] V. Palomeres, P. Serras, I. Villaluenga, K. B. Hueso and J. Carretero-Gonzalez, *Energy Environ. Sci.*, 2012, **5**, 5884–5901.

[21] B. L. Ellis and L. F. Nazar, *Curr. Opin. Solid St. M.*, 2012, **16**, 168–177.

[22] N. Yabuuchi, K. Kubota, M. Dahbi and S. Komaba, *Chem. Rev.*, 2014, **114**, 11636–11682.

[23] M. Armand and J.-M. Tarascon, *Nature*, 2008, **451**, 652–657.

[24] S.-W. Kim, D.-H. Seo, X. Ma, G. Ceder and K. Kang, *Adv. Energy Mater.*, 2012, **2**, 710–721.

[25] A. Ponrouch and M. R. Palacin, *Electrochem. Commun.*, 2015, **54**, 51–54.

[26] M. M. Doeff, J. Cabana and M. Shirpour, *J. Inorg. Organomet. P.*, 2014, **24**, 5–14.

[27] A. Rudola, K. Saravanan, C. W. Mason and P. Balaya, *J. Mater. Chem. A*, 2013, **1**, 2653–2662.

[28] F. E. Mouahid, M. Bettach, M. Zahir, P. Maldonado-Manso, S. Bruque, E. R. Losilla and M. A. G. Aranda, *J. Mater. Chem.*, 2000, **10**, 2748–2757.

[29] H. Xiong, M. D. Slater, M. B. Balasubramanian and C. S. C. S. J. Rajh, *J. Phys. Chem. Lett.*, 2011, **2**, 2560–2565.

[30] S. Lunell, A. Stashans, L. Ojamae, H. Lindstrom and A. Hagfeldt, *J. Am. Chem. Soc.*, 1997, **119**, 7374–7380.

[31] Y. Xu, E. M. Lotfabad, H. L. Wang, B. Farbod, Z. W. Xu, A. Kohandehghan and D. Mitlin, *Chem. Commun.*, 2013, **49**, 8973–8975.

[32] T. Ohzuku, Z. Takehara and S. Yoshizawa, *Electrochim. Acta.*, 1979, **24**, 219–222.

[33] L. Wu, D. Buchholz, D. Bresser, L. G. Chagas and S. J. Passerini, *J. Power Sources*, 2014, **251**, 379–385.

[34] H. Usui, S. Yoshioka, K. Wasada, M. Shimizu and H. Sakaguchi, *ACS Appl. Mater. Inter.*, 2015, **7**, 6567–6573.

[35] P. Senguttuvan, G. Rousse, V. Seznec, J. M. Tarascon and M. R. Palacin, *Chem. Mater.*, 2011, **23**, 4109–4111.

[36] W. Wang, C. Yu, Z. Lin, J. Hou, H. Zhu and S. Jiao, *Nanoscale*, 2013, **5**, 594–599.

[37] A. Rudola, K. Saravanan, S. Devaraj, H. Gong and P. Balaya, *Chem. Commun.*, 2013, **49**, 7451–7453.

[38] S. Andersson and A. D. Wadsley, *Acta Crystallogr.*, 1962, **15**, 194–201.

[39] S. I. Park, I. Gocheva, S. Okada and J. Yamaki, *J. Electrochem. Soc.*, 2011, **158**, A1067–A1070.

[40] C. Delmas, F. Cherkaoui, A. Nadiri and P. Hagenmuller, *Mat. Res. Bull.*, 1987, **22**, 631–639.

[41] C. Delmas, A. Nadiri and J. L. Soubeyroux, *Solid State Ionics*, 1988, **28-30 (Part 1)**, 419–423.

[42] Y. H. Xu, Y. J. Zhu, Y. H. Liu and C. S. Wang, *Adv. Energy Mater.*, 2013, **3**, 128–133.

[43] H. Zhu, Z. Jia, Y. Chen, N. Weadock, J. Wan, O. Vaaland, X. Han, T. Li, and L. Hu, *Nano Lett.*, 2013, **13**, 3093–3100.

[44] Y. C. Liu, N. Zhang, L. F. Jiao, Z. L. . Tao and J. Chen, *Adv. Funct. Mater.*, 2015, **25**, 214–220.

[45] Y. Kim, K. H. Ha, S. M. Oh and K. T. Lee, *Chem. Eur. J.*, 2014, **20**, 11980–11992.

[46] T. Hatchard and M. N. Obrovac, *J. Electrochem. Soc.*, 2014, **161**, A1748–1752.

[47] A. Ponroach, R. Dedryvere, D. Monti, A. E. Demet, J. M. A. Mba, L. Croguennec, C. Masquelier, P. Johansson and M. R. Palacin, *Energy Environ. Sci.*, 2013, **6**, 2361–2369.

[48] C. Vidal-Arbarca, P. Lavela, J. L. Tirado, A. V. Chadwick, M. Alfredsson and E. Kelder, *J. Power Sources*, 2012, **197**, 314–318.

[49] S. Komaba, W. Murata, T. Ishikawa, N. Yabuuchi, T. Ozeki, T. Nakayama, A. Ogata, K. Gotoh and K. Fujiwara, *Adv. Funct. Mater.*, 2011, **21**, 3859–3867.

[50] M. H. Han, E. Gonzalo, G. Singh and T. Rojo, *Energy Environ. Sci.*, 2015, **8**, 81–102.

[51] C. Delmas, C. Fouassier and P. Hagenmuller, *Physica B & C*, 1980, **99**, 81–85.

[52] P. Vassilaras, X. Ma, X. Li and G. Ceder, *J. Electrochem. Soc.*, 2013, **160**, A207–A211.

[53] B. M. de Boisse, J.-H. Cheng, D. Carlier, M. Guignard, C.-J. Pan, S. Bordere, D. Filimonov, C. Drathen, E. Suard, D.-J. Hwang, A. Wattiaux and C. Delmas, *J. Mater. Chem. A*, 2015, **3**, 10976–10989.

[54] A. Caballero, L. Hernan, J. Morales, L. Sanchez, P. J. Santos and M. A. G. Aranda, *J. Mater. Chem.*, 2002, **12**, 1142–1147.

[55] N. Yabuuchi, H. Yoshida and S. Komaba, *Electrochemistry*, 2012, **80**, 716–719.

[56] N. Yabuuchi, M. Kajiyama, J. Iwatate, H. Nishikawa, S. Hitomi, R. Okuyama, R. Usui, Y. Yamada and S. Komaba, *Nat. Mater.*, 2012, **11**, 512–517.

[57] A. Bhide and K. Harihanan, *Solid State Ionics*, 2011, **192**, 360–363.

[58] J.-J. Ding, Y.-N. Zhou, Q. Sun, Q. Yu, X. Q. Yang and Z. W. Fu, *Electrochim. Acta.*, 2013, **87**, 388–393.

[59] R. Alcantara, J. M. Jimenez-Mateos, P. Lavela and J. L. Tirado, *Electrochem. Commun.*, 2001, **3**, 639–642.

[60] A. K. Rai, L. T. Anh, J. Gim, V. Mathew and J. Kim, *Ceram. Int.*, 2014, **40**, 2411–2417.

[61] S. Komaba, N. Yabuuchi, T. Nakayama, A. Ogata, T. Ishikawa and I. Nakai, *Inorg. Chem.*, 2012, **51**, 6211–6220.

[62] S. Komaba, C. Takai, T. Nakayama, A. Ogata and N. Yabuuchi, *Electrochem. Commun.*, 2010, **12**, 355–358.

[63] J.-J. Ding, Y.-N. Zhou, Q. Sun and Z.-W. Fu, *Electrochem. Commun.*, 2012, **22**, 85–88.

[64] D. Kim, E. Lee, M. Slater, W. Lu, S. Rood and C. S. Johnson, *Electrochem. Commun.*, 2012, **18**, 66–69.

[65] H. Liu, H. Zhoub, L. Chena, Z. Tanga and W. Yang, *J. Power Sources*, 2011, **16**, 814–819.

[66] D. Carlier, J. H. Cheng, R. Berthelot, M. Guignard, M. Yoncheva, R. Stoyanova, B. J. Hwang and C. Delmas, *Dalton T.*, 2011, **40**, 9306–9312.

[67] D. Hamani, M. Ati, J.-M. Tarascon and P. Rozier, *Electrochem. Commun.*, 2011, **13**, 938–941.

[68] M. Guignard, C. Didier, J. Darriet, P. Bordet, E. Elkaim and C. Delmas, *Nat. Mater.*, 2013, **12**, 74–80.

[69] C. Didier, M. Guignard, J. Darriet and C. Delmas, *Inorg. Chem.*, 2012, **51**, 11007–11016.

[70] C. Didier, M. Guignard, C. Denage, O. Szajwaj, S. Ito, I. Saadoune, J. Darriet and C. Delmas, *Electrochem. Solid St.*, 2011, **14**, A75–A78.

[71] J. Xu, S.-L. Chou, J.-L. Wang, H.-K. Liu and S.-S. Dou, *ChemElectroChem*, 2014, **1**, 371–374.

[72] S. Tepavcevic, H. Xiong, V. R. Stamenkovic, X. Zuo, M. Balasubramanian, V. B. Prakapenka, C. S. Johnson, and T. Rajh, *ACS Nano*, 2012, **6**, 530–538.

[73] Y. Cao, L. Xiao, W. Wang, D. Choi, Z. Nie, J. Yu, L. V. Saraf, Z. Yang and J. Liu, *Adv. Mater.*, 2011, **23**, 3155–3160.

[74] S. Komaba, T. Mikumo, N. Yabuuchi, A. Ogata, H. Yoshida and Y. Yamada, *J. Electrochem. Soc.*, 2010, **157**, A60–A65.

[75] S. Tepavcevic, H. Xiong, V. R. Stamenkovic, X. Zuo, M. Balasubramanian, V. B. Prakapenka, C. S. Johnson and T. Rajh, *ACS Nano*, 2011, **5**, 530–536.

[76] D. Jiang, H. Wang, G. Li, X. Lan, M. H. Abib, Z. Zhang and Y. Jiang, *J. Electrochem. Soc.*, 2015, **162**, A697–A703.

[77] E. Uchaker, Y. Z. Zheng, S. Li, S. L. Candelaria, S. Hu and G. Z. Cao, *J. Mater. Chem. A*, 2014, **2**, 18208–18214.

[78] J.-H. Park, K. Park, R.-H. Kim, D.-J. Yun, S.-Y. Park, D. Han, S.-S. Lee and J.-H. Park, *J. Mater. Chem. A*, 2015, **3**, 10730–10737.

[79] J. F. Whitacre, A. Tevar and S. Sharma, *Electrochem. Commun.*, 2010, **12**, 463–466.

[80] K. Zhang, X. P. Han, Z. Hu, X. L. Zhang, Z. L. Tao and J. Chen, *Chem. Soc. Rev.*, 2015, **44**, 699–728.

[81] Y. K. Sun, Z. H. Chen, H. J. Noh, D. J. Lee, H. G. Jung, Y. Ren, S. Wang, C. S. Yoon, S. T. Myung and K. Amine, *Nature Mater.*, 2012, **11**, 942–947.

[82] Z. W. Chen, Z. Jiao, D. Y. Pan, Z. Li, M. H. Wu, C. H. Shek, C. M. L. Wu and J. K. L. Lai, *Chem. Rev.*, 2012, **112**, 3833–3855.

[83] Z. Y. Wang, L. Zhou and X. W. Lou, *Adv. Mater.*, 2012, **24**, 1903–1911.

[84] J. M. Tarascon, D. G. Guyomard, B. Wilkins, W. R. McKinnon and P. Barboux, *Solid State Ionics*, 1992, **57**, 113–120.

[85] J. F. Whitacre, S. Shanbhag, A. Mohammed, A. Polonsky, K. Carlisle, J. Gulakowski, W. Wu, C. Smith, L. Clooney, D. Blackwood, J. C. Dandrea and C. Truchot, *Energy Technology*, 2015, **3**, 20–31.

[86] D. Su, H.-J. Ahn and G. J. Wang, *J. Mater. Chem. A*, 2013, **1**, 4845–4850.

[87] D. Su, H.-J. Ahn and G. Wang, *NPG Asia Mater.*, 2013, **5**, E70.

[88] D. A. Tompsett and M. S. Islam, *Chem. Mater.*, 2013, **25**, 2515–2526.

[89] Y. Kadoma, T. Akahira, T. Fukuda, K. Ui and N. Kumagai, *Funct. Mater. Lett.*, 2012, **5**, 1250004.

[90] C. S. Johnson and M. M. Thackeray, *J. Power Sources*, 2001, **97-8**, 437–442.

[91] C. S. Johnson, *J. Power Sources*, 2007, **165**, 559–565.

[92] S.-M. Oh, S.-T. Myung, J. Hassoun, B. Scrosati and Y.-K. Sun, *Electrochem. Commun.*, 2012, **22**, 149–152.

[93] J. Lu, S. C. Chung, S. Nishimura and A. Yamada, *Chem. Mater.*, 2013, **25**, 4557–4565.

[94] J. Barker, M. Y. Saidi and J. L. Swoyer, *Electrochem. Solid St*, 2003, **6**, A1–A4.

[95] Z. Jian, L. Zhao, H. Pan, Y.-S. Hu, H. Li, W. Chen and L. Chen, *Electrochem. Commun.*, 2012, **14**, 86–89.

[96] Z. Jian, W. Han, X. Lu, H. Yang, Y.-S. Hu, J. Zhou, Z. Zhou, J. Li, W. Chen, D. Chen and L. Chen, *Adv. Energy Mater.*, 2012, **3**, 156–160.

[97] C. Zhu, K. Song, P. A. van Aken, J. Maier and Y. Yu, *Nano Lett.*, 2014, **14**, 2175–2180.

[98] K. Saravanan, C. W. Mason, A. Rudola, K. H. Wong and P. Balaya, *Adv. Energy Mater.*, 2012, **3**, 444–450.

[99] J. Liu, K. Tang, K. Song, P. A. van Aken, Y. Yu and J. Maier, *Nanoscale*, 2014, **6**, 5081–5086.

[100] K. Chihara, A. Kitajou, I. D. Gocheva, S. Okada and J. ichi Yamaki, *J. Power Sources*, 2013, **227**, 80–85.

[101] R. A. Shakoor, D. H. Seo, H. Kim, Y. U. Park, J. Kim, S. W. Kim, H. Gwon, S. Leec and K. Kang, *J. Mater. Chem.*, 2012, **22**, 20535–20541.

[102] W. Song, X. Ji, Z. Wu, Y. Zhu, F. Li, Y. Yao and C. E. Banks, *RSC Adv.*, 2014, **4**, 11375–11383.

[103] B. L. Ellis, W. R. M. Makahnouk, W. N. Rowan-Weetaluktuk, D. H. Ryan and L. F. Nazar, *Chem. Mater.*, 2010, **22**, 1059–1070.

[104] P. Barpanda, T. Ye, S. ichi Nashimura, S.-C. Chung, Y. Yamada, M. Okubo, H. Zhou and A. Yamada, *Electrochem. Commun.*, 2012, **24**, 116–119.

[105] P. Barpanda, G. Lui, C. D. Ling, M. Tamaru, M. Avdeev, S. C. Chung, Y. Yamada and A. Yamada, *Chem. Mater.*, 2013, **25**, 3480–3487.

[106] F. Sauvage, E. Quarez, J.-M. Tarascon and E. Baudrin, *Solid State Sci.*, 2006, **8**, 1215–1221.

[107] Y. U. Park, D. H. Seo, H. S. Kwon, B. Kim, J. Kim, H. Kim, I. . Kim, H. I. Yoo and K. .Kang, *J. Am. Chem. Soc.*, 2013, **135**, 13870–13878.

[108] A. Langrock, Y. Xu, Y. Liu, S. Ehrman, A. Manivannan and C. Wang, *J. Power Sources*, 2013, **223**, 62–67.

[109] B. L. Ellis, K. T. Lee and L. F. Nazar, *Chem. Mater.*, 2010, **22**, 691–714.

[110] N. Recham, J. N. Chotard, L. Dupont, K. Djellab, M. Armand and J. M. Tarascon, *J. Electrochem. Soc.*, 2009, **156**, A993–A999.

[111] Y. Kawabe, N. Yabuuchi, M. Kajiyama, N. Fukuhara, T. Inamasu, R. Okuyama, I. Nakai and S. Komaba, *Electrochem. Commun.*, 2011, **13**, 1225–1228.

[112] P. Barpanda, G. Oyama, S. Nishimura, S. C. Chung and A. Yamada, *Nat. Commun.*, 2014, **5**, 4358.

[113] H. Kim, I. Park, D.-H. Seo, S. Lee, S.-W. Kim, W. J. Kwon, Y.-U. Park, C. S. Kim, S. Jeon and K. Kang, *J. Am. Chem. Soc*, 2012, **134**, 10369–10372.

[114] I. V. Zatovsky, *Acta Crystallogr.*, 2010, **66**, 12–21.

[115] J. M. le Meins, M. P. Crosnier-Lopez, A. Hemon-Ribaud and G. Courbion, *J. Solid State Chem.*, 1999, **148**, 260–277.

[116] Q. Y. Wang, B. D. Zhao, S. Zhang, X. H. Gao and C. Deng, *J. Mater. Chem. A*, 2015, **3**, 7732–7740.

[117] W. X. Song, Z. P. Wu, J. Chen, Q. Lan, Y. R. Zhu, Y. C. Yang, C. C. Pan, H. S. Hou, M. J. Ming and X. B. Ji, *Electrochim. Acta*, 2014, **146**, 142–150.

[118] W. Song, X. Ji, J. Chen, Z. Wu, Y. Zhu, K. Ye, H. Hou, M. Jing and C. E. Banks, *Phys. Chem. Chem. Phys.*, 2015, **17**, 159–165.

[119] Y.-L. Ruan, K. Wang, S.-D. Song, X. Han and B.-W. Cheng, *Electrochim. Acta*, 2015, **160**, 330–336.

[120] G. Bauer, V. Guther, H. Hess, A. Otto, O. Roidl, H. Roller and S. Sattelberger, *Vanadium and Vanadium Compounds: Ullmann's Encylcopedia of Industrial Chemistry*, Wiley-VCH, 2000.

[121] F. Sanz, C. Parada, J. M. Rojo and C. Ruiz-Valero, *Chem. Mater.*, 2001, **13**, 1334–1340.

[122] M. Nose, H. Nakayama, K. Nobuhara, H. Yamaguchi and S. Nakanshi, *J. Power Sources*, 2013, **234**, 175–179.

[123] M. Gabelica-Robert, M. Goreaud, P. Labbe and B. Raveau, *J. Solid State Chem.*, 1982, **45**, 389–395.

[124] M. Reynaud, G. Rousse, A. M. Abakumov, M. T. Sougrati, G. V. Tendeloo, J. N. Chotarda and J. M. Tarascon, *J. Mater. Chem. A*, 2014, **2**, 2671–2680.

[125] P. Barpanda, G. Oyama, C. D. Ling and A. Yamada, *Chem. Mater.*, 2014, **26**, 1297–1299.

[126] L. Wong, H. M. Chen and S. Adams, *Phys. Chem. Chem. Phys.*, 2015, **17**, 9186–9193.

[127] N. Wongittharom, T. C. Lee, C. H. Wang, Y. C. Wang and J. Chang, *J. Mater. Chem. A*, 2014, **2**, 5655–5661.

[128] M. Casas-Cabanas, V. V. Roddatis, D. Saurel, P. Kubiak, J. Caretero-Gonzalez, V. Palomeres, P. Serras and T. Rojo, *J. Mater. Chem.*, 2012, **22**, 17421–17423.

[129] Y. Zhu, Y. Xu, Y. Liu, C. Luo and C. Wang, *Nanoscale*, 2013, **5**, 780–787.

[130] B. L. Ellis, W. R. M. Makahnouk, Y. Makimura, K. Toghill and L. F. Nazar, *Nat. Mater.*, 2007, **6**, 749–753.

[131] P. Moreau, D. Guyomard, J. Gaubicher and F. Boucher, *Chem. Mater.*, 2010, **22**, 4126–4128.

[132] R. Tripathi, S. M. Wood, M. S. Islam and L. F. Nazar, *Energy Environ. Sci.*, 2013, **6**, 2257–2264.

[133] I. K. Lee, I.-B. Shim and C. S. Kim, *J. Appl. Phys.*, 2011, **109**, 07E136.

[134] H. Zou, S. Li, X. Wu, M. J. McDonald and Y. Yang, *Electrochem. Lett.*, 2015, **4**, A53–A55.

[135] N. V. Kosova, V. R. Podugolnikov, E. T. Devyatkina and A. B. Slobodyuk, *Mat. Res. Bull.*, 2014, **60**, 849–857.

[136] M. Brisbois, N. Krins, R. P. Hermann, A. Schrijnemakers, R. Cloots, B. Vertruyen and F. Boschini, *Mater. Lett.*, 2014, **130**, 263–266.

[137] J. Zhou, J. Zhou, Y. Tang, Y. Bi, C. Wang, D. Wang and S. Shi, *Ceram. Int.*, 2013, **39**, 5379–5385.

[138] X. Wu, J. Zheng, Z. Gong and Y. Yang, *J. Mater. Chem.*, 2011, **21**, 18630–18637.

[139] H. Kim, I. Park, S. Lee, H. Kim, K.-Y. Park, Y.-U. Park, H. Kim, J. Kim, H.-D. Lim, W.-S. Yoon, and K. Kang, *Chem. Mater.*, 2013, **25**, 3614–3622.

[140] J. D. Gale, *J. Chem. Soc. Faraday Trans.*, 1997, **93**, 629.

[141] I. T. Todorov, W. Smith, K. Trachenko and M. T. Dove, *J. Mater. Chem.*, 2006, **16**, 1611–1618.

[142] S. Plimpton, *J. Comp. Phys.*, 1995, **117**, 1–19.

[143] G. Kresse and J. Furthermuller, *Phys. Rev. B. Condens. Matter Mater. Phys.*, 1996, **54**, 11169.

[144] G. Kresse and D. Joubert, *Phys. Rev. B: Condens. Matter Mater. Phys.*, 1999, **59**, 1758.

[145] A. R. Leach, *Molecular Modelling Principles and Applications*, Addison Wesley Longman Limited, 1996.

[146] A. K. Cheetham and P. Day, *Solid State Chemistry Techniques*, Clarenden Press, 1987.

[147] R. Catlow, A. Sokol and A. Walsh, *Computational Approaches to Energy Materials*, Wiley, 2013.

[148] E. Eberhard and R. M. Dreizler, *Density Functional Theory An Advanced Course*, Springer Berlin Heidelberg, 2011.

[149] T. Tsuneda, *Density Functional Theory in Quantum Chemistry*, Springer Japan, 2014.

[150] R. M. Martin, *Electronic Structure: Basic Theory and Practical Methods*, Cambridge Univeristy Press, 2004.

[151] R. G. Parr and W. Yang, *Density-Functional Theory of Atoms and Molecules*, Oxford University Press, 1989.

[152] C. J. Cramer, *Essentials of Computational Chemistry*, John Wiley and Sons, 2002.

[153] B. G. Dick and A. W. Overhauser, *Phys. Rev.*, 1958, **112**, 90–103.

[154] V. Klee and G. J. Minty, *How good is the simplex algorithm*, DTIC document technical report, 1970.

[155] S. L. Roux and V. Petkov, *ISAACS*, online, 2015.

[156] R. C. Ropp, *Solid State Chemistry*, Elsevier, 2003.

[157] J. M. Haile, *Molecular Dynamics Simulation: Elementary Methods*, John Wiley and Sons, 1992.

[158] J. C. Slater, *Phys. Rev.*, 1951, **81**, 385.

[159] P. A. M. Dirac, *Mathematical Proceedings of the Cambridge Philosophical Society*, 1930, **26**, 376–385.

[160] P. Hohenberg and W. Kohn, *Phys. Rev.*, 1964, **136**, B864.

[161] W. Kohn and L. J. Sham, *Phys. Rev.*, 1965, **140**, A1133.

[162] J. M. Tao, J. P. Perdew, V. N. Staroverov and G. E. Scuseria, *Phys. Rev. Lett.*, 2003, **91**, 146401.

[163] Y. Zhao, N. E. Schultz and T. D. G, *J. Chem. Phys.*, 2005, **123**, 161103.

[164] J. P. Perdew and A. Zunger, *Phys. Rev. B*, 1981, **23**, 5048.

[165] J. P. Perdew, J. A. Chevary, S. H. Vosko, K. A. Jackson, M. R. Pederson, D. J. Singh and C. Fiolhais, *Phys. Rev. B*, 1992, **46**, 6671.

[166] Z. Wu and R. E. Cohen, *Phys. Rev. B*, 2006, **73**, 235116.

[167] J. P. Perdew, K. Burke and M. Ernzerhof, *Phys. Rev. Lett.*, 1996, **77**, 3865.

[168] F. Bloch, *Zeitschrift fur Physik*, 1929, **52**, 555–600.

[169] P. Blaha, K. Schwarz, G. Madsen, D. Kvasnika and J. Luitz, *An Augmented Plane Wave and Local Orbitals Program for Calculating Crystal Properties*, Karlheinz Schwarz, Tecn. Universtitat Wein, Austria, 2001.

[170] P. E. Blochl, *Phys. Rev. B.*, 1994, **50**, 17953.

[171] P. W. Tasker, *J. Phys. C: Solid State Phys.*, 1979, **12**, 4977.

[172] P. Masri, P. W. Tasker, J. P. Hoare and J. H. R. Harding, *Surf. Sci.*, 1986, **173**, 439.

[173] G. Wulff, *Zeitschrift fur Krystallographie und Mineralogie*, 1901, **34**, 449–530.

[174] J. Gaubicher, C. Wurm, G. Goward, C. Masquelier and L. F. Nazar, *Chem. Mater.*, 2000, **12**, 3240–3242.

[175] K. T. Lee, T. N. Ramesh, F. Nan, G. Botton and L. F. Nazar, *Chem. Mater.*, 2011, **23**, 3593–3600.

[176] Y. Kawabe, N. Yabuuchi, M. Kajiyama, N. Fukuhara, T. Inamasu, R. Okuyama, I. Nakai and S. Komaba, *Electrochemistry*, 2012, **80**, 80–84.

[177] S. P. Ong, V. L. Chevrier, G. Hautier, A. Jain, C. J. Moore, S. Kim, X. Ma and G. Ceder, *Energy Environ. Sci.*, 2011, **4**, 3680–3688.

[178] M. S. Islam, D. J. Driscoll, C. A. J. Fisher and P. R. Slater, *Chem. Mater.*, 2005, **17**, 5085–5092.

[179] R. Tripathi, G. R. Gardiner, M. S. Islam and L. F. Nazar, *Chem. Mater.*, 2011, **23**, 2278–2284.

[180] J. N. Bridson, S. E. Quinlan and P. R. Tremaine, *Chem. Mater.*, 1998, **10**, 763–768.

[181] Y. Lepage and G. Donnay, *Can. Mineral.*, 1977, **15**, 518–521.

[182] K. Kang, D. Carlier, J. Reed, E. M. Arroyo, G. Ceder, L. Croguennec and C. Delmas, *Chem. Mater.*, 2003, **15**, 4503–4507.

[183] G. R. Gardiner and M. S. Islam, *Chem. Mater.*, 2010, **22**, 1242–1248.

[184] S. C. Nishimura, G. Kobayashi, K. Ohoyama, Y. Kanno, M. Yashima and A. Yamada, *Nat. Mater.*, 2008, **7**, 707–711.

[185] C. A. J. Fisher, V. M. H. Prieto and M. S. Islam, *Chem. Mater.*, 2008, **20**, 5907–5915.

[186] H. Chen, G. Hautier, A. Jain, C. Moore, B. Kang, R. Doe, L. Wu, Y. Tang and G. Ceder, *Chem. Mater.*, 2012, **24**, 2009–2016.

[187] C. Eames, J. M. Clark, G. Rousse, J.-M. Tarascon and M. S. Islam, *Chem. Mater.*, 2014, **26**, 3672–3678.

[188] M. Armand, J.-M. Tarascon and M. A. de Dompablo, *Electrochem. Commun.*, 2011, **13**, 1047–1050.

[189] A. Saracibar, A. V. der Ven and M. E. A. de Dompablo, *Chem. Mater.*, 2012, **24**, 495–503.

[190] C. A. J. Fisher and M. S. Islam, *J. Mater. Chem.*, 2008, **18**, 1209–1215.

[191] A. Whiteside, C. A. J. Fisher, S. C. Parker and M. S. Islam, *Phys. Chem. Chem. Phys.*, 2014, **16**, 21788–21794.

[192] M. Nose, K. Nobuhara, S. S. H. Nakayama, S. Nakanshi and H. Iba, *RSC Adv.*, 2014, **4**, 9044–9047.

[193] R. Tripathi, T. N. Ramesh, B. L. Ellis and L. F. Nazar, *Angew. Chem. Int. Ed.*, 2010, **49**, 8738–8742.

[194] R. Katoaka, T. Mukai, A. Yoshizawa and T. Sakai, *J. Electrochem. Soc.*, 2013, **160**, A933–A939.

[195] S. M. Wood, C. Eames, E. Kendrick and M. S. lslam, *J. Phys. Chem. C*, 2015, **119**, 15935–15941.

[196] A. Pedone, G. Malavasi, M. C. Menziani, A. N. Cormack and U. Segre, *J. Phys. Chem. B*, 2006, **110**, 11780–11795.

[197] J. M. Clark, S. ichi Nishimura, A. Yamada and M. S. Islam, *Angew. Chem. Int. Ed.*, 2012, **51**, 13149–13153.

[198] S. Y. Chung, S. Y. Choi, T. Yamamoto and Y. Ikuhara, *Phys. Rev. Lett.*, 2008, **100**, 125502.

[199] J. M. Clark, P. Barpanda, A. Yamada and M. S. Islam, *J. Mater. Chem. A*, 2014, **2**, 11807–11812.

[200] G. J. Shu and F. C. Chou, *Phys. Rev. B*, 2008, **78**, 052101.

[201] T. Jiang, G. Chen, A. Li, C. Wang and Y. Wei, *J. Alloy. Compd.*, 2009, **478**, 604 – 607.

[202] A. Yamada, M. Hosoya, S.-C. Chung, Y. Kudo, K. Hinokuma, K.-Y. Liu and Y. Nishi, *J. Power Sources.*, 2003, **119**, 232–238.

[203] J. Wolfenstine and J. Allen, *J. Power Sources*, 2005, **142**, 389–390.

[204] M. Tamaru, P. Barpanda, Y. Yamada, S. Nishimura and A. Yamada, *J. Mater. Chem.*, 2012, **22**, 24526–24529.

[205] D. Portehault, S. Cassaignon, E. Baudrin and J.-P. Jolivet, *Chem. Mater.*, 2007, **19**, 5410–5417.

[206] H. M. Galindo, Y. Carvajal, E. Njagi, R. A. Ristau and S. L. Suib, *Langmuir*, 2010, **26**, 13677–13683.

[207] B. Lan, L. Yu, T. Lin, G. Cheng, M. Sun, F. Ye, Q. Sun and J. He, *ACS Appl. Mater. Interfaces*, 2013, **5**, 7458–7464.

[208] D. Li, M. H. Nielsen, J. R. I. Lee, C. Frandsen, J. F. Banfield and J. J. D. Yoreo, *Science*, 2012, **336**, 1014–1018.

[209] S. Deveraj and N. Munichandraiah, *J. Phys. Chem.*, 2008, **112**, 4406–4417.

[210] T. X. T. Sayle, C. R. A. Catlow, R. R. Maphanga, P. E. Ngoepe and D. C. Sayle, *J. Am. Chem. Soc.*, 2005, **127**, 12828–12837.

[211] T. X. T. Sayle, C. R. A. Catlow, R. R. Maphanga, P. E. Ngoepe and D. C. Sayle, *J. Cryst. Growth*, 2006, **294**, 118–129.

[212] R. R. Maphanga, D. C. Sayle, T. X. T. Sayle and P. E. Ngoepe, *Phys. Chem. Chem. Phys.*, 2011, **13**, 1307–1313.

[213] D. A. Tompsett, S. C. Parker and M. S. Islam, *J. Am. Chem. Soc.*, 2014, **136**, 1418–1426.

[214] C. Ling and F. Mizuno, *Chem. Mater.*, 2012, **24**, 3943–3951.

[215] L. Trahey, N. K. Karan, M. K. Y. Chan, J. Lu, Y. Ren, J. Greeley, M. Balasubramanian, A. K. Burrell, L. A. Curtiss and M. M. Thackaray, *Adv. Energy Mater.*, 2013, **3**, 75–84.

[216] M. H. Rossouw, D. C. Liles, M. M. Thackaray, W. I. F. David and S. Hull, *Mater. Res. Bull.*, 1992, **27**, 221–230.

[217] Y. Yuan, S. M. Wood, K. He, W. Yao, D. A. Tompsett, J. Lu, A. Nie and M. S. I. ad R Shahbazian-Yassar, *ACS Nano*, 2015, **-**, [In Press].

[218] T. S. Arthur, R. Zhang, C. Ling, P. A. Glans, X. Fan, J. Guo and F. Mizuno, *ACS Appl. Mater. Interfaces*, 2014, **6**, 7004–7008.

[219] W. Li, , X. Cui, R. Zeng, G. Du, Z. Sun, R. Zheng, S. P. Ringer and S. X. Dou, *Sci. Rep.*, 2015, **5**, 8987.

[220] L. Li, C. Nan, Q. Peng and Y. Li, *Chem. Commun.*, 2012, **48**, 6945–6847.

[221] P. Yang, Y. Ding, Z. Lin, Z. Chen, Y. Li, P. Qiang, M. Ebrahimi, W. Mai, C. P. Wong and Z. L. Wang, *Nano Lett.*, 2014, **14**, 731–736.

[222] D. Zhai, B. Li, C. Xu, H. Du, Y. He, C. Wei and F. Kang, *J. Power Sources*, 2011, **196**, 7860–7867.

[223] W. Xiao, H. Xia, J. Y. H. Fuh and L. Lu, *J. Power Sources*, 2009, **193**, 935–938.

[224] Y. Qin, J. Lu, P. Du, Z. Chen, Y. Ren, T. Wu, J. T. Miller, J. Wen, D. J. Miller, Z. Zhang and K. Amine, *Energy Environ. Sci.*, 2013, **6**, 519–531.

[225] G. S. Hutchings, J. Rosen, D. Smiley, G. R. Goward, P. G. Bruce and F. Jiao, *J. Phys. Chem. C*, 2014, **118**, 12617–12624.

[226] T. T. Truong, Y. Liu, Y. Ren and L. T. Y. Sun, *ACS Nano*, 2012, **6**, 8067–8077.

[227] A. Debart, A. J. Paterson, J. Bao and P. G. Bruce, *Angew. Chem.*, 2008, **120**, 4597–4600.

[228] F. Kroger, *The Chemistry of Imperfect Crystals*, North-Holland:Amsterdam, 1974.

[229] J. C. Kim, C. J. Moore, B. Kang, G. Hautier, A. Jain and G. Ceder, *J. Electrochem. Soc.*, 2011, **158**, A309–A315.

[230] J. M. Clark, C. Eames, M. Reynaud, G. Rousse, J. N. Chotard, J. M. Tarascon and M. S. Islam, *J. Mater. Chem. A*, 2014, **2**, 7446–7453.

[231] D. Santamaria-Perez, U. Amador, J. Tartojada, R. Dominiko and M. E. A. de Dompablo, *Inorg. Chem.*, 2012, **51**, 5779–5786.

[232] D.-H. Seo, Y.-U. Park, S.-W. Kim, I. Park, R. A. Shakoor and K. Kang, *Phys. Rev. B: Condens. Mater.*, 2011, **83**, 205127.

[233] S.-W. Kim, D.-H. Seo, H. Kim, K.-Y. Park and K. Kang, *Phys. Chem. Chem. Phys.*, 2012, **14**, 3299–3303.

[234] D.-H. Seo, H. Gwon, S.-W. Kim, J. Kim and K. Kang, *Chem. Mater.*, 2010, **22**, 518–523.

[235] H. Kim, D.-H. Seo, H. Kim, I. Park, J. Hong, K.-Y. Park and K. Kang, *Chem. Mater.*, 2012, **24**, 720–725.

[236] H. Kim, D. J. Kim, D.-H. Seo, M. S. Yeom, K. Kang, D. K. Kim and Y. Jung, *Chem. Mater.*, 2012, **24**, 1205–1211.

[237] D. H. Lee, J. Xu and Y. S. Meng, *Phys. Chem. Chem. Phys.*, 2013, **15**, 3304–3312.

[238] D. Qian, B. Xu, M. Chi and Y. S. Meng, *Phys. Chem. Chem. Phys.*, 2014, **16**, 14665–14668.

[239] B. Xu, C. R. Fell, M. Chi and Y. S. Meng, *Energy Environ. Sci.*, 2011, **4**, 2223–2233.

[240] C. R. Fell, D. H. Lee, Y. S. Meng, J. M. Gallardo-Amores, E. Moran and M. E. Arroyo-de Dompablo, *Energy Environ. Sci.*, 2012, **5**, 6214–6224.

[241] M.-C. Yang, B. Xu, J.-H. Cheng, C.-J. Pan, B.-J. Hwang and Y. S. Meng, *Chem. Mater.*, 2011, **23**, 2832–2841.

[242] D. A. Tompsett, S. C. Parker, P. G. Bruce and M. S. Islam, *Chem. Mater.*, 2013, **25**, 536–541.

[243] D.-H. Seo, H. Kim, I. Park, J. Hong and K. Kang, *Phys. Rev. B*, 2011, **84**, 220106.

[244] C. Eames, A. R. Armstrong, P. G. Bruce and M. S. Islam, *Chem. Mater.*, 2012, **24**, 2155–2161.

[245] A. Abdellahi, O. Akyildiz, R. Malik, K. Thornton and G. Ceder, *J. Mater. Chem. A*, 2014, **2**, 15437–15447.

[246] P. Vassilaras, A. J. Toumar and G. Ceder, *Electrochem. Commun.*, 2014, **38**, 79–81.

[247] D. Qian, Y. Hinuma, H. Chen, L.-S. Du, K. J. Carroll, G. Ceder, C. P. Grey and Y. S. Meng, *J. Am. Chem. Soc.*, 2012, **134**, 6096–6099.

[248] Z. Jian, H. Yu and H. Zhou, *Electrochem. Commun.*, 2013, **34**, 215–218.

[249] D. J. Kim, R. Ponraj, A. G. Kannan, H.-W. Lee, R. Fathi, R. Ruffo, C. M. Mari and D. K. Kim, *J. Power Sources.*, 2013, **244**, 758 – 763.

[250] R. Ruffo, R. Fathi, D. J. Kim, Y. H. Jung, C. M. Mari and D. K. Kim, *Electrochim. Acta.*, 2013, **108**, 575–582.

[251] C. J. Hung, P. Lin and T. Y. Tseng, *J. Power Sources.*, 2013, **243**, 594–602.

[252] T. Shibata, W. Kobayashi and Y. Moritomo, *Appl. Phys. Express.*, 2013, **6**, 097101.

[253] T. Shibata, W. Kobayashi and Y. Moritomo, *Appl. Phys. Express*, 2014, **7**, 067101.

[254] S. Guo, H. Yu, Z. Jian, P. Liu, Y. Zhu, X. Guo, M. Chen, M. Ishida and H. Zhou, *ChemSusChem*, 2014, **7**, 2115–2119.

[255] C. Deng, S. Zhang, Z. Dong and Y. Shang, *Nano Energy*, 2014, **4**, 49–55.

[256] N. Bockenfield and A. Balducci, *J. Solid State Electrochem.*, 2014, **18**, 959–964.

[257] W. Song, X. Ji, Z. Wu, Y. Yang, Z. Zhou, F. Li, Q. Chen and C. E. Banks, *J. Power Sources.*, 2014, **256**, 258–263.

[258] L. Su, J. Winnick and P. Kohl, *J. Power Sources.*, 2001, **101**, 226–230.

[259] M. Vujkovic and S. Mentus, *J. Power Sources.*, 2014, **247**, 184–188.

[260] Y. Wang, X. Yu, S. Xu, J. Bai, R. Xiao, Y.-S. Hu, H. Li, X.-Q. Yang, L. Chen and X. Huang, *Nat. Commun.*, 2013, **4**, 2365.

[261] X. Yu, H. Pan, W. Wan, C. Ma, J. Bai, Q. Meng, S. N. Ehrlich, Y.-S. Hu and X.-Q. Yang, *Nano Lett.*, 2013, **13**, 4721–4727.

A Kroger-Vink notation

Whilst various symbolisms exist to describe defects succinctly, Kroger-Vink notation is one of the most commonly employed. The formalism is based upon the structure

$$X_Y^Z \tag{A.1}$$

whereby X indicates the species present, Y the location of the species and Z the net charge with respect to the crystal lattice. The possible components of X, Y and Z are given in Table A.1. The number of $\bullet$ or $'$ indicate the net charge of the species (i.e. $\bullet\bullet\bullet$ represents +3). So for instance a calcium ion on a calcium site would take the form

$$Ca_{Ca}^{\times} \tag{A.2}$$

Table A.1: *Components involved in Kroger-Vink defect notation to describe point defects in solids.*

Component	Possible Values	Description
X	V	Vacancy
	H, Li, Be...	Atomic symbol of lattice site ion
Y	H, Li, Be...	Atomic symbol of species
	i	interstitial site
Z	$\times$	neutral charge
	$\bullet$	positive charge
	$'$	negative charge

whilst an oxygen vacancy would be

$$V_O^{\bullet\bullet} \tag{A.3}$$

In this manner defect equations can be built up, for example the formation of an oxygen Frenkel defect,

$$O_O^{\times} \rightarrow V_O^{\bullet\bullet} + O_i^{''} \tag{A.4}$$

this formalism comprises the notation employed throughout this study [228].

B Tabulated U_{eff} values

Table B.1: *Tabulated U_{eff} values from Li-ion/Na-ion cathode studies.*

Transition metal	Material	U-J value (eV)	Reference
$\mathbf{Mn^{2+}/Mn^{3+}}$	Borate	3.9	Ceder et al.[229]
	Carbonophosphate	3.9	Ceder et al.[186]
	Sulphate	3.9	Islam et al.[230]
	Oxide and phosphate	4.0	Ceder et al.[177]
	Silicate	4.0	Dompablo et al.[231]
	Silicate	4.0	Van der Ven et al.[189]
	Borate	4.5	Kang et al.[232]
	Fluorophosphate	4.5	Kang et al.[233]
	Phosphate	4.5	Kang et al.[234]
	Oxide Spinel	5.0	Kang et al.[235]
$\mathbf{Mn^{3+}/Mn^{4+}}$	Oxide	3.9	Kang et al.[236]
	Oxide	4.0	Meng et al.[237]
	Oxide	5.0	Meng et al.[238]
	Oxide	5.0	Meng et al.[239]
	Oxide	5.0	Dompablo et al.[240]
	Oxide Spinel	5.0	Meng et al.[241]
	Oxide	5.1	Islam et al.[242]
	Oxide	5.2	Islam et al.[88]

Fe^{2+}/Fe^{3+}	Oxide and phosphate	3.9	Ceder et al.[177]
	Silicate	4.0	Kang et al.[243]
	Carbonophosphate	4.0	Ceder et al.[186]
	Hydroxysulfate	4.0	Islam et al.[187]
	Silicate	4.0	Islam et al.[244]
	Silicate	4.0	Dompablo et al.[188]
	Sulphate	4.0	Islam et al.[230]
	Silicate	4.0	Van der Ven et al.[189]
	Borate	4.3	Kang et al.[232]
	Mixed Phosphate	4.3	Kang et al.[139]
	Phosphate	4.3	Kang et al.[234]
	Phosphate	4.39	Ceder et al.[245]
	Oxide Spinel	5.0	Kang et al.[235]
Fe^{3+}/Fe^{4+}	Oxide	4.0	Ceder et al.[246]
Ni^{2+}/Ni^{3+}	Silicate	4.0	Van der Ven et al.[189]
	Carbonophosphate	6.0	Ceder et al.[186]
Ni^{3+}/Ni^{4+}	Oxide	5.96	Meng et al.[238]
	Oxide	5.96	Meng et al.[239]
	Oxide	5.96	Dompablo et al.[240]
	Oxide Spinel	5.96	Meng et al.[241]
	Oxide	6.1	Meng et al.[237]
	Oxide	6.0	Ceder et al.[246]
Co^{2+}/Co^{3+}	Oxide Spinel	4.3	Kang et al.[235]
	Silicate	4.0	Dompablo et al.[231]
	Silicate	4.0	Van der Ven et al.[189]
	Borate	5.7	Kang et al.[232]
	Carbonophosphate	5.7	Ceder et al.[186]
	Phosphate	5.7	Kang et al.[234]
	Sulphate	5.7	Islam et al.[230]
Co^{3+}/Co^{4+}	Oxide	3.0	Meng et al.[247]
	Oxide	3.4	Ceder et al.[246]

C Collated Na^+ Diffusion Constants

Table C.1: *Published Na^+ ion diffision constants in Na-ion cathode materials.*

Diffusion constant (cm^2s^{-1})	Material	Reference
10^{-14}	Na rich layered oxides	Zhou et al.[248]
10^{-16} - 10^{-12}	$Na_{0.44}MnO2$	Kim et al.[249]
10^{-14} - 10^{-13}	$Na_{0.44}MnO_2$	Kim et al.[250]
10^{-8}	MnO_2	Tseng et al. [251]
10^{-11}	Na_xCoO_2	Moritomo et al.[252]
10^{-11}	Na_xMnO_2	Moritomo et al.[253]
10^{-8} - 10^{-7}	Na_xCoO_2	Chou et al.[200]
10^{-15} - 10^{-13}	$NaMn_3O_5$	Zhou et al. [254]
10^{-14}	$Na_2V_6O_{16} \cdot nH_2O$	Shang et al. [255]
10^{-15} - 10^{-13}	$Na_3V_2(PO_4)_3$	Balducci et al [256]
10^{-10}	$Na_3V_2(PO_4)_2F$-3C	Wei et al. [201]
10^{-12}	$Na_3V_2(PO_4)_2F$	Banks et al.[257]
10^{-14} - 10^{-12}	V_2O_5	Kohl et al.[258]
10^{-15}	$NaFePO_4$	Mentus et al.[259]
10^{-10}	$Na_{0.66}[Li_{0.22}Ti_{0.78}]O_2$	Huang et al.[260]
10^{-11}	$Li_4Ti_5O_{12}$	Yang et al.[261]

D Isolated Defect Energies

Table D.1: *Isolated defect energies of intrinsic defects in Na_2FePO_4F*

Defect type	**Species$_{\text{Site}}$**	**Defect energy (eV)**
Vacancy	P	157.61
Vacancy	Fe	22.27
Vacancy	Na	5.91
Vacancy	O	23.60
Vacancy	F	5.81
Interstitial	Na	-2.57
Interstitial	Fe	-17.17
Interstitial	O	-16.55
Interstitial	F	-3.21
Impurity	Fe_{Na}	-14.81
Impurity	Na_{Fe}	15.73

Table D.2: *Isolated defect energies of intrinsic defects in $Na_4M_3(PO_4)_2P_2O_7$ with [M=Fe,Mn,Ni,Co] in eV.*

Defect Type	**Transition Metal**			
	Fe	**Mn**	**Ni**	**Co**
Na Vacancy	6.33	6.49	6.69	6.33
M Vacancy	23.39	23.02	25.30	25.22
P Vacancy	145.31	146.00	146.00	146.31
O Vacancy	24.22	24.23	24.81	24.31
Na Interstitial	-4.48	-4.52	-4.41	-4.47
M Interstitial	-18.25	-18.22	-19.03	-18.86
P Interstitial	-121.20	-121.74	-121.65	-120.88
O Interstitial	-18.96	-18.88	-18.90	-16.72
M_{Na} Impurity	-14.62	-14.03	-15.40	-15.23
Na_{Fe} Impurity	15.81	15.40	17.12	16.67

E Surface Energy and Morphology Data

Table E.1: *Surface and attachment energies for all terminations studied in* Na_2FePO_4F.

Plane	d-spacing, d_{hkl}/Å	Type	Termination	Surface energy/J m^{-2}		Attachment energy/Jm^{-2}
				Unrelaxed	Relaxed	
(010)	6.92	II	0.00	16.51	9.55	-4.07
			0.25	1.74	1.44	-0.42
(02$\bar{1}$)	5.96	II	0.00	2.37	1.87	-0.28
			0.16	4.03	2.95	-0.49
			0.50	5.45	3.82	-0.69
			0.84	4.03	2.87	-0.49
(1$\bar{3}$0)	3.47	II	0.00	5.91	3.85	-0.65
			0.23	3.56	2.57	-0.46
			0.50	4.11	2.92	-0.46
			0.77	3.56	2.64	-0.45
(1$\bar{1}$0)	4.89	II	0.00	4.11	2.81	-0.47
			0.23	6.55	4.24	-0.72
			0.50	5.73	3.77	-0.68
			076	6.55	4.09	-0.71
(1$\bar{2}\bar{2}$)	3.40	II	0.00	4.07	2.83	-0.50
			0.20	5.60	3.57	-0.67
			0.50	4.45	3.02	-0.52
			0.80	5.60	3.78	-0.60
(1$\bar{2}\bar{1}$)	3.93	II	0.00	4.68	3.21	-0.54
			0.07	4.15	2.93	-0.52
			0.50	4.15	2.93	-0.52
			0.93	4.15	2.94	-0.49
(001)	5.87	II	0.00	4.35	2.97	-1.12

$(1\bar{1}\bar{2})$	3.76	II	0.00	5.81	3.78	-0.69
			0.10	6.01	3.90	-0.69
			0.14	6.96	4.46	-0.70
			0.25	6.76	4.43	-0.51
			0.36	7.58	4.85	-0.70
			0.42	6.36	4.18	-0.69
			0.50	4.93	3.36	-0.53
			0.58	6.36	4.03	-0.76
			0.64	7.58	4.83	-0.75
			0.75	6.76	4.44	-0.49
			0.86	6.96	4.41	-0.65
			0.90	6.01	3.93	-0.64
$(02\bar{3})$	3.41	II	0.00	5.01	3.43	-0.33
			0.25	6.46	4.27	-0.43
			0.50	5.01	3.43	-0.33
			0.75	6.46	4.27	-0.43
$(01\bar{1})$	4.48	II	0.00	5.51	3.61	-1.39
			0.25	5.41	3.75	-1.72
			0.33	12.72	7.50	-3.60
			0.40	9.11	5.50	-2.90
$(2\bar{2}\bar{1})$	2.40	II	0.00	5.53	3.70	-0.92
			0.50	5.50	3.63	-0.67
$(1\bar{1}\bar{1})$	4.52	II	0.00	6.05	3.98	-0.66
			0.08	6.12	4.01	-0.72
			0.15	5.66	3.79	-0.64
			0.28	6.43	4.12	-0.71
			0.32	6.16	3.95	-0.71
			0.35	6.16	3.95	-0.71
			0.42	6.99	4.42	-0.72
			0.50	6.39	4.15	-0.74
			0.58	6.99	4.51	-0.71
			0.65	6.16	4.05	-0.70
			0.68	6.16	4.05	-0.70
			0.86	5.66	3.69	-0.66
			0.92	6.12	3.92	-0.74
$(10\bar{2})$	3.91	III	0.00	5.51	3.66	-0.66
$(10\bar{1})$	2.39	II	0.00	6.95	4.44	-2.46
(100)	2.62	II	0.25	15.11	8.94	-5.84
$(2\bar{1}\bar{1})$	2.51	II	0.00	5.41	3.57	-0.77
			0.09	5.55	3.63	-0.73
			0.33	5.70	3.73	-0.90
			0.38	5.51	3.63	-0.81
			0.50	5.67	3.71	-0.81
			0.62	5.51	3.62	-0.76
			0.67	5.70	3.74	-0.89
			0.91	5.55	3.66	-0.75

Table E.2: *Extent of surface relxation region normal to the surface in Na_2FePO_4F.*

Surface	**Relaxation Region** (Å)
$(02\bar{1})$	12.0
$(1\bar{1}0)$	9.8
$(1\bar{2}\bar{2})$	10.3
$(1\bar{3}0)$	8.7
(010)	13.9
(001)	23.4
$(02\bar{3})$	13.7
$(1\bar{1}\bar{2})$	7.6
$(1\bar{2}\bar{1})$	12.0

Table E.3: *Relative contribution to the total surface area of individual surfaces in the equilibrium and growth morphologies respectively in Na_2FePO_4F.*

Miller Index	**Percentage of surface area**
$(02\bar{1})$	31.3
(010)	24.5
$(1\bar{2}\bar{2})$	21.9
$(1\bar{1}0)$	12.7
(001)	5.7
$(1\bar{3}0)$	3.9
$(02\bar{1})$	47.4
$(02\bar{3})$	20.8
$(1\bar{1}0)$	18.5
$(1\bar{1}\bar{2})$	10.7
$(1\bar{3}0)$	2.2
$(1\bar{2}\bar{1})$	0.5

F

Density of State and Thermodynamic Data

The doping considered in **Chapter 5** is analogous to mixing of two phases and as such is vulnerable to phase separation and aggregation. We explored the feasibility of doping by calculating the formation enthalpy of solid solutions and hence performing a convex-hull analysis, displayed in Figure F-2. It is found that for the Mn material the $Na_4Fe_2Mn(PO_4)_2P_2O_7$ phase lies above the convex hull and as such is predicted to phase separate into the $Na_4FeMn_2(PO_4)_2P_2O_7$ and $Na_4Fe_3(PO_4)_2P_2O_7$ compositions under low temperature equilibration conditions. The convex hull for the Ni doped material demonstrates significantly different behaviour to that of the Mn doped material. All compositions of the sodiated phase lie along the convex hull; however the formation enthalpies are low, ($\sim$1-10 meV per formula unit), and as such the doped phases are likely to be unstable at room temperature. In addition, the desodiated phases demonstrate a miscibility gap across the composition range. As such in the bulk we predict that these doped phases are unstable and solid solutions are unlikely to be synthesised, instead separating into the $Na_4Fe_3(PO_4)_2P_2O_7$ and $Na_4Ni_3(PO_4)_2P_2O_7$ phases. However, in real systems most materials are synthesised at high temperatures whilst calculations refer to 0 K conditions. It is possible that with the high temperature formation this would help, but the materials would need to be quenched for the solid solution to remain. Alternatively, whilst these calculations deal with the bulk it is possible that nanosizing the materials may stabilise the solid solution phase against separation. In any case, since the $Na_4Fe_2Ni(PO_4)_2P_2O_7$ material is predicted to display an attractive voltage, this warrants further investigation, although if synthesis proves challenging we have shown that the likely explanation is the fundamental thermodynamic stability of the mixed phases.

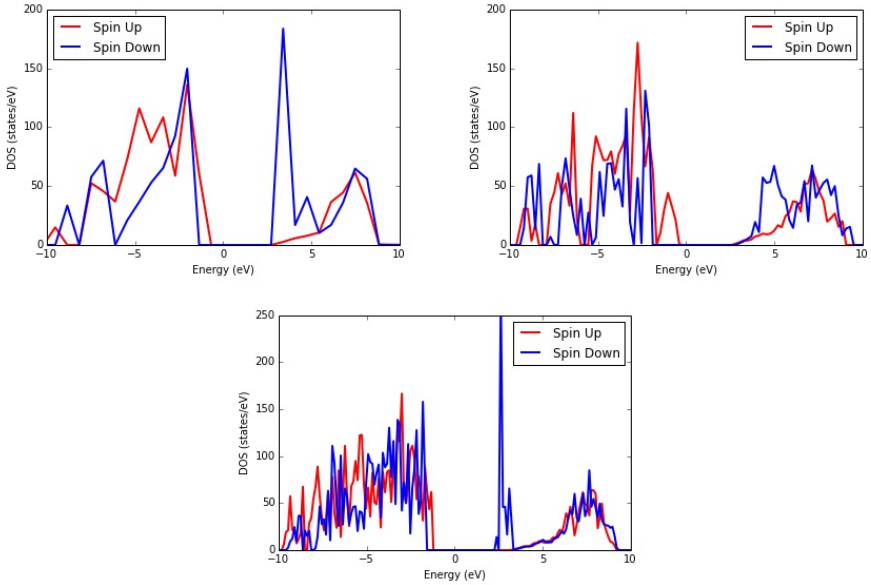

Figure F-1: *Density of states plots for $Na_4M_3(PO_4)_2P_2O_7$ with (a) M=Fe, (b) M=Mn and (c) M=Ni, all demonstrating the expected band gap over the Fermi level (centred at 0 eV).*

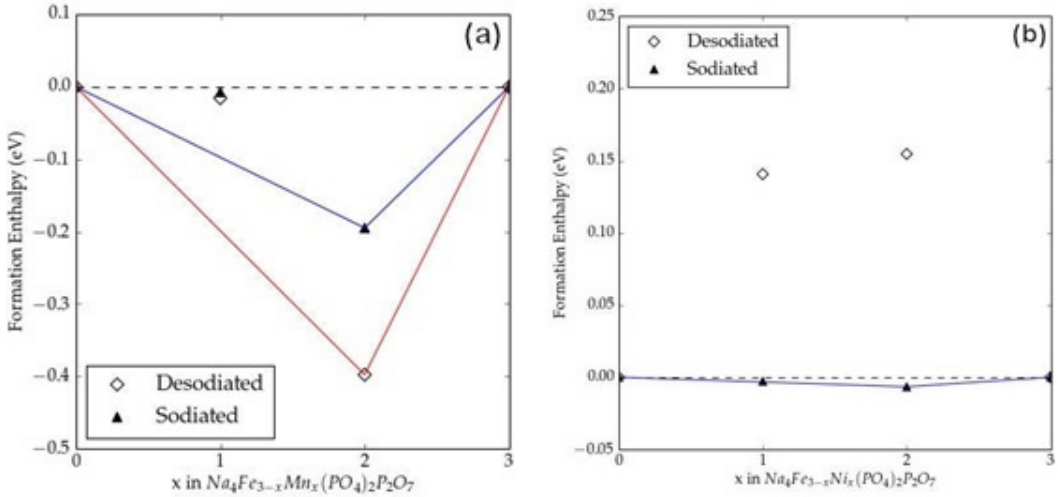

Figure F-2: *The energy of mixing as a function of composition for (a) Mn doping (b) Ni doping in $Na_{4-x}Fe_3(PO_4)_2P_2O_7$ for the sodiated (x=0) and desodiated (x=3) phases in blue and red respectively.*

G Example Datasets

EXAMPLE LAMMPS .in FILE

```
##################################################
#————Variables and cell————————————#
##################################################

clear
units metal #eV,atomic charge,angstroms,ps,kelvin,bars,g/mol
dimension 3
boundary p p p
atom_style full
#processors    grid numa
read_data data.na2cosio4
group sodium type 1
#replicate 2 2 2
variable T1 equal 300
variable Timer equal step*dt

##################################################
#———- Pair styles and electrostatics————#
##################################################

pair_style buck/coul/long 10.0
pair_coeff   0.0 1.0 0.0
pair_coeff 1 4 14825.35672 0.200040 0.00000
pair_coeff 2 4 4639.089976 0.207824 0.00000
pair_coeff 3 4 3794.045952 0.215528372 0.00000
pair_coeff 4 4 22764.2907 0.17747046 0.00000
```

```
kspace_style pppm 1e-05

################################################
# ———— Run Minimization ————————#
################################################

reset_timestep 0
timestep 0.5
thermo 10
thermo_style custom step enthalpy fmax lx ly lz vol press
min_style cg
minimize 1e-25 1e-25 5000 10000

################################################
# ———— Relax Cell ———————————#
################################################

reset_timestep 0
timestep 0.5
fix 1 all box/relax aniso 1.0 vmax 0.003
thermo 1
thermo_style custom step enthalpy fmax lx ly lz vol press
min_style cg
minimize 1e-25 1e-25 5000 10000
unfix 1

################################################
# ————- Run NPT ———————————-#
################################################

reset_timestep 0
timestep 0.002
velocity all create ${T1} 4928459 rot yes dist gaussian
fix 2 all npt temp ${T1} ${T1} 0.01 aniso 1.0 1.0 0.1
thermo_style custom step v_Timer cpu temp etotal fmax lx ly lz vol press
thermo 1000
run 2000
unfix 2

################################################
# ————- Run NVT ———————————-#
################################################
```

reset_timestep 0

restart 5000 rest.1 rest.2

timestep 0.002

compute mymsd sodium msd com yes

variable msdx equal “c_mymsd[1]”

variable msdy equal “c_mymsd[2]”

variable msdz equal “c_mymsd[3]”

variable msdtot equal “c_mymsd[4]”

fix msdT1 sodium ave/time 1 1 10000 v_msdx v_msdy v_msdz v_msdtot file msd${T1}

fix 3 all nvt temp ${T1} ${T1} 0.01

thermo_style custom step v_Timer cpu temp etotal fmax lx ly lz vol press

thermo 5000

#dump dynamics all xyz 10000 dynamics.xyz

run 5000000

unfix 3

unfix msdT1

EXAMPLE LAMMPS .data FILE

LAMMPS Na2CoSiO4 structure file

7488 atoms

4 atom types

0.00000 42.99100 xlo xhi

0.00000 52.47980 ylo yhi

0.00000 42.48880 zlo zhi

Masses

1 22.9898

2 58.9332

3 28.0855

4 15.9994

Atoms

1 1 1 0.600 1.7003 1.0260 0.9751

2 1 1 0.600 4.2712 1.3592 2.7575

3 1 1 0.600 9.0475 4.2220 4.5166

4 1 1 0.600 6.4766 3.8888 6.2990

5 1 1 0.600 3.6736 3.6500 4.5166

6 1 1 0.600 1.1027 3.9832 6.2990

7 1 1 0.600 7.0742 1.5980 0.9751

8 1 1 0.600 9.6450 1.2648 2.7575

9 1 1 0.600 12.4480 22.0179 15.1388

10 1 1 0.600 15.0189 22.3511 16.9212

11 1 1 0.600 19.7952 25.2139 18.6802

12 1 1 0.600 17.2243 24.8807 20.4605

13 1 1 0.600 14.4213 24.6419 18.6802

14 1 1 0.600 11.8505 24.9751 20.4605

15 1 1 0.600 17.8219 22.5899 15.1388

16 1 1 0.600 1.7003 22.0179 15.1388

17 1 1 0.600 4.2712 22.3511 16.9212

18 1 1 0.600 9.0475 25.2139 18.6802

⋮

EXAMPLE GULP .gin FILE

#Keywords

opti conp comp prop phonon defect dist

cutd 3.5

name Na2CoSiO4

#Structural Data

cell

10.906650 5.279282 7.035906 90.000000 90.000000 90.000000

fractional

Co1 core 0.154833 0.206287 0.637000

Si1 core 0.404460 0.204011 0.885768

Na1 core 0.155927 0.215358 0.134794

Na2 core 0.410060 0.251730 0.389158

O1 core 0.324685 0.284045 0.691871

O2 core 0.110121 0.391753 0.417854

O3 core 0.052977 0.231129 0.856077

O4 core 0.146741 0.850796 0.579473

Co1 shel 0.154833 0.206287 0.637000
O1 shel 0.328485 0.275390 0.708321
O2 shel 0.109340 0.415828 0.419935
O3 shel 0.041585 0.236500 0.854006
O4 shel 0.142387 0.844608 0.562657

space
P n a 21

#Defect Information
interstitial frac Co99 0.19 0.26 0.11
centre frac 0.19 0.26 0.11
size 14 28

#Potential Parameters
Species
Co core 0.0
Si core 4.0
Na core 1.0
O core 0.96
Co shel 2.0
O shel -2.96

Buck
Co shel O shel 696.3 0.3362 0.0 0.0 15.0
Na core O shel 1497.830598 0.287483 0.0 0.0 15.0
Si core O shel 1345.432113 0.32052 10.66 0.0 15.0
O shel O shel 22764.3 0.149 43.0 0.0 15.0
Three
Si core O shel O shel 2.09724 109.4 2.0 2.0 5.0

Spring
O 65.00
Co 10.74

EXAMPLE Dl_POLY CONTROL FILE

DL_POLY Control file
temp 325.000000
pressure 0.001
ensemble npt ber 0.1 0.1

timestep 0.0015
steps 750000
equil 0
cap 1000.000000
scale 4000
print 4000
stack 4000
stats 4000

cut 12.000000
delr 1.000000
rvdw 12.000000
integrator leapfrog
ewald precision 0.000010
traj 0 4000 2
rdf 4000
quaternion tolerance 0.000010
shake tolerance 0.000010
msdtmp 0 4000

job time 86400
close time 1000

finish

EXAMPLE DL_POLY FIELD FILE

DL_POLY Field file
UNITS eV

MOLECULES 26

Sodium1

NUMMOLS 960

ATOMS 1

Na1 22.989799 0.6000000 1

FINISH

Sodium2

NUMMOLS 864

ATOMS 1

Na2 22.989799 0.6000000 1

FINISH

Sodium3

NUMMOLS 864

ATOMS 1

Na3 22.989799 0.6000000 1

FINISH

Sodium4

NUMMOLS 960

ATOMS 1

Na4 22.989799 0.600000 1

FINISH

⋮

FINISH

VDW 12

O O mors 0.042395 3.618701 1.379316

P1 O mors 0.831326 1.800790 2.585833

P2 O mors 0.831326 1.800790 2.585833

P3 O mors 0.831326 1.800790 2.585833

P4 O mors 0.831326 1.800790 2.585833

Na1 O mors 0.023363 3.006315 1.763867

Na2 O mors 0.023363 3.006315 1.763867

Na3 O mors 0.023363 3.006315 1.763867

Na4 O mors 0.023363 3.006315 1.763867

Fe1 O mors 0.078171 2.658163 1.822638

Fe2 O mors 0.078171 2.658163 1.822638

Fe3 O mors 0.078171 2.658163 1.822638

CLOSE

EXAMPLE DL_POLY CONFIG FILE

DL_POLY Config file

2 2 24768 500000 1.5000000E-03 7.5000000E+02

73.8628176648 0.0000000000 0.0000000000

0.0000000000 66.7351943104 0.0000000000

0.0000000000 0.0000000000 65.2659203787

Na1 1

19.11089653 1.631870931 4.770628419

3.191196460 -0.5072243157 -0.8786410143

431.9290373 2087.301783 693.0205150

Na1 2

36.63723017 5.206276198 6.165463223

-3.845006684 -0.2315047309 -0.1905282430

-1383.927856 -343.4373883 1583.641780

Na1 3

28.23117433 1.645062141 0.6911487074

1.600940176 1.178663183 -2.329669428

-1080.757524 -243.2350076 -477.3170553

Na1 4

27.13010292 4.969876351 10.28216746

0.3524720803 -0.5224162695 -6.492517599

-2779.580486 3001.508666 -668.1407884

Na1 5

-36.56309958 2.035973097 4.953429372

0.6720420201 1.408980952 -1.170759390

-1489.216286 -253.9752158 443.9360519

Na1 6

-18.33726153 5.530476452 6.189370013

-2.131165016 -0.2221127362 -3.454165743

-2693.949094 2451.380732 -1363.089892

Na1 7

-27.31830700 1.715870110 0.9066635788

⋮

EXAMPLE VASP INCAR FILE

SYSTEM = Na2FePO4F Surface

#Start Parameters:
ISTART=0
ICHARG=2

LREAL=AUTO

NELMIN = 4 #min of 4 electronic steps
EDIFF = 1E-6 #electronic accuracy
EDIFFG = -0.01 #accuracy of ions
NSW = 100 #max of 100 ionic steps in ions
IBRION = 2 #use BFGS algorithm
NELM = 40 #Max number of electronic steps
NCORE = 16
ISMEAR = 0
SIGMA = 0.2
LORBIT = 11

ADDGRID = TRUE
ISIF = 2
ISPIN = 2
ALGO = A
MAGMOM = 192*0.0 48*0.0 96*0.0 48*0.0 48*4.0

#GGA + U parameters
LDAU = .TRUE.
LDAUTYPE = 2
LDAUL = -2 -2 -2 -2 2
LDAUU = 0.0 0.0 0.0 0.0 5.0
LDAUJ = 0.0 0.0 0.0 0.0 1.0
LASPH = .TRUE.

#CONVERGENCE SETTINGS
GGA = PE
ENCUT = 500.0 eV
PREC = Accurate

EXAMPLE VASP KPOINTS FILE

Automatic Mesh

0

Gamma

3 3 3

0. 0. 0.

EXAMPLE VASP POSCAR FILE

O F Na P Fe

1.00000000000000

13.0652799376736173 0.0000000000000000 0.0000000000000000
-4.2542079959640056 17.0240988223515330 0.0000000000000000
0.0000000000000000 0.0000000000000000 44.6919438625337548

O F Na P Fe
192 48 96 48 48

Direct
0.1709210422148836 0.6131561344296012 0.0700627016870814
0.2001907922872808 0.0279826553407702 0.0675280862524989
0.6720331947257541 0.3790077424386919 0.0660999874276427
0.6832488707139913 0.7514093086344620 0.0533757560473487
0.7162336407673950 0.2506177866551789 0.0506943685894749
0.4888825944591780 0.0867687371408674 0.0512578447207648
0.2288824511365092 0.4949944350809403 0.0497494903511897
0.0015531998688482 0.8569271714805909 0.0465917645316398
0.4550658373073217 0.4909553826846453 0.0392849068676416
0.9924629842731724 0.2214988267821675 0.0329993125936556
⋮

EXAMPLE VASP POTCAR FILE

PAW_PBE O 08Apr2002

6.00000000000000000

parameters from PSCTR are:

VRHFIN =O: s2p4

LEXCH = PE

EATOM = 432.3788 eV, 31.7789 Ry

TITEL = PAW_PBE O 08Apr2002 LULTRA = F use ultrasoft PP ?

IUNSCR = 0 unscreen: 0-lin 1-nonlin 2-no

RPACOR = .000 partial core radius

POMASS = 16.000; ZVAL = 6.000 mass and valenz

RCORE = 1.520 outmost cutoff radius

RWIGS = 1.550; RWIGS = .820 wigner-seitz radius (au A)

ENMAX = 400.000; ENMIN = 300.000 eV

ICORE = 2 local potential

LCOR = T correct aug charges

LPAW = T paw PP

EAUG = 605.392

DEXC = .000

RMAX = 2.264 core radius for proj-oper

RAUG = 1.300 factor for augmentation sphere

RDEP = 1.550 radius for radial grids

QCUT = -5.520; QGAM = 11.041 optimization parameters

Description

l E TYP RCUT TYP RCUT

0 .000 23 1.200

0 -.700 23 1.200

1 .000 23 1.520

1 .600 23 1.520

2 .000 7 1.500

Error from kinetic energy argument (eV)

NDATA = 100

STEP = 20.000 1.050

163. 160. 159. 156. 154. 151. 148. 146.

142. 139. 137. 134. 130. 126. 123. 119.

115. 111. 108. 102. 98.8 95.2 90.0 86.6

83.2 78.3 73.5 70.4 65.9 61.6 57.4 53.4

49.6 46.0 42.6 39.3 35.3 32.4 28.9 26.4

23.4 20.6 18.1 15.8 13.7 11.9 10.3 8.47

7.22 5.87 4.73 3.95 3.13 2.45 1.80 1.37

1.03 .721 .493 .329 .215 .138 .882E-01 .534E-01

.367E-01 .267E-01 .223E-01 .205E-01 .193E-01 .181E-01 .162E-01 .138E-01

.112E-01 .878E-02 .646E-02 .490E-02 .370E-02 .300E-02 .259E-02 .238E-02

.219E-02 .196E-02 .167E-02 .132E-02 .100E-02 .764E-03 .617E-03 .544E-03

.522E-03 .507E-03 .467E-03 .403E-03 .312E-03 .236E-03 .181E-03 .157E-03

.152E-03 .150E-03 .139E-03 .118E-03

END of PSCTR-controll parameters

local part

122.832189257630020

.23155445E+02 .23152693E+02 .23149261E+02 .23143544E+02 .23135541E+02

.23125253E+02 .23112681E+02 .23097823E+02 .23080677E+02 .23061237E+02

.23039495E+02 .23015440E+02 .22989059E+02 .22960335E+02 .22929249E+02

.22895777E+02 .22859896E+02 .22821578E+02 .22780793E+02 .22737509E+02

.22691690E+02 .22643299E+02 .22592293E+02 .22538630E+02 .22482260E+02

.22423132E+02 .22361190E+02 .22296376E+02 .22228625E+02 .22157873E+02

⋮

H Published Papers

Publications

1. Tripathi R., Wood S. M., Islam M. S. and Nazar L. F. "Na-ion mobility in layered Na_2FePO_4F and olivine $Na[Fe,Mn]PO_4$", *Energy Environ. Sci.* **6**, 2257-2264 (2013).

2. Wood S. M., Eames C., Kendrick E. and Islam M. S. "Sodium Ion Diffusion and Voltage Trends in Phosphates $Na_4M_3(PO_4)_2P_2O_7$ (M = Fe, Mn, Co, Ni) for Possible High-Rate Cathodes", *J. Phys. Chem. C*, **119 (28)**, 15935-15941 (2015)

3. Roos J., Eames C., Wood S. M., Whiteside A. and Islam M. S., "Unusual Mn coordination and redox chemistry in the high capacity borate cathode $Li_7Mn(BO_3)_3$", *Phys. Chem. Chem. Phys.*, **17**, 22259-22265 (2015)